UNIVERSITY OF OKLAHOMA

GRADUATE COLLEGE

STUDY OF CARBON PARTICULATES IN COFLOW DIFFUSION VAPORIZED BIODIESEL, DIESEL, AND BLENDED BIODIESEL/DIESEL AIR-FLAMES

A DISSERTATION

SUBMITTED TO THE GRADUATE FACULTY

in partial fulfillment of the requirements for the

Degree of

DOCTOR OF PHILOSOPHY

By

ALIREZA ABDIHAMZEHKOLAEI
Norman, Oklahoma
2019

STUDY OF CARBON PARTICULATES IN COFLOW DIFFUSION VAPORIZED BIODIESEL, DIESEL, AND BLENDED BIODIESEL/DIESEL AIR-FLAMES

A DISSERTATION APPROVED FOR THE
SCHOOL OF AEROSPACE AND MECHANICAL ENGINEERING

BY

Dr. Wilson Merchan-Merchan, Chair

Dr. Steven Crossley

Dr. Jivtesh Garg

Dr. Yingtao Liu

I dedicate my dissertation to my family,

Especially to my wonderful father and my beloved wife.

Acknowledgements

First, I would like to thank my academic advisor, Dr. Wilson Merchan-Merchan, for his guidance and support.

I also would like to thank my committee members, Dr. Crossley, Dr. Garg, and Dr. Liu for their valuable feedback and support.

Many thanks to AME faculties and staff for their time, guidance, and consideration during my PhD program at OU.

The support of this work by the National Science Foundation through the grants CBET-1067395 and REU CBET-1440030 is gratefully acknowledged.

I am thankful to the Gallogly College of Engineering for the "Dissertation Excellence Award" which helped me to complete my dissertation.

Additionally, I am grateful to Farzaneh Family and Dolese company for their support and generous scholarships.

I would like to thank Dr. Russell and Dr. Larson from the Samuel Roberts Noble Electron Microscopy Laboratory for their day-to-day help in electron microscopy, comments, and helpful suggestions.

I am thankful to Steven McCollam and Juan Felipe Correa Pugliese for the initial setup of the burner, and also undergraduate students in our lab (Duncan Merchan-Breuer, Courtney Baukal, Mike Treinen, and Stephanie Prado) for their assistance.

Special thanks to my family who despite being far from me, always was supportive and caring.

Many thanks to my friends who were always there for me and became my family.

Finally, I am deeply grateful of my fantastic wife who was there every step of the way and never stopped supporting, loving, caring, and believing in me.

Table of Contents

List of Tables

List of Figures

Abstract

Biodiesel, which is a biodegradable and renewable fuel, has been considered one of the best alternative fuels for diesel due to its chemical similarity. Compared to diesel, burning biodiesel will reduce various emissions such as particulate matter, unburned hydrocarbons, carbon monoxide, and carbon dioxide which are well-known harmful components for the environment and human health. Employment of biodiesel/diesel blends is very common as well, especially in compression-ignition (CI) engines, as allows to lessen the difficulties of using pure biodiesel and help reducing the final fuel price. Therefore, studying the impact of biodiesel on combustion emissions is of great interest and was the main motivation for the current study. Despite the established findings on biodiesel, still there is not a clear understanding of how particulate matter forms and oxidizes during the combustion of this renewable fuel. In this experimental study, a detailed evolution process of carbon particulate formation along the axial direction of various co-flow diffusion air flames is presented. The studied flames are formed by three popular biodiesels (canola methyl ester (CME), cotton methyl ester (COME), and soy methyl ester (SME)), #2 diesel, and diesel/CME blending. Soot samples were collected directly from inside of the flame volume using the thermophoretic sampling technique which employs the temperature gradient to capture particles from specific flame positions. Transmission electron microscopy (TEM) follows the sample extraction to analyze and obtain the desired properties. The obtained evolution process provides information of particle size, liquid-like and droplet-like characteristics, fractal dimension, radius of gyration, number of primary particles per aggregates, and nanostructure of soot samples extracted from studied flames. A typical soot formation and oxidation behavior

was detected inside all tested flames. However, unique structures resembling tar-like material with droplet-like characteristic were dominant inside the evaporated biodiesel and blended fuel flames. Physical properties of soot aggregates (such as fractal dimension (D_f), degree of branching, aggregates skeleton and branching length) were calculated from their two-dimension projections (TEM images). Fractal analysis of TEM images aids in quantifying morphologic variations of fractal aggregates and correlating them to growth and evolution mechanism. Outside the soot inception region, distinct fractal-like morphologies were detected between biodiesel and diesel. The calculation resulted in lower D_f values for aggregates generated by the tested biodiesels and blended mixtures compared to diesel indicating more open-structured soot aggregates for biodiesel and blending and more compact aggregates for diesel. However, since D_f values cannot solely explain the considerable difference observed between soot clusters produced by various tested fuels, the branching and skeleton length have been employed to quantify distinguishable characteristics of soot aggregates. It was noticed that all tested biodiesels and blended mixtures formed flames containing soot aggregates with stronger branching and longer skeleton length compared to diesel (except B20, which the number after the letter "B" represents the percentage of biodiesel in the fuel mixture). The evolution of soot aggregates is hypothesized to cause the distinct characteristics. The agglomeration and growth stages inside the biodiesels, B50, and B80 flames are observed to follow the order of soot inception, monomer-cluster aggregation, carbonization, and cluster-cluster aggregation. However, the growth process inside the diesel and B20 flames is spotted to be slightly different with carbonization proceeding the monomer-cluster aggregation. In addition to the growth process, biodiesel was found to strengthen the soot inception hence

increasing the concentration of singlet particles which can enhance the branching and elongation of the agglomerates. High-resolution TEM (HR-TEM) images of selected soot particles revealed a nanostructure composed of shorter and more curved carbon layers with smaller interlayer separation in case of biodiesel and blending with respect to diesel. This observation suggests less graphitized internal structure and higher oxidative reactivity for biodiesel which is another desired characteristic in particulate filters.

Much of the material in chapters 4 and 6 of this dissertation is verbatim from a recently published journal paper. Co-authors have granted full authority for the reproduction of the material.

- Merchan-Merchan, Wilson, Alireza Abdihamzehkolaei, and Duncan A. Merchan-Breuer. **"Formation and evolution of carbon particles in coflow diffusion air flames of vaporized biodiesel, diesel and biodiesel-diesel blends."** Fuel 226 (2018): 263-277.

1 Introduction

1.1 Petroleum-based fuels and alternatives

Diesel engines are favorable in a wide variety of applications such as transportation, construction, and agricultural especially in heavy duty applications due to their higher torque, thermal efficiency, drivability, and lower fuel consumption than gasoline engines [1, 2]. More than 40% of global on-road energy consumption is dominated by diesel which is also the main fuel of 90% of heavy-duty trucks and 75% of buses [3]. However, diesel engines are associated with the high emission of oxides of nitrogen (NOx) and particular matter (PM) which are major health and environmental concerns [4]. The simultaneous decrease of NOx and PM is challenging in conventional diesel engines [5].

The statistics of 2014 report that while the number of diesel vehicles accounted for only 14.1% of the total vehicle volume, their contribution rate of NOx and PM is 69.2% and 99%, respectively [6]. diesel exhaust is in category 1 carcinogen for humans, as stated by the International Agency for Research on Cancer [7]. Many studies have proved that PM emission leads to degenerative disorders and diseases [8-10]. In 2016 alone, outdoor air pollution was anticipated to cause 4.2 million deaths worldwide [11]. Therefore, controlling the exhaust emissions of diesel engines is of great interest and has become one of the top research subjects in atmospheric protection [12].

Currently, there are different technologies for emissions reduction of diesel engines through the optimization of the engine structure and parameters (geometry, ignition delay, etc.) [13] or after-treatment devices (e.g. NOx and particulate traps) [14]. These technologies need a large investment and time, thus cannot become a short-term

solution. Moreover, after-treatment devices have a negative impact on the engine fuel conversion efficiency [15]. Particulate traps, which are commonly employed in heavy-duty diesel vehicles to reduce the PM emission, increase the engine fuel consumption because of the required energy for regenerating the trapped PM and also the back pressure generated in the exhaust manifold [16, 17].

The usage of alternative fuels and their mixtures with diesel is becoming another way to reduce the harmful emissions of diesel engines. Besides, using alternative fuels can decrease the demand for fossil fuels which are dwindling. Among available fuels, alcohols, natural gas, dimethyl ether (DME) and biodiesel are the four most promising and attractive alternatives, because they can be easily obtained, handled and stored [18]. Biodiesel is the best diesel fuel alternative in CI engines due to its desirable properties including high cetane number, low aromatic content, low PM emission, biodegradability, and molecular oxygen content [19, 20].

1.2 Biodiesel

1.2.1 Introduction to biodiesel

Oils extracted from vegetables, animal fats and their derivatives can be transformed into a fuel called biodiesel through a simple chemical reaction process (transesterification) as shown in Figure 1. In that process, a short-chain alcohol (typically ethanol or methanol) is added to a triglyceride molecule (oil) in order to separate the fatty acid chains that are attached to a glycerol “backbone”. Potassium hydroxide or sodium hydroxides are typically used to act as a catalyst to speed up the reaction [21]. One of the derived components from the transesterification process is considered a fuel that is clean,

biodegradable, non-toxic, renewable and potentially the best replacement for petroleum-based fuel [21]. In recent years, research in the area of biodiesel has been focused on the synthesis processes, type of catalyst, and performance of these alternative fuels [22-24].

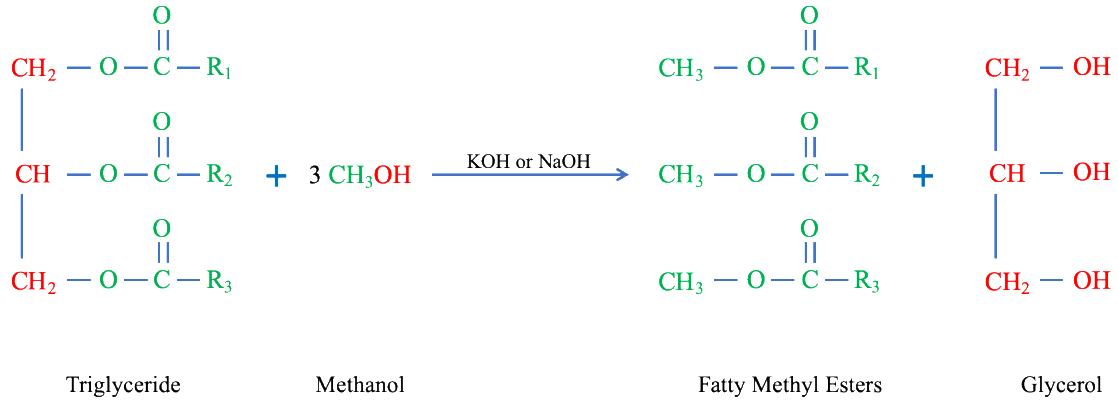

Figure 1. Schematic of the transesterification process in which vegetable oil or animal fat can be transformed into biofuel by reacting with an alcohol.

The use of vegetable oils as alternative fuels in diesel engines is almost as old as the diesel engine itself. The concept of vegetable oils as an alternative renewable fuel was proposed in the early 1980s [25]. The German inventor of diesel engines Rudolph Diesel designed the original diesel engine to run on vegetable oil and used peanut oil as the fuel at the Paris Exposition of 1900 [26]. A variety of vegetable oils including hemp and peanut oil were suitable for the engine due to the high temperatures created. vegetable oils were used as diesel fuels occasionally and in emergency situations in the 1930s and 1940s [27]. Vegetable oils were not widely acceptable as fuels due to their higher price than petroleum fuels. However, with the price increase of petroleum and uncertainties about its availability, vegetable oils became more attractive since they come from renewable resources and bring environmental benefits [28]. The first International Conference on Plant and Vegetable Oils as Fuels was held in North Dakota in August 1982. Cost of the fuel, the effects of vegetable oil fuels on engine performance and

durability, fuel preparation, oilseed processing and extraction were the main concerns discussed in that meeting [29, 30]. Biodiesel (mono alkyl esters) started to be extensively produced in the 1990s followed by a steady production increase ever since [31].

There are many advantages associated with biodiesel such as being renewable and available locally, biodegradable, non-toxic, easy to store, and transfer, having molecular oxygen content (~11%), high cetane number, high miscibility with diesel, superior lubricity, and reducing CO_2, CO, and SO_x emissions [28, 32]. However, there are some disadvantages and limitation with the usage of biodiesel including increasing NOx emission in some cases, lower energy content, poor storage stability, high viscosity, cloud point, and price [19, 33-35]. For instance, due to its high cloud point, it can be difficult to use biodiesel in a very cold region since it tends to crystalize.

In addition to the limitations of biodiesel under extreme environmental conditions, there has been a social issue on “food vs. fuel” controversy. Despite the advantages of biodiesel, there have been some concerns about the consumption of large volume of grains and other edible feedstocks to produce biofuels [36]. Moreover, enormous areas of farm lands are needed for making enough biofuels to compete with petrofuels. These factors are promoting the production of biodiesel from less controversial feedstocks. Some of the non-edible plants suitable for biodiesel are cottonseed, jatropha, microalgae, neem, karanja, rubber seed, mahua, silk cotton tree, etc [37-40]. For instance, algae are composed of a broad genetic diversity that is considered photosynthetic and aquatic [41, 42]. Some of algae groups can grow rapidly to order of meters long which can increase the biodiesel production pace. Some of them can grow double in only six hours and many

exhibited two doublings per day [43]. Most algae groups are able to produce energy-rich oils [39].

More than 350 oil-bearing crops have been identified but only soybean, rapeseed, cottonseed, palm, sunflower, safflower, and peanut oils are considered potential alternative fuels for diesel engines [44]. Canola methyl ester (CME), Soybean methyl ester (SME), and cottonseed methyl ester (COME) are among the most favorable biodiesels in terms of having the best properties for an alternative diesel fuel [45]. Furthermore, CME and SME are the most common feedstock biodiesel in Europe and USA, respectively [46]. COME, however, is of great interest since it comes from a non-edible feedstock and does not conflict with the edible feedstock market.

1.2.2 Properties of biodiesel and their comparison to diesel

Chemically speaking, diesel fuel is composed of mainly saturated non-branched hydrocarbons with 12 to 24 carbon atoms while biodiesel includes esters (methyl or ethyl) with varying chemical structures. The main fatty acid methyl ester (FAME) composition of biodiesel is methyl laurate, behenate, lignocerate, palmitate, stearate, oleate, linoleate, and linolenate [32].

Viscosity is one of the most important properties of biodiesel due to its influence on the fuel injectors. Low viscosity is desirable since high viscosity results in poor fuel spray atomization preventing the accurate operation of fuel injectors [28]. The main purpose of the transesterification process is to reduce the viscosity of vegetable oils to become more suitable for diesel engines. Transesterification can reduce the viscosity by a factor of eight [28]. The viscosity of vegetable oils are between 27.2 and 53.6 mm^2/s while vegetable oil methyl esters have viscosity values between 3.6 and 4.6 mm^2/s.

compared to #2 diesel with a viscosity of 2.7 mm^2/s at 311 K, all vegetable oil methyl esters are slightly viscous [47].

The density of biodiesels are slightly higher (2-7%) than that of #2 diesel which is 860 kg/m^3 [48]. The flash point temperature of diesel is around 336 K which is lower than biodiesel [49].Having a higher flash point temperature make biodiesel less volatile and safer for storage and transport. Viscosity, density, and flash point of several biodiesels are presented by Table 1. Various physical properties of several popular biodiesels. below.

Table 1. Various physical properties of several popular biodiesels.

Methyl ester	Cetane number	kinematic Viscosity mm^2/s (at 313 k)	Density kg/m3 (at 288 k)	Flash point k	Cloud point k	Ref.
Cottonseed Oil	54.13	4.07	870	423	280	[50]
Soybean Oil	60.1	3.97	885	412	269	[51, 52]
Canola Oil	61.5	4.34	883	380	274	[51, 53]
Hazelnut Kernel Oil	53.35	3.59	860	422	262	[28, 54]
Linseed Oil	55	3.82	890	447	269	[28, 55, 56]
Mustard Oil	61.1	4.10	885	441	277	[28, 57]
Palm Oil	57.3	3.94	880	431	283	[28, 55, 58]
Safflower Oil	56	4.03	880	440	268	[28, 55, 59]
Sunflower Oil	51.25	4.16	880	439	259	[28, 54]
Diesel #2	47	2.7	860	336	255	[47-49]

The cetane number is another important property in diesel engine implying the ignition quality of the fuel. Higher cetane number means shorter ignition delay which is favorable in diesel engines [46]. Biodiesel generally has a higher cetane number compared to diesel, and the cetane number of biodiesel coming from animal fats are higher than that from vegetable oils [60]. The cetane number of several biodiesels have been reported to be from 52 to 64 compared to 47 for diesel [61]. Cloud point and pour point are two important properties especially in low-temperature applications of the fuel. Biodiesel has higher cloud and pour points compared to diesel which means biodiesel cannot flow in very cold environments [62]. For instance, the cloud point of #2 diesel is -18 ºC while for several common biodiesels is in the range of -3 to 23 ºC which is considerably higher [61].

Another important property of a fuel is the energy content which is the amount of heat released during a complete combustion of one gram of fuel leading to production of CO_2 and H_2O. The standard indication of the energy content is known as higher heating value (HHV), also referred to as the calorific value or heat of combustion. The HHV of biodiesel (39 to 41 MJ/kg) is slightly lower than that of diesel (43 MJ/kg) [28].

1.2.3 Biodiesel's influence on combustion

Various combustion configurations (e.g. diesel engines and shock tubes) have been employed to study the emissions from the burning of biodiesel [63-66]. Several studies have shown that biodiesel can significantly reduce engine emissions such as CO_2, CO, SOx, and other volatile organic compounds [67, 68]. However, using biodiesel can increase the NOx emission in most cases [69-71] while there are some studies reporting the NOx increases only in certain operation conditions [72-74] and others even reported

a decrease in NOx with biodiesel compared to diesel [75-77]. Studies in diesel engines have revealed that the presence of oxygen in the biodiesel can improve the combustion quality and therefore reduce PM emissions [63-66].

Biodiesel's physical and chemical properties can affect the performance of compression ignition (CI) engines. While it is generally accepted that biodiesel enhances the start of combustion due to its higher cetane number than diesel [78, 79], various biodiesels (from waste cooking oil, palm, and rapeseed) have shown to increase the ignition delay compared to conventional diesel due to their higher viscosity [80, 81]. The high viscosity of biodiesel can also slow down the needle speed and reduce the performance of the flow in the injector during the transient injection behavior [82]. Biodiesel has shown to decrease the injector spray angle resulting in poor air entrainment and higher Sauter mean diameter [81, 83]. Moreover, biodiesel can reduce the equivalence ratio along the axis of the fuel spay compared to diesel due to the presence of inherent oxygen in the molecular structure [78].

In diesel engines, a loss in torque and power is expected when using biodiesel instead of diesel mostly due to the lower heating value of biodiesel. For example, sunflower-oil biodiesel and diesel fuels were compared by Kaplan et al. [84] and a torque and power loss of 5% to 10% was reported. However, there have been some studies reporting higher torque for biodiesel than diesel [65, 85, 86]. Brake-specific fuel consumption is another important parameter which can be increased by around 14% when biodiesel is used instead of diesel [65, 87, 88]. The lower heating value and oxygen content of biodiesel cause the higher fuel consumption. The thermal efficiency of diesel

engines have been reported not to vary significantly with the use of biodiesel compared to diesel [89-91].

1.3 Blending

1.3.1 The importance of blending

Due to due the negative environmental effects and the limited resources of diesel, biodiesel, a renewable form of energy, has the potential to become the alternative source of energy and replace petroleum derived fuel. However, the usage of pure biodiesel has its own complications. Some well-known major drawbacks of biodiesel are i) Its high viscosity comparted to Diesel or other liquid fuels; ii) its strong effect towards oxidation and thermal degradation; and iii) its high cloud point that will lead to solidification of the fuel at higher temperatures in comparison to diesel. For instance, the cloud point for CME is -3 ºC compared to #2 Diesel with a value of -18 ºC [92], and the viscosity of CME is 3.3 mm^2/s compared to #2 Diesel that has a value of 2.7 mm^2/s at the temperature of 311 K [93]. The high viscosity could lead to several issues such as poor fuel atomization during spraying, more engine deposits, higher required energy to pump the fuel, and wear on injectors and pump components [51]. Sensitivity to oxidative and thermal degradation are also major concerns regarding the usage of biodiesel which may enhance the corrosion and deposits in tanks, fuel systems and filters [94, 95]. Oxidation instability and deterioration of the lubricant properties are other important barriers to use pure biodiesel in a large scale [94, 96, 97]. Due to the high demand/consumption of Diesel in internal combustion engines in the transportation sector biodiesel can be a gamechanger. In the USA, the transportation area alone consumes about 557 million gallons of petroleum per

day in January 2019 [98] which implies the need for a plausible renewable replacement for petroleum-based fuels.

One of the simplest and cheapest ways to remedy some of these problems is to blend biodiesel with Diesel. For instance, the blending of biodiesel (characteristics of higher cloud point) with a Diesel (lower cloud point) can significantly improve the practicability of biodiesel in low temperature environments. Fortunately, biodiesel is thoroughly miscible with diesel making it possible to use their blending in order to take advantage of biodiesel's benefits and at the same time lessen the aforementioned problems; also, the overall price would be lower comparing to pure biodiesel since biodiesel has a price more than double than petro diesel mostly because of the high price of feedstock [35, 99]. Therefore, many studies have been conducted with the aim of investigating the properties and emissions of various biodiesel/diesel blends [64, 92, 99-104].

1.3.2 Physical properties of blended fuels

Besides emissions, physical properties of blended fuels are another key factor needed to be considered because of their important role in engine performance. For this reason, Kinast [100] studied the fuel properties of various biodiesel/diesel blends with different concentrations and found that in the case of all biodiesels, the viscosity increased by increasing the biodiesel concentration from 3% to 100%. The same trend was observed for other properties including the pour point, cloud point, and cetane number. Another study reported analogous observations: an increase of viscosity, density, cloud point, cetane number, and a decrease of low heating value with increasing the biodiesel (palm oil) concentration [99]. Similar trends were reported for soybean biodiesel/diesel blends

elsewhere [101]. B20 has been reported to be the optimum, very popular, and an easy storage blend; it also does not require any engine modification when being used in a diesel engine [104, 105].

1.3.3 Effects of blending on combustion

There have been numerous studies focusing on the impact of blending on engine performance and emissions. For instance, it has been reported that the blended fuels decrease the power of the engine, and the higher biodiesel percentage in the blend leads to lower engine power due to the lower heating value of the biodiesel than diesel [84, 106]. Likewise, brake-specific fuel consumption (BSFC) of the diesel engine has been observed to increase with blends with higher biodiesel concentration [65, 106-108]. Regarding the emissions, Qi., et al. [101] investigated the effects of 10% (B10), 20% (B20), 30% (B30), and 40% (B40) soybean biodiesel/diesel blends on a diesel engine and found that the blends reduce the emission of particulate matter (PM), HC, and CO while increasing the NOx emission. Similar trends were also reported by other researchers [102, 103]. It is established that the decrease in PM emission could be related to the less aromatic content which is responsible for the formation of PAHs and consequently PM. Another suggested reason could be the biodiesel's oxygen component providing oxygen to the fuel rich zone, where soot formation happens, and subsequently reduces PM emission. Reduction of CO and HC could be attributed to the oxygen content and higher cetane number of the biodiesel which, on the other hand, are responsible for increasing the NOx emission [103]. However, retarding the fuel injection timing has been proven to be an effective way in order to decrease the NOx emission [103, 104]. More specifically, many studies have focused on the PM or soot characteristics emitted from diesel engines

running by biodiesel/diesel blends. It has been shown by Andrea et al. [92] that soot formed in a diesel engine running with biodiesel/diesel blends can be significantly different from that of diesel. The same group reported that the higher content of biodiesel in the blend leads to soot particles with shorter carbon layers and more open structure with the higher surface area which may enhance the oxidation process. Soot nanostructure of shorter graphene segments along with more amorphous and disordered structure, which enhances the oxidation, was also observed in the case of biodiesel/diesel blend compared to the diesel fuel in a diesel engine [64].

1.4 Soot formation

1.4.1 Soot evolution mechanism

Combustion of hydrocarbons results in carbon dioxide and water as the products under ideal condition, which could be defined as having sufficient oxygen for all hydrocarbon molecules in the entire combustion process. However, in reality, combustion configurations such as engines, furnaces, and gas turbines are usually far from ideal combustion conditions. As a result, insufficient oxygen leads to other byproducts such as carbon monoxide, unburned hydrocarbons, hydrogen, and soot in addition to carbon dioxide and water [109]. The term soot generally refers to the particulates formed in the fuel rich condition of combustion, with the carbon to hydrogen ratio about 8 in the case of the mature soot, and smaller (~1) in the case of newly formed or young soot [110].

It is well known that the mechanism of soot formation is composed of several processes: fuel pyrolysis, nucleation, coalescence, surface growth, agglomeration, and oxidation [110]. The first 5 processes are related to soot formation while the last one (oxidation) has the tendency to turn hydrocarbons to CO_2, CO, and water [110]. Figure 2

illustrates a schematic of a coflow diffusion flame with different labeled flame zone which are associated with various soot evolution processes. These processes will be briefly described in the following paragraph.

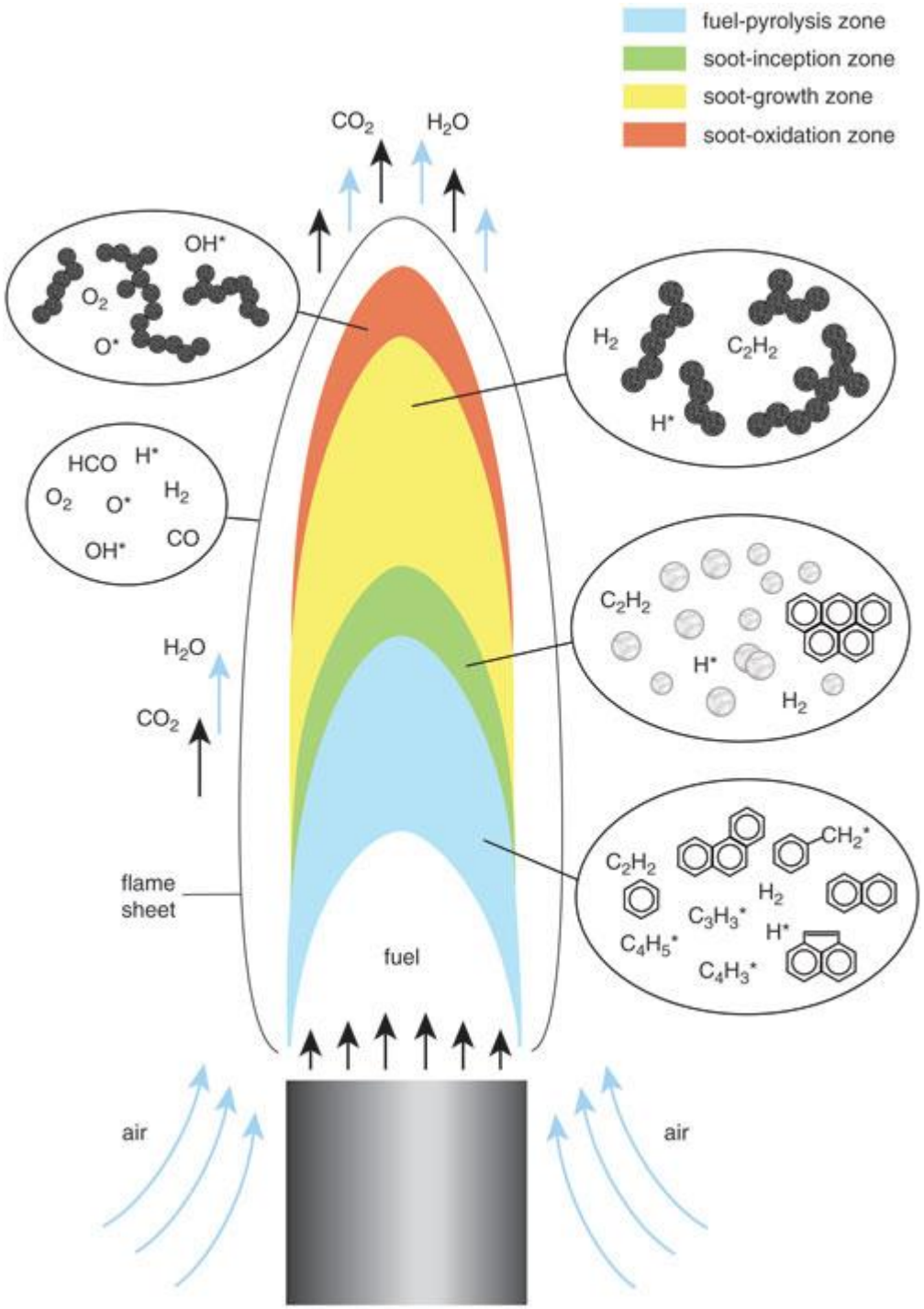

Figure 2. Schematic of a coflow diffusion flame labeled with different flame zone attributed to soot evolution stages. (from [111])

The first step in the soot formation mechanism (fuel pyrolysis) is a process in which the fuel molecular structure is altered due to the high temperature in the absence of oxygen [112]. Species resulting from fuel pyrolysis are essential for soot formation. Both fuel pyrolysis and oxidation rates increase with the temperature increase; however, as temperature increases, the rate of oxidation surges faster than that of pyrolysis. In general, fuel pyrolysis of hydrocarbons would result in unsaturated hydrocarbons (especially acetylene), polycyclic aromatic hydrocarbons (PAHs), and polyacetylenes [110]. The next step is nucleation which is probably the least known part of the soot formation mechanism. It refers to the formation of solid particles from gas-phase material [113]. It has been suggested that the addition of small radical hydrocarbons to large aromatics may cause nucleation or soot inception. The formation of first and second aromatic ring (mostly benzene) structures would be considered as the initial step in nucleation, which provides sites for gas-phase alkyls, acetylene, and other components to attach in order to form and grow PAHs [110]. When PAHs become sufficiently large, they form very small particles generally called nuclei. After forming the nuclei, gas-phase hydrocarbons (mostly acetylene) attach to the hot surface which leads to the growth of mass and size (surface growth). Soot particles continue to grow even when they are outside the main reaction zone and reach cooler and less dense regions [114]. Since in this process, mass is added to the existing particles, surface growth does not affect the number of particles and only increases their mass and size. As soot particles grow, due to the flame structure, flow rate, and buoyancy forces, they contact and attach to each other which leads to agglomeration and coalescence. In the case of coalescence, two approximately spherical soot particles attach to each other and form one larger particle

which is spherical. Therefore, the number of particles starts to decrease while the overall mass of particles remains unchanged. Unlike coalescence, in agglomeration particles attach to each other, but do not merge into a single larger particle and form chain-like structures. Oxidation, as mentioned earlier, is the transition of hydrocarbon or carbon to CO_2, CO, and water. When carbon is partially oxidized and converts to CO, it will not participate in soot formation even in the fuel-rich region [110]. It is suggested that OH is the main oxidizer agent in fuel-rich conditions, and in lean conditions, both OH and O_2 play key roles. It is worth noting that oxidation occurs constantly, however, in some regions and conditions it is more effective due to a variety of conditions such as temperature and oxygen presence [110].

1.4.2 Soot characteristics

While there are environmental and health concerns about soot particles as they can trigger several illnesses, including cancer and respiratory problems, Soot formation is desirable under some circumstances. For instance, in some applications where a high heat transfer is targeted, having a large amount of intermediate soot, but very small amount at the exhaust (due to environmental concerns) would be beneficial [115]. Figure 3 illustrates a coflow ethylene flame with and without the nitrogen dilution. The nitrogen diluted flame forms less soot and hence is much less bright than the undiluted flame which generates a high amount of soot and, as a result, much luminous. During the oxidation process in diesel engines, the in-cylinder soot is luminous and thus a main source of radiant energy [116, 117]. Additionally, carbon dioxide, water vapor, and intermediate species during the combustion emit radiation, however its magnitude is much smaller than soot particles [118]. Therefore, soot particles are a major source of the efficiency

loss in diesel engines [119]. Depending on the engine operation conditions and soot conditions, soot radiation can cause an energy loss from 0.5-1% to 5-10% of the total released chemical energy [120, 121].

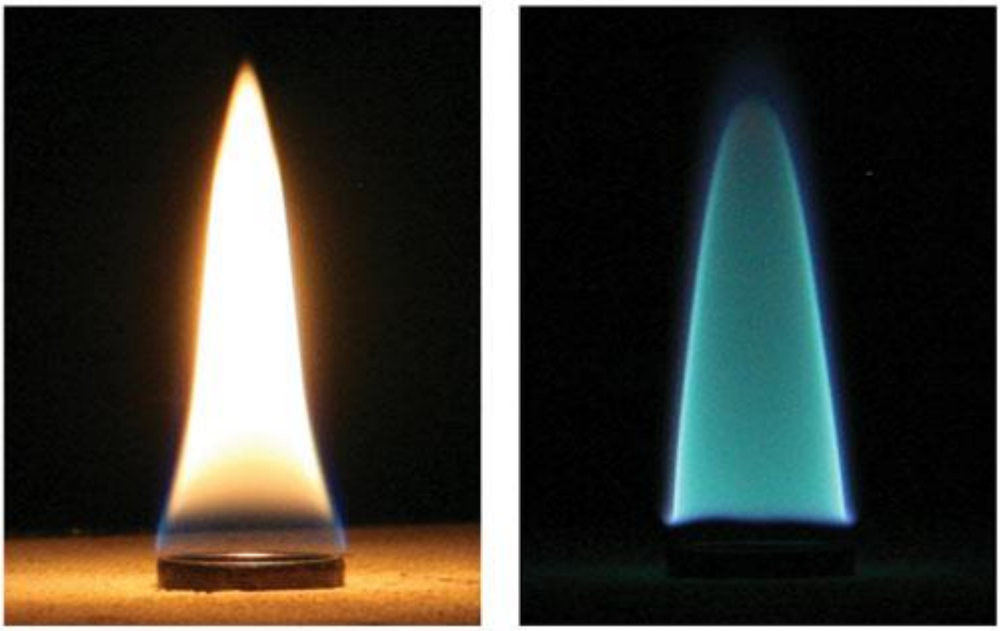

Figure 3. Two ethylene gas flames with and without the nitrogen dilution. The flame in the right is diluted with nitrogen and hence produces less soot. Soot increases the luminosity and radiant heat transfer of the left flame. To obtain the dimmer image on the right, the camera aperture had to be left open 30 times longer. (from [111])

Physical properties of soot such as density, porosity, and composition are similar to carbon black. Soot is generally nonporous except during the last stage of oxidation where has been observed to have a significant porosity [122]. the soot density is similar to that of carbon black which is in the range of 1820-2050 kg/m^3 [123]. The main component of soot is carbon with the following mole ratio ranges: C:O of 58-109, C:H of 8.3-18.3, C:N of 292-976 depending on the fuel and combustion conditions [122]. In some cases (e.g., diesel engines at heavy sooting conditions) soot can also comprise high levels of volatile matter [124].

Soot and carbon black (manufactured soot with high carbon purity) have many industrial applications due to their unique characteristics. For instance, carbon black as a filler can replace more expensive binder materials. It also can enhances the tear strength, improve the modulus and wear characteristics of the tires, and expand the tires life by conducting heat away from the tread and belt area [125]. Additionally, carbon black is an important pigment in xerographic toners since it can maintain a suitable level of electric charge on the toner which is crucial for electrographic copiers and printers to operate properly [125]. Carbon black has numerous other commercial applications such as in sensors, fuel cells, sodium and lithium batteries, and electronic equipment [126-129].

2 Motivation and Background

2.1 Engine-generated soot studies

Due to the impact of soot particles on the environment and human health, there have been numerous studies on the characteristics and formation of soot emitted by diesel engines because of their high soot emission. Several studies have been tried to establish effective methods to measure soot emitted by the engines. For instance, various soot measurement techniques such as in-cylinder [130], lift-off length [131], planar time-resolved [132, 133], two-color [134] and line-of-sight measurements have been used in order to obtain more reliable and accurate results. Moreover, the subject of how soot formation is influenced by different fuel structures has drawn many attentions. For example, the effect of aromatics on soot has been a topic of interest. Initially, it was suggested that aromatics can considerably contribute to soot emission level [135] while later, the reverse was reported, stating minor contribution of aromatics on soot emission [136]. However, it was reported afterwards that the influence of aromatics can alter based on the engine emitting level. That is, in engines with low emitting level, soot emission would not be significantly affected by aromatic addition contrary to high-emitting engines where aromatic addition can make a huge difference [137]. Fuel molecular structure (e.g. having straight or branched structure) can also affect the soot formation. It has been reported that a fuel with more branched molecular structure and even with lower distillation temperatures, aromatic content, density, and sulfur content which are expected to reduce the soot formation, produces a higher amount of soot implying the significant influence of molecular structure on soot formation [138, 139].

The effects of oxygenated fuels have also been studied considerably; e.g. it was announced that ethers are more effective in reducing soot particles than alcohols [140], and glycol generates less soot compared to other ethers with the same amount of oxygen composition [141]. Furthermore, there are many other parameters affecting the soot formation and characteristics emitted from engines such as combustion chamber geometry, injection timing, engine transient, intake pressure and temperature, etc. which have been investigated in detail [110]. The combustion chamber geometry can affect the soot formation by altering the swirl and liquid fuel impingement. Swirl, which is an organized rotation of the charge about the cylinder axis, can increase the turbulence and mixing leading to a higher rate of combustion late in the injection and after the injection which enhances the soot oxidation and reduces the amount of soot. However, having a too high swirl can cause the jets to hit each other before hitting the cylinder wall slowing the combustion and soot oxidation [110]. Injection timing can have a significant effect on both soot and NOx emissions. Generally, a retarded timing leads to a higher amount of soot but lower NOx while an advanced timing results in less soot but higher NOx [110, 142]. In diesel engines, the higher intake temperature enhances the in-cylinder soot formation but at the same time increases the oxidation more significantly leading to less soot at the exhaust [143]. Additionally, an increase of the intake pressure can reduce both in-cylinder and exhaust soot by increasing the charge air amount entered into the jet and improving the mixing rate [110].

2.2 Biodiesel impact on diesel engines

There have been numerous studies investigating the effects of biodiesel and diesel/biodiesel blend on the engine performance and emissions. Generally, it is accepted that biodiesel can enhance the start of combustion due to its higher cetane number compared to diesel fuel [78, 79, 144]. However, several biodiesels made from waste cooking oil, palm, and rapeseed have shown to increase the ignition delay compared to conventional diesel due to their higher viscosity [80, 81]. Moon et al. [82] observed a slower needle speed and decreased flow performance of the injector in case of biodiesel (due to the high viscosity) than diesel by means of X-ray phase-contrast imaging. Hwang et al. [83] reported the higher viscosity of biodiesel (waste cooking oil) to be responsible for the smaller injector spray angle compared to diesel resulting in the poor air entrainment and higher Sauter mean diameter. Regarding the equivalence ratio, Mohan et al. [78] observed a leaner equivalence ratio along the axis of the fuel spray of biodiesel compared to diesel due to the presence of inherent oxygen in the molecular structure.

The lower heating value of biodiesel can reduce the torque and power of diesel engines. Kaplan et al. [84] showed a torque and power loss of 5% to 10% based on the engine load in the case of sunflower-oil biodiesel compared to traditional diesel. Similarly, Cetinkaya et al. [145] and Lin et al. [146] reported a torque loss of 3% to 5% and 3.5%, respectively, when burning pure biodiesel (waste-oil and palm-oil biodiesels respectively) in a diesel engine. However, there have been some studies reporting higher torque for biodiesel than diesel due to several reasons mostly related to viscosity [65, 85, 86]. Brake-specific fuel consumption which is the ratio of mass fuel consumption over the brake effective power, can be increased by around 14% when biodiesel is used instead

of diesel [65, 87, 88]. The lower heating value and oxygen content of biodiesel are responsible for the higher fuel consumption as stated by Graboski et al. [87]. However, the thermal efficiency of diesel engines has been reported not to vary significantly with the use of biodiesel [89-91].

Using biodiesel can contribute to a higher NOx emission of diesel engines in most cases [69-71] while there are some studies reporting the NOx increases only in certain operation conditions [72-74] and others reported a decrease in NOx with the use of biodiesel compared to diesel [75-77]. Biodiesel can also significantly decrease the total hydrocarbons emission of diesel engines compared to diesel fuel [73, 147-149]. However, there are a few studies in the literature reporting a similar [72, 150, 151] or higher [74] hydrocarbons emission for diesel engines running by biodiesel. Lower biodiesel concentrations have been reported to reduce the hydrocarbons emission more effectively. Last et al. [152] studied various soybean biodiesel concentrations and reported a total hydrocarbons emission reduction of 28%, 32%, and 75% for 10%, 20%, and 100% biodiesel concentration, respectively. The total hydrocarbons emissions reduction is not affected significantly by changing the operation load of diesel engines burning biodiesel [77, 153]. Several reasons such as oxygen content, higher cetane number, lower final distillation points, and advanced injection and combustion timing have been suggested for total hydrocarbons reduction with biodiesel [154-157]. Regarding the CO emissions, it is widely accepted that biodiesel reduces the CO emissions considerably when used as the diesel engine fuel [154, 155, 157] while a few researchers reported no significant difference [72] and even higher [74] CO emissions for biodiesel. Biodiesel percentage did not affect the CO reduction as reported by Last et al. [152] who studied various

concentrations of soybean biodiesel in a heavy-duty diesel engine. Substituting diesel with biodiesel and their blends in diesel engines has been known to decrease the soot emission significantly [63-66]. Haas et al. [158] reported a 20% soot reduction with 20% blends and 50% soot reduction with pure biodiesel. The engine operation conditions can also affect the soot emission. For instance, it has been reported that the highest soot emission reduction occurs at high load operation conditions [74, 152, 159, 160]. The reason for that is because at high loads the combustion process is mostly diffusive and hence the oxygen content of the biodiesel can be more effective in decreasing the soot emission since particles are primarily produced during the diffusion combustion [160].

2.3 Flame-generated soot studies

The study of soot formation in engines is indeed helpful and essential since vehicles represent one of the most important forms of transformation and are also considered heavy soot emitters. However, soot particles collected from the exhaust of an engine are the final products of soot evolution and are known as “mature soot” (Figure 4). Obviously, mature soot cannot provide enough information on the evolution mechanism and each step of soot formation and oxidation. In order to understand the underlying process of soot formation, another combustion configuration needs to be employed. Among various configurations, a laminar cow-flow diffusion flame has shown to be a great medium to study different stages of soot formation and oxidation with several advantages including having a multi-dimensional structure and being easier to be analyzed and modeled compared to turbulent flames [161]. Additionally, direct soot sampling (e.g. inside a flame) has several advantages over exhaust collection (e.g. from

engine tailpipe) such as prevention of condensation, dilution, and aggregation in the exhaust [162].

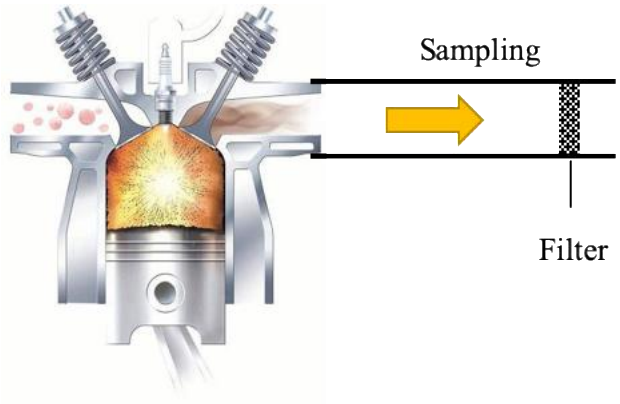

Figure 4. The common method of studying soot particles by trapping them at the engine exhaust. This sampling method only captures the final product of soot, "mature soot", and does not provide comprehensive information on soot formation mechanism. Engine schematic from [163].

The employment of a flame provides the opportunity for an easy extraction of soot particles from different positions that could be related to different soot evolution stages (Figure 5). In this configuration, for instance, the low, middle and upper part of the flame would be related to the soot inception, growth and agglomeration, and oxidation regions, respectively. Therefore, by sampling from different regions of a flame, different soot evolution processes can be studied separately (Figure 5). Consequently, numerous studies have focused on studying soot morphology and evolution process in laminar diffusion flames [164-170].

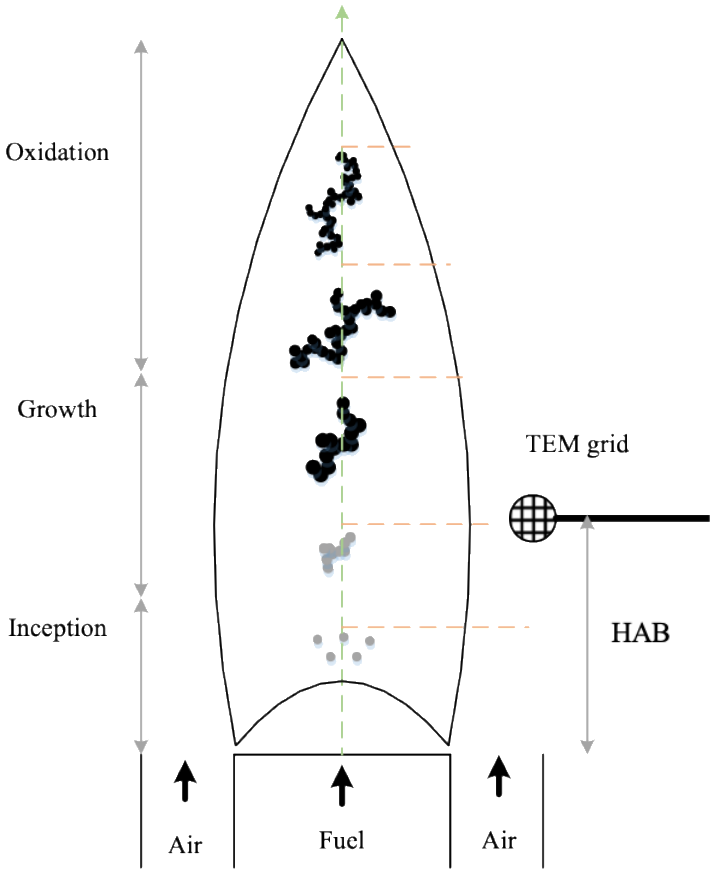

Figure 5. Schematic of a coflow diffusion flame illustrating different regions of soot formation inside the flame and collecting technique. TEM grid can be inserted into various heights above the burner (HAB) to capture soot particles.

Dobbins et al. [167] perfected the thermophoretic sampling technique to study the morphology of flame-generated soot particles. They employed an ethane diffusion flame and tested various probes to obtain the best quality TEM and SEM images revealing the soot morphology and agglomeration. It was reported that at the intermediate region of the flame, the maximum primary particles size and the maximum degree of branching occurs at the same radios as the maximum soot volume fraction. Lee et al. [169] investigated the soot formation effects of various oxygen concentrations in the oxidizer stream of a laminar diffusion methane flame. Air, 50% O_2, and pure O_2 have been introduced in the oxidizer stream to observe the soot formation alteration. A decrease in the flame height

was reported by increasing the oxygen concentration in the oxidizer. The soot primary particles were found to be similar in size in the case of air and 50% O_2 while the primary particles in the case of pure O_2 were smaller than the others by a factor of 2. The TEM images obtained in the two above studies ([167, 169]) were analyzed by Yazicioglu et al. [170] in order to measure the fractal properties of soot particles. The fractal dimension was calculated to be between 1.65 and 1.75 and the prefactor to be from 6.75 to 8.47. Ying et al. [171] studied the nanostructure of thermophoretically sampled soot from normal and inverse diffusion flames by means of HR-TEM. It was reported that the addition of n-butanol to the ethylene fuel can result in weaker soot carbonization and more amorphous structure. Moreover, hollowed and shell-like particles were found inside the normal diffusion flame indicating internal burning. Lapuerta et al. [172] investigated the soot morphology in a laminar coflow diffusion flame fueled by biodiesel surrogates. The size of the primary particles and agglomerates was observed to increase from the lower part of the flame until around two-thirds of the flame height and decreased afterward due to the dominance of oxidation. The presence of double bonds at the edge of the fuel molecule showed to increase the oxidation reactivity while at the center of the molecule enhance the PAH formation.

2.4 Thesis objective

The main objective of this work is to investigate the effects of neat biodiesel and biodiesel/diesel blending on soot characteristics and evolution process. Soot particles are extracted from different regions at the centerline of a coflow laminar diffusion flame. The flame is formed by #2 diesel, three popular biodiesel, and biodiesel/diesel blending with three different concentrations. Low-resolution TEM images of soot samples are employed for observation of the soot evolution process and also for characterizing the morphology (primary particles diameter, fractal dimension, branching, etc.) of soot aggregates. The internal structure of soot particles is investigated by high-resolution TEM images and several nanostructure parameters (fringe length, spacing, etc.) are obtained by image processing technique. Having morphological and structural information of soot particles allows to better understand soot evolution process and its impact on human health and environment and also to design after-treatment devices more efficiently.

3 Experimental Approach

3.1 Coflow burner

A slightly modified version of the coflow burner developed for methane/ethane flame by Santoro [173] is used in this study. The coflow burner is mounted on two-dimensional UniSlide assemblies (MA 6000) built by Velmex Inc. and has a stepping motor controller of 8300 series (Figure 6). An X-Y assembly of two UniSlides allows to move the burner in both X and Y direction (Figure 6). A personal computer with the COSMOS V3.1.4 (Computer Optimized Stepper Motor Operating System) software is employed to control the burner and move it in two axis planes with high precision (0.0000625 inches). The burner is composed of two concentric pipes which have a diameter of 11 mm and 82 mm, respectively. The central pipe is designed for supplying the vaporized fuel and the outer pipe supplies the oxidizer (Figure 7).

The oxidizer flow is introduced into a vacant chamber in the bottom section of the burner separated by a stainless-steel mesh which contains a bed of glass beads with a diameter of 3mm, and above that a ceramic honeycomb unit (51mm thick) in order to render the oxidizer flow and make it stable and uniform. Liquid fuel (biodiesel/diesel) is introduced at the rate of 6 ml/h into a pre-vaporization chamber by a syringe pump.

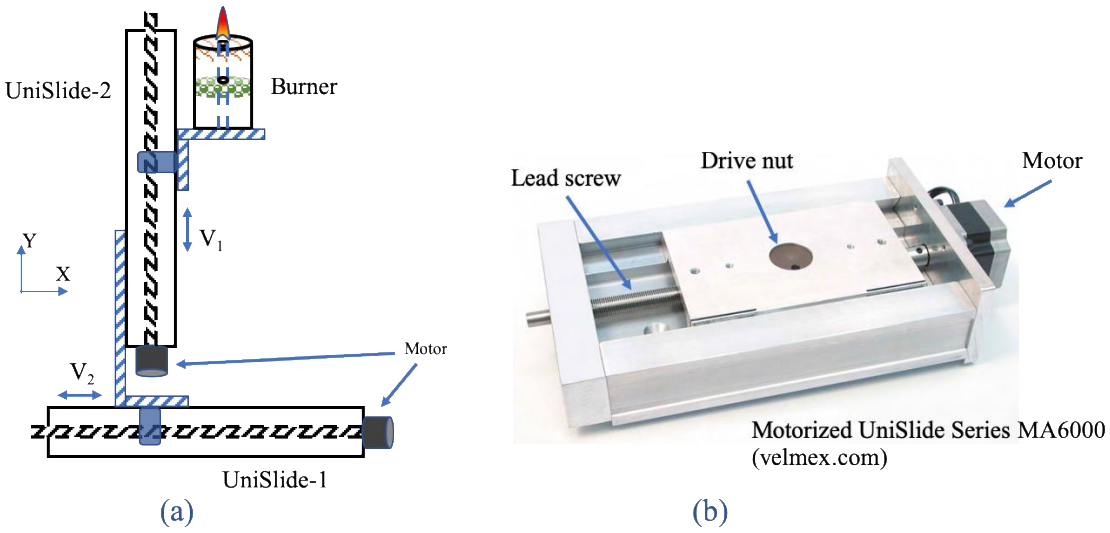

Figure 6. The 2-D positioner configuration (a), and the closed-up view of a UniSlide (b) employed in the experimental procedure.

The temperature inside the chamber can be continuously monitored and maintained at the preferred value to evaporate the fuel. The vaporized fuel travels toward the inlet of the co-flow burner within a heated and insulated pipe. Three heating tapes set to 350, 475 and 500 Celsius are employed to heat the walls of the evaporator and fuel line. The liquid fuel is pumped into the pre-vaporization chamber maintained at 350 Celsius.

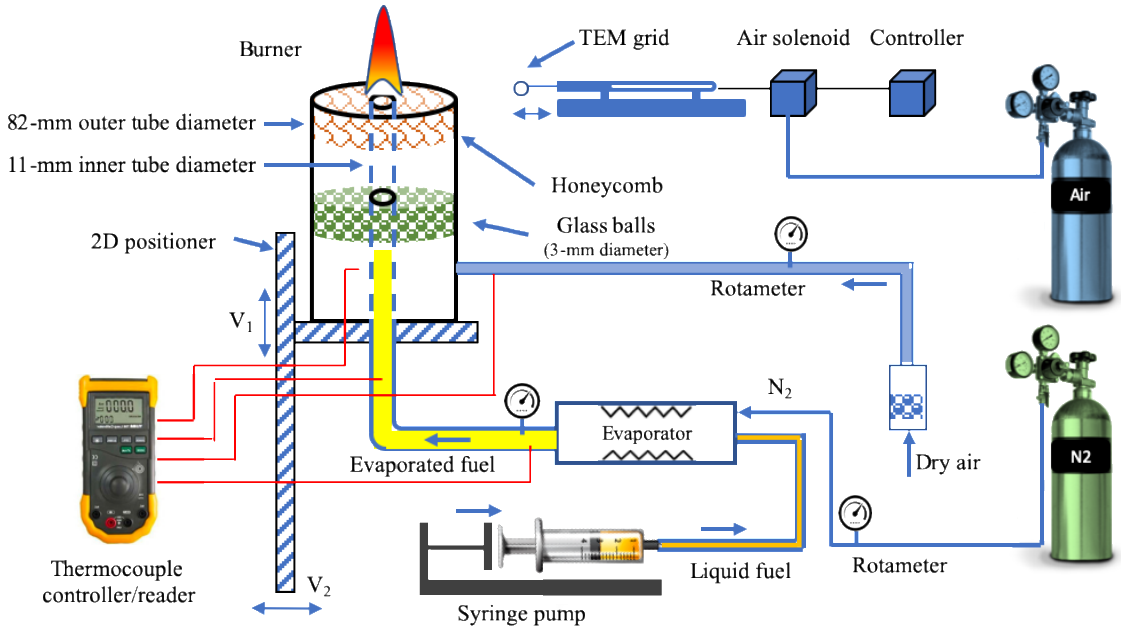

Figure 7. Schematic of the experimental setup used to study soot formation using thermophoretic sampling technique from vaporized (pre-heated) biodiesel/diesel air flames.

3.2 Studied biodiesels

The studied fuels consist of canola methyl ester (CME) (Milligan Bio-TECH Inc), soy methyl ester (SME) (Northeast Nebraska Biodiesel Inc.), cotton methyl ester (COME) (Southwest Energy & Feed, LLC) and #2 diesel (local gas station). The blends consist of B80 (80% CME /20% #2 Diesel), B50 (50% CME/50% #2 Diesel) and B20 (50% CME/50% #2 Diesel).

While diesel is mainly composed of aromatic content and saturated hydrocarbons, biodiesel is composed of unsaturated hydrocarbons. SME is composed of methyl palmitate ($C_{17}H_{34}O_2$), methyl stearate ($C_{19}H_{38}O_2$), methyl oleate ($C_{19}H_{36}O_2$), methyl linoleate ($C_{19}H_{34}O_2$) and methyl linolenate ($C_{19}H_{32}O_2$) with 13%, 5%, 25%, 52%, and 5% weight percentage, respectively [174]. CME is composed of the same fatty acids with different concentrations: methyl palmitate (5%), methyl stearate (3%), methyl oleate

(62%), methyl linoleate (20%) and methyl linolenate (10%) [175]. The chemical structure of COME along with several other well-known biodiesels are listed in Table 2.

Table 2. Fatty acids weight percentage of various biodiesels.

Fuel	Methyl Palmitate (%)	Methyl Stearate (%)	Methyl Oleate (%)	Methyl Linoleate (%)	Methyl Linolenate (%)	Ref.
SME	13	5	25	52	5	[174]
CME	5	3	62	20	10	[175]
COME	23	3	19	54	1	[176]
Sunflower Methyl Ester	6	5	20.5	68	0.5	[177]
Palm Oil Methyl Ester	40	4	43	10.5	0.5	[178]
Peanut Methyl Ester	10.5	9	47	33	0.5	[176]
Corn Methyl Ester	12	2	27.4	58	0.6	[179]

As it is clear from Table 2, unlike methyl stearate and linolenate, methyl palmitate, oleate, and linoleate seem to be the main fatty acid components of biodiesels. Among the three major components, methyl linoleate has the lowest cetane number, freezing point, and kinematic viscosity while methyl palmitate has the highest cetane number and freezing point, and methyl oleate has the highest kinetic viscosity [180, 181]. Methyl linoleate is the predominant ester in SME and COME while methyl oleate is the predominant ester

in CME (Table 2). That is why the SME and COME have higher cetane number and lower kinematic viscosity than CME (Table 1). Despite having 54% methyl linoleate, COME shows higher cloud point than CME (Table 1) which is probably due to the 23% methyl palmitate with the highest freezing point.

3.3 Thermophoretic sampling technique

A thermophoretic sampler is employed to insert TEM grids inside the flame and extract soot samples. Thermophoretic deposition is due to the temperature difference between the cold surface of the grid and the hot flow inside the flame. As the room-temperature TEM grid is inserted in the high-temperature medium of the flame, particles tend to deposit and freeze on the carbon film. The residence time of the grid inside the flame should be long enough to capture the particles, but not too long to lose the temperature gradient [167]. The height above the burner used in this study represents the axial distance from the mouth of the burner to approximately the center of the TEM grid inserted inside the flame volume. The thermophoretic sampler utilized here is similar to the one developed by Megaridis and Dobbins [167, 182] to capture particles directly from inside the flame's yellow luminous zone. Samples of carbon particulates are collected on the surface of a transmission electron microscopy grid. The grids are made of Cu with a film of carbon on their surface (EMS, Inc.). The TEM grid gains its movement from a 50 mm stroke compressed-air piston controlled by a pneumatic valve (Model SY5140, SMC Corp. of America) (Figure 8) with a residence time of 38 ms inside the flame and approximately 10 ms for the grid's travel time. The soot samples were studied by a high-resolution electron microscope (JEOL TEM-3010), operated at 200 KeV with a LaB6

filament. The TEM micrographs were collected on a Gatan digital imaging system and processed by digital micrograph software.

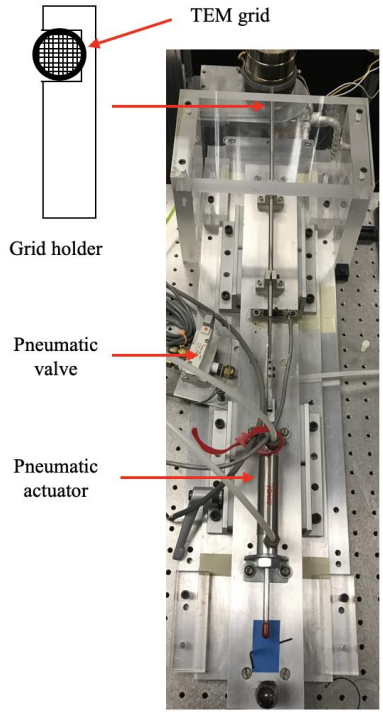

Figure 8. The thermophoretic sampler employed in this study to extract soot samples from various locations inside the flame.

4 Soot Formation and Evolution Profile Inside the Studied Diffusion Flames Burning Diesel, Biodiesel, and Biodiesel-Diesel Blending

In this chapter, the evolution profiles containing physical characteristics of soot in vaporized coflow diffusion flames along the flame centerline are reported. The profiles are obtained using transmission electron microscopy (TEM) on the collected samples revealing the sequence of the morphological changes within a flame axial direction. The studied vaporized flames are formed using three types of neat biodiesel (B100), blends (B20, B50, and B80), and #2 diesel (B0) flame. The evolution profiles contain information on the morphology of the soot particles (agglomeration, size and nanostructure) present at the different stages within the studied flames. All soot samples are collected thermophoretically from the flame's centerline at different heights above the burner (HAB).

4.1 Soot formation in diesel air-flames

TEM images of soot samples from different regions of the flame can be very helpful in order to understand the evolution process of soot particles. Figure 9 depicts the morphological characteristics of carbon particulates present in the evaporated #2 diesel-air flame at different heights above the burner (HAB) in the axial direction. The evolution presents the different stages in the carbon particulates formation. The set of lower resolution TEM images provides information of particle agglomeration (density of particle per aggregate) at various flame heights (Figure 9 a1-e1). The set of higher magnification TEM images are useful for measuring the primary particle diameters (d_p) (Figure 9 a2-e2). As indicated by the TEM images, the diameter of primary soot particles,

degree of agglomeration or density of primary particles forming the aggregates strongly depend on the flame position. In the upper part of the flame, the characteristics of the carbon particulates are governed by long and branched aggregates, while in the lower part of the flame the characteristics of the carbon particulates are dominated by singlet particles and small aggregates formed by a smaller number of primary particles. TEM images of particles collected from the lowest sampled height of the flame (HAB of 6mm) (Figure 9 a1) illustrate the presence of mostly singlet particles. The particle diameter at this HAB appears to be of a polydisperse diameter size distribution (Figure 9 a1). In the literature such singlet particles are typically referred to as soot "precursors" or "young soot". They are more transparent and have lower contrast in TEM images (Figure 9 a1-2). Such structures have been reported in a number of studies, both in premixed [183] and diffusion [184] flames. Now it is quite accepted that these low-contrast particles are associated with the presence of aliphatic hydrocarbons [185-187] due to their higher H/C ratio compared to aromatic hydrocarbons, and the lower the H/C ratio is, the more solidified the particles. The peak value of d_p for the diesel-air flame is approximately 39 nm and is located at the HAB of 15 mm. The d_p increases due to the coalescence and surface growth as soot precursors/aggregates move from the lower to the upper region of the flame. Subsequently, the d_p falls from 39 nm at the HAB of 15 mm to 21 nm at the HAB of 33 mm. This reduction in the soot diameter size in the upper region of the flame is due to the oxidation or destruction process. It is also interesting to note that the most severe increase in the degree of primary particle agglomeration starts at the height of 15 mm, which can be considered approximately half of the flame length. At the HAB of 15 mm the soot aggregates are shorter and of higher density and are surrounded by spherical

singlet particulates (Figure 9 c1). As it is illustrated by Figure 9, at approximately the middle part of the flame, carbon aggregates are accompanied by a few particulates that appear to be less opaque and do not have a clear shape and sharp boundaries (Figure 9 c1). Structures with this type of characteristics are known in the literature as “liquid-like”. The presence of these “irregular-shaped” or “globules” structures in the soot evolutions can be attributed to the soluble organic fraction (SOF). This will be discussed later in this chapter. High resolution TEM (HR-TEM) was applied to study the nanostructure of the samples collected from the different stages within the flame. A simple inspection of the low resolution TEM images in Figure 9 a1 reveals the presence of very large and smaller particles forming the samples. The nature of the inner structure at this HAB (tar-like material) allows ease for the particles to fuse and form larger particles. Carbon particulates composed of ordered graphite structure are evident in the intermediate and mature soot present in the upper regions of the flame. At HAB of 15 mm the primary particles forming the aggregates are composed of clearly distinguishable graphitic layers. These zones represent higher local temperatures within the flame volume and significantly modify the soot’s inner structure.

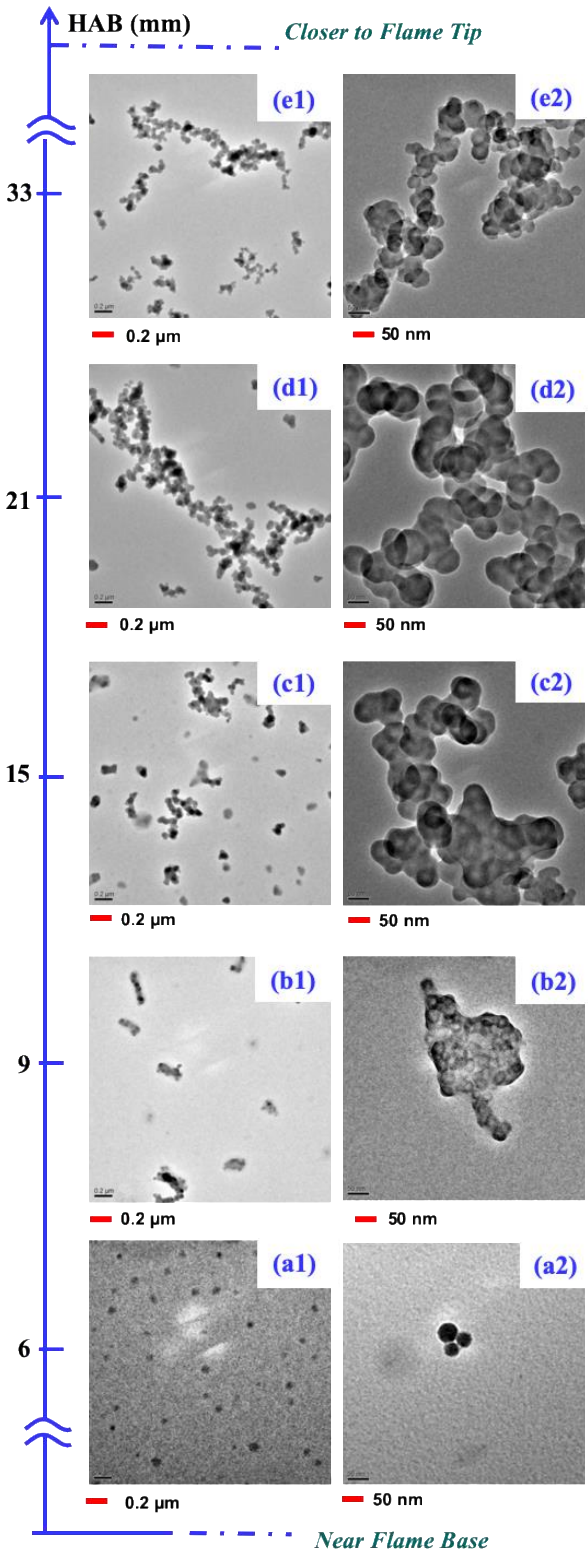

Figure 9. Representative progression of the soot evolution in an evaporated diesel-air flame through a series of low and higher-resolution TEM images taken from samples extracted along the central axis of the flame at various heights above the burner (HAB).

4.2 Soot formation in biodiesel air-flames

Figure 10 displays the typical morphological characteristics present in soot particles extracted from different axial locations inside the evaporated CME-air (Figure 10 a1-a4), COME-air (Figure 10 b1-b4) and SME-air (Figure 10 c1-c4) flame. Similar to the #2 diesel-air flame, in the biodiesel air flames the sampling was performed in the post flame region at various HAB on the axial direction.

The overall flame length of the tested biodiesel-air flames is significantly shorter compared to that of the Diesel-air flame (33 mm). The highest sampling point for the CME and COME air flames was 21 mm, while for the SME it was 25 mm but still shorter than the diesel flame. Therefore, the rates of soot formation and evolution (soot inception, growth, and oxidation) of the biodiesel-air flames are much stronger (Figure 10). The carbon particulate growth mechanism in the tested biodiesel-air flames follows the same general trend as in the diesel flame. That is, precursors lead to the formation of "young" and "mature" soot particles by means of coalescence and surface growth. However, a visual comparison between the soot evolution profile of the diesel (Figure 9) and the biodiesel flame profiles (Figure 10) reveals that there are some interesting differences and characteristics in the soot morphology. At the flame height of 15 mm the presence of large "irregular-shaped" fragments containing complex structural morphology is evident in the biodiesel flames (Figure 10 a3, b3, c2). The characteristics of the soot at the HAB of 21 mm (CME and COME) and 25 mm (SME) (sampled at the highest position in the flame) indicate that they are composed predominantly of highly elongated and branched aggregates (Figure 11 a4, b4, c4). For the #2 diesel flame, the "irregular" structures are not broadly evident.

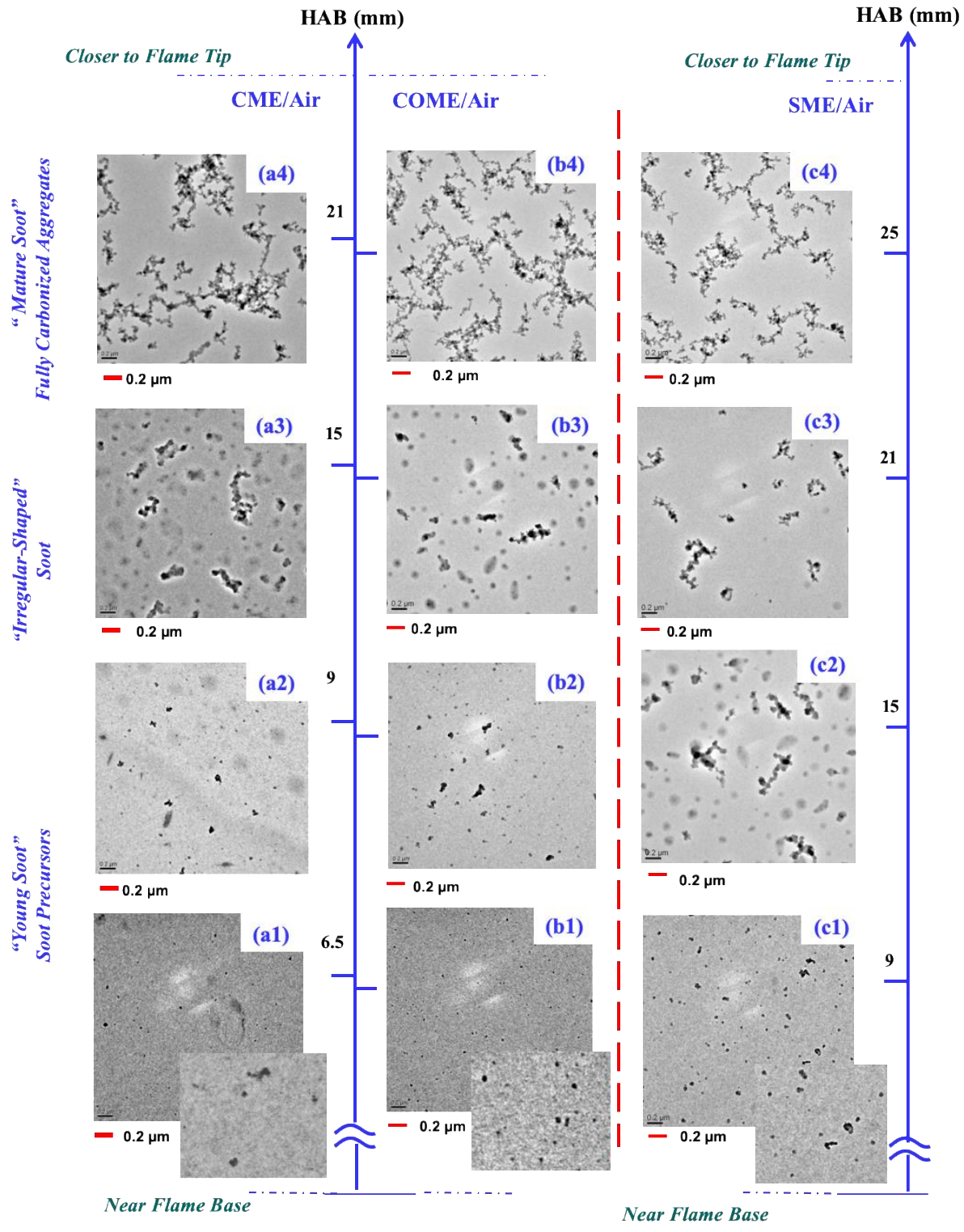

Figure 10. Representative progression of the soot formation and evolution present along the central axis of three (B100) evaporated biodiesel formed flames. Particles were sampled at various heights above the burner (HAB): 6.5, 9, 15, 21 and 25 mm from the burner's mouth. (a1–a4), (b1–b4) and (c1–c4) represents the soot evolution of the CME, COME and SME air flames, respectively.

Only a few "globules" are present in the diesel soot evolution (Figure 9 c1) showing that the presence of these structures is more pronounced in the biodiesel vaporized flames.

The evolution profiles with close-up views of the soot from the CME, COME and SME are presented in Figure 11 a1-a4, b1-b4 and c1-c4, respectively. For the CME-air flame the d_p is measured to be approximately 15 nm and 18 nm at the HAB of 6.5 and 9 mm, respectively (Figure 12). The peak value of the d_p is ~28.5 nm at the HAB of 15 mm, followed by an oxidation zone present near the tip of the flame (Figure 12). At the HAB of 21 mm, a d_p value of 21 nm was measured. The peak value of the d_p for the COME-air flame was found to be very similar to that of the CME-air flame. That is, a peak value of d_p of 27.5 nm was measured at the HAB of 15 mm for the CME-air flame. In the COME flame the average primary particle diameter ranged from 15 nm (6.5 mm HAB) at the lowest region of the studied flame to 19.5 nm (21mm HAB) at the highest studied flame position near the tip of the flame (Figure 11 b1-b4). Figure 11 (c1-c4) represents the physical evolution of soot present in a vaporized SME-air flame. TEM analysis conducted on soot samples at the HAB of 6.5 mm for the SME-air flame (lowest sample position) showed that the number density of precursors was nonexistent. However, at the HAB of 9 mm the presence of singlet particles is evident (Figure 11 c1). The average primary particle diameter for the SME-air flame ranges from 21 nm at HAB of 9 mm to 14 nm at HAB of 25 mm (Figure 12). The peak value of the d_p for this flame was measured as 30.5 nm at the HAB of 15 mm (Figure 12).

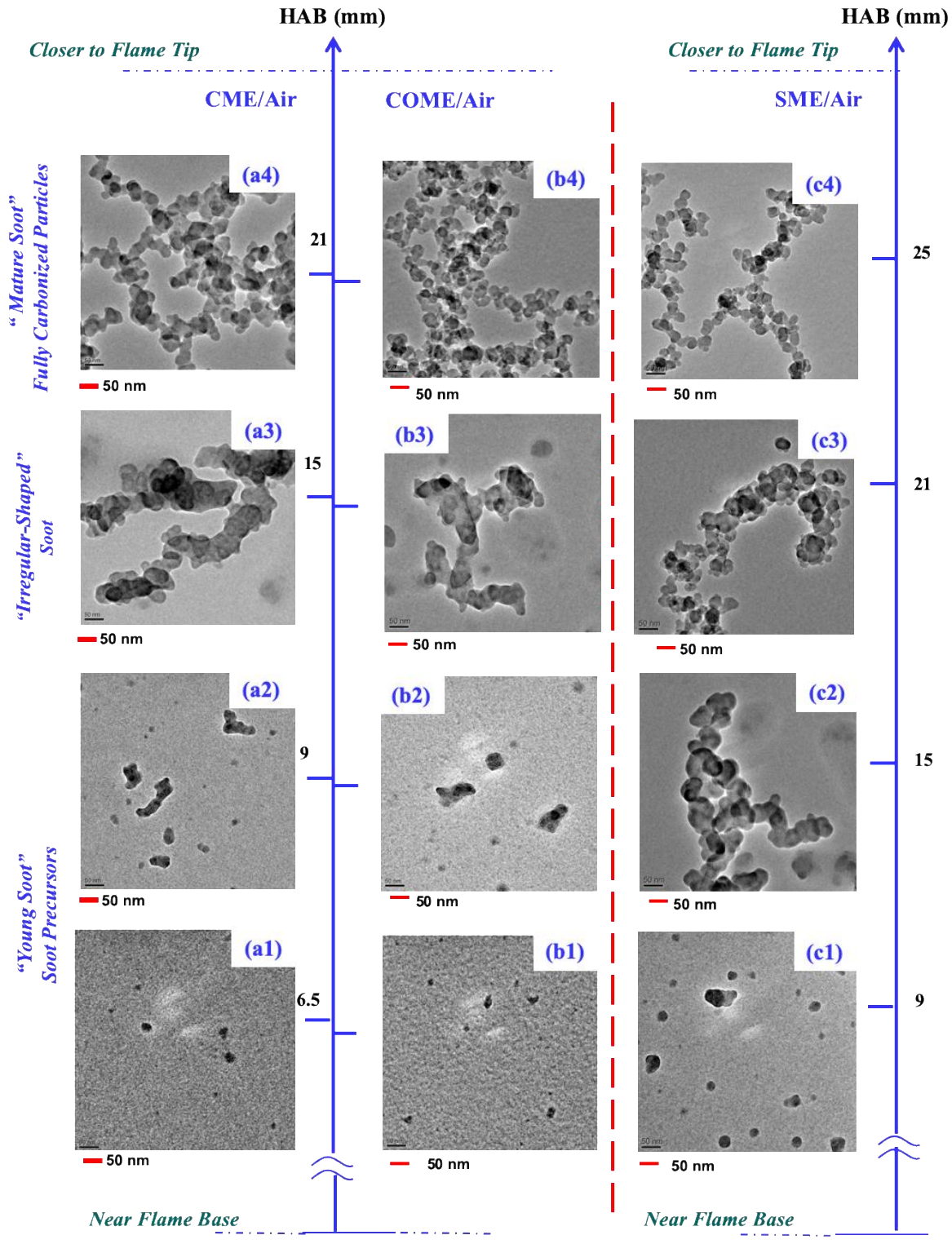

Figure 11. Close-up view of the representative progression of the soot formation and evolution present along the central axis of the three (B100) evaporated biodiesel formed flames. (a1–a4), (b1–b4) and (c1–c4) represent the soot evolution of the CME, COME and SME air flames, respectively. The magnified views allow for comparisons (within a flame and fuel type) of particle size diameter, morphology of soot, and primary soot particle size.

The "close-up" TEM views in Figure 11 (a1, b1, c1) of the tested vaporized biodiesel formed flames show that the soot precursors or "young soot" present at the lower region of the flame (close the fuel nozzle) have a polydisperse size distribution. It is also evident that the larger elements at this lower flame position are composed of more than one particle and are not necessarily spherical in shape (Figure 11 a).

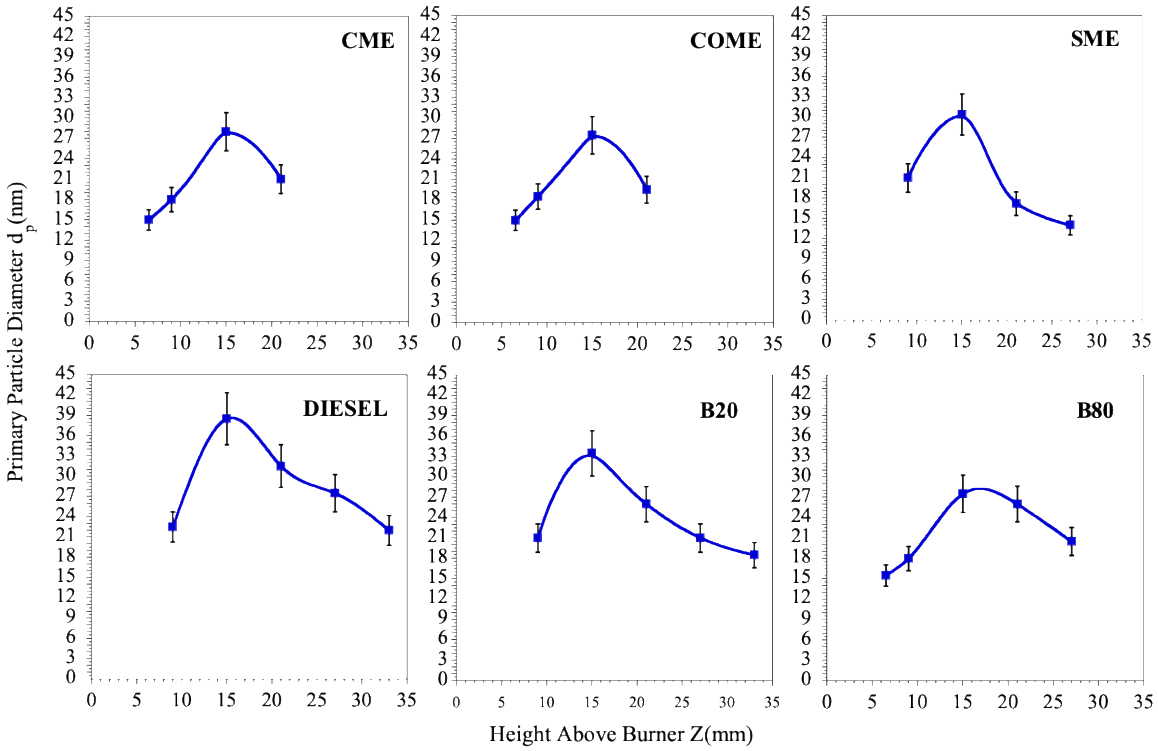

Figure 12. The plots represent the average primary particle diameter (d_p) with respect to the axial sampled heights for tested flames at different flame heights above the burner. Note that due to the particle size polydispersity (liquid-like structures) present at the lowest sampled position of the diesel and B20 flames, their corresponding d_p values are not provided. Also, the graph for B50 is not reported due to uncertain measurements.

It can be observed that the smaller the particles, the more spherical they appear to be under the electron beam. These precursors or "young soot" diameter size ranges from a few nm to tens of nm. Another interesting aspect of the TEM imaging analysis in Figure 11 is the details that they offer of the "irregular-shaped" particles. The "close up" TEM images show that in all of the three tested biodiesel flames, the soot aggregates are also

accompanied by “liquid-like” droplets or “globules” of significantly smaller diameters (<100 nm in diameter). Structural characteristics of such nature were not observed in our previous work when sampling carbon particulates from non-vaporized biodiesel and Diesel flames [102]. The flame length of the CME is very similar to that of the COME-air flame and in both flames the “irregular-shaped” fragments are formed at 15 mm HAB. However, for the SME-air flame the “irregular” fragments are present at 15 and 21 mm HAB. For the CME and COME air flames it can be observed that at 21 mm HAB the primary particles forming the aggregates are more spheroidal. The “close up” TEM views indeed reveal that the primary particles are diffuse and fully carbonized forming complex branched structures in the upper region of the flame (Figure 11 a4, b4, c4).

4.3 Different soot evolutions in diesel and biodiesel air-flames

From a comparison of the soot evolution of the #2 diesel (Figure 9) with the B100 profiles (Figure 10 and Figure 11) it is evident that the diameter of the primary particles forming the aggregates or “mature soot” in the diesel flame is considerably larger than the biodiesel flame. It has been suggested that the oxygen content in the biodiesel fuel ($C_xH_yO_2$) can contribute to a higher oxidation rate of the soot resulting in smaller diameter of the primary soot particles produced in the combustion of this fuel [65, 188-193]. For instance, the work of Song et al. showed that the carbon particulates from a neat biodiesel (B100) are more reactive during oxidation than soot formed with the counterpart diesel [193]. Zhang et al. [190] suggested the biodiesel fuel-bonded oxygen to be responsible for the hollowed soot structure leading to a higher oxidation rate. Omidvarborna et al. [191] also stated that the extra oxygen included in biodiesel leads to further oxidation and particle size reduction. The study of Barrientos et al. on soot produced in a co-flow

laminar diffusion flame formed with different types of fuels (including methyl esters, alkanes, biodiesel and diesel) showed the effect of fuel-bound oxygen in fatty acid esters on soot oxidation behavior using thermogravimetric analysis and Raman spectroscopy [188]. In that work it was suggested that the oxygen present in the oxygenated fuel leads to the formation of soot particulates with more active sites or with a structure allowing greater accessibility to the oxidation sites [188]. This could explain the smaller soot particle diameters in our biodiesel soot. However, higher oxidation rate in a biodiesel flame could not be the only reason for smaller particles, since oxidation is not profound in lower and intermediate regions of the flame. Soot particles in the diesel flame are considerably larger than those of biodiesel at any position of the flame implying that there is stronger surface growth in the diesel flame. While soot inception is an essential step in soot formation, it is mainly the surface growth that contributes to the overall mass of soot. Larger diameter particles could also be the result of a higher coagulation rate; however, surface growth is known to be responsible for smoothing the surface of the soot particles and yielding nearly spherical particles [194]. Since coalescence does not always form perfectly circular particles, surface growth is necessary in order to have spherical particles [195]. Figure 13 illustrates the outcome of the incomplete coalescence of two spherical particles which does not have a round shape, but surface growth can lessen the irregularity and make more spherical particles. The soot formation and evolution profile of the diesel flame (Figure 9) clearly shows that the primary particles are much more spherical and of smooth surface supporting the theory of more considerable surface growth. On the other hand, soot particles in the biodiesel appear to be far from spherical and of a greater surface roughness than those present in the #2 diesel. This is possibly due to poor surface growth

process while the surface roughness in the fully carbonized soot particles of the biodiesel appears to improve possibly due to oxidation (Figure 11 (a4, b4, c4)). Sulfur content in diesel could be another explanation of larger particles since it can increase soot particle size and mass by oxidizing and attaching to their surface [196]. Last but not least, acetylene is known to be the dominant soot growth species [110, 114, 197, 198], therefore different concentrations of acetylene could be an explanation for different soot growth rates. As reported by Smith [199] some acetylene is oxidized to rather inert products in the presence of oxygen. This could support the lower growth rate in biodiesel flames where the oxygen component of the fuel may oxidize some acetylene and consequently slow the surface growth process.

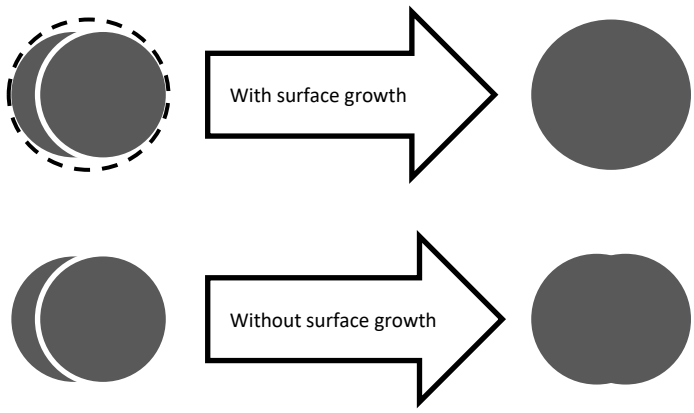

Figure 13. The effect of surface growth on circularity of particles after coalescence, a) coalescence with surface growth leads to a very circular particle, b) coalescence without surface growth leads to a less circular particle.

As Figure 9-Figure 11 illustrate, there are profoundly larger number of relatively small singlet particles (soot precursors) at the lower part of the biodiesel flame compared to fewer but much larger particles in diesel flame. It indicates that soot inception rate is extremely higher in case of biodiesel than diesel. Fuel pyrolysis is the key factor in soot inception since the products of pyrolysis will make soot formation possible, and also it

was reported that having small amounts of O, O_2, and OH might accelerate the pyrolysis due to the fact that many of its reactions happen by free radical mechanism [199]. Therefore, the oxygen content in biodiesel could be the reason behind the tremendously higher inception rate. The oxygen content in molecular structure of biodiesel fuel plays a key role in determining the flame height since it enhances the reactions and makes biodiesel flames much shorter that the diesel flame (about 33mm for diesel and 21mm for CME and COME). The effect of oxygen on the flame height is also well established from the oxygen-enhanced studies in which the height of the flame decreases with increasing the oxygen content in the oxidizer flow [175]. It is worth noting that having oxygen content could increase oxidation as well which might result to fewer soot particles, but in the low and intermediate part of the flame where the temperature is relatively low, oxidation is not as powerful as pyrolysis. Higher unsaturated content in biodiesel could be another factor contributing to the pyrolysis and, consequently, soot inception rate. Interestingly, having greater amount of aromatics, which are well known to be considerably important in nucleation process, did not lead to a higher inception rate for diesel, but it might be the reason for the lager nuclei. As it is illustrated by Figure 9-Figure 11, at the low and intermediate parts of the flame, soot particles are less opaque and do not have a clear shape and sharp boundaries. This “liquid-like” or “transparent” characteristic of soot particles at the first stage of soot formation has been reported in a number of studies, both in premixed [183] and diffusion flames [184, 200]. The term liquid-like is suitable since these soot particles do not act as solidified or rigid particles and deform (flatten) when sitting on the TEM grid. They also are more transparent and have lower contrast in TEM images. However, after undergoing the carbonization

process, all the soot particles and clusters become fully carbonized, rigid, and well defined as shown by TEM images from upper part of the flames. The liquid-like characteristic is attributed to the presence of aliphatic hydrocarbons [185-187, 194], since aliphatics have generally higher H/C ratio compared to aromatic hydrocarbons, and the lower the H/C ratio is the more solidified the particles are. Previously, the presence of aliphatics was not clear since most of the methods used for the purpose of investigating the chemical components of soot particles such as LMMS (laser microprobe mass spectrometry) [200], laser ablation particle mass spectrometry [201], and laser desorption/laser ionization mass spectrometry [202] were only able to detect aromatic hydrocarbons and not the aliphatic ones, probably because the laser fragmentation is too destructive for the less stable hydrocarbons (aliphatics). Thus, it was believed that soot particles are composed of aromatic hydrocarbons especially PAHs (polycyclic aromatic hydrocarbons). However, new methods such as HR-MS (high-resolution mass spectrometry) along with soft ionization [184] and micro-FTIR spectroscopy [203] and photoionization aerosol mass spectrometry (PIAMS) [204], recently managed to detect aliphatic hydrocarbons as well, which changed many aspects of soot formation and growth mechanism analysis. the transparent structures are less profound in the diesel flame which could be attributed to its high amount of aromatic component.

In the intermediate region of the flames, before soot particles/aggregates become fully carbonized, particles are covered by tar-like material or condensed hydrocarbons which has been attributed to the soluble organic fraction (SOF) [63, 64]. This tar-like cover is considerably more dominant in the biodiesel flame than the diesel, which is consistent with the higher SOF in biodiesel reported in the literature [63, 64, 205, 206].

The more dominant tar-like and droplet-like characteristics inside the biodiesel flames at the intermediate part of the flame could be also related to the soot evolution mechanism. Reilly et al. [207] suggested a new soot evolution mechanism considering large PAH-containing droplets including nuclei that grow and fuse together before carbonization, which seems very similar to the droplet-like appearance observed herein and in other reported works.

Figure 14 displays the soot evolution mechanism inside the CME flame which is similar to other biodiesel flames and is consistent with the mechanism suggested by Reilly et al. [207]. At the lower part of the flame (Figure 14 a1-2), only small singlet particles are present which turn to large droplet-like structures and globules a few millimeters upper in the flame (Figure 14 b1-b2). The large droplets containing singlet dark particles (nuclei) convert to more solid structures as a result of carbonization as traveling upward inside the flame (Figure 14 c1-2) where they are exposed to higher temperature and finally become fully carbonized near the flame tip (Figure 14 d1-2). However, that does not seem to be the only possible evolution mechanism because TEM images reported in many other studies [204, 208-212] and even in the case of diesel flame herein do not show the large droplets with nuclei and the halo-like feature. This observation suggests the other proposed mechanism by Lahaye [213] that soot precursors first carbonize and then fuse together and form aggregates. Kholghy et al. [214] studied two different streamlines in a diffusion Jet A-1 flame and reported that both mentioned mechanisms could occur based on different temperature profiles. In that study, they reported that the first mechanism, which is observed in biodiesel flames herein, occurred in the centerline of the flame where

soot precursors reach carbonization temperature later than precursors in annular streamlines where they first carbonized and then created aggregates.

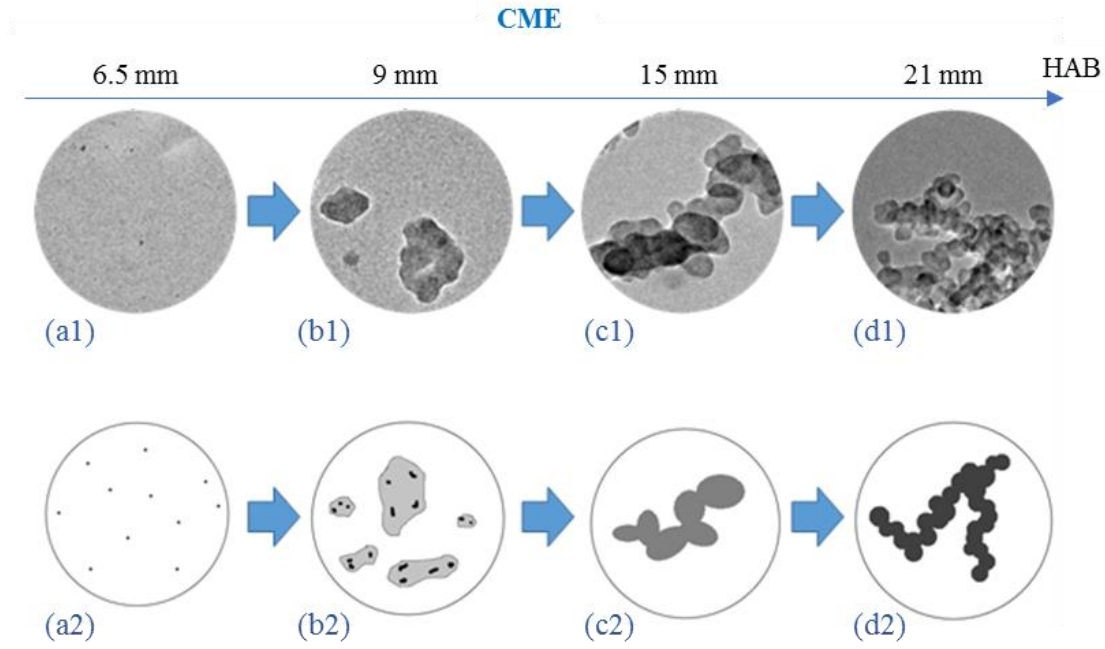

Figure 14. The soot evolution mechanism observed on the central axis of biodiesel flames (only CME is shown as an example). Original TEM images (a1-d1) along with their corresponding schematics (a2-d2) are presented to better observe the evolution mechanism.

Figure 15 is a detailed pictograph representation of the growth and carbonization process present along the axial direction of a vaporized # 2 diesel Figure 15 a-c and of a biodiesel flame Figure 15 d-f. COME is used as a representation of the soot evolution process taking place in a biodiesel flame. As discussed previously, the general progression of the soot formation for both the #2 diesel and biodiesel appear to be similar. However, it is evident from the soot evolution profiles that the upper part of the biodiesel flames is heavily composed of "irregular-shaped" or "globules" structures that have a "liquid-like" characteristics. While at the lower region of both Diesel and biodiesel flames the presence of soot precursors is evident. Although, soot precursors formed in

the Diesel flame (Figure 15 a5) appear to be larger in size compared to those formed in the biodiesel flame (Figure 15 d2). The effect of particle overlapping, necking, and the transition (overlapping/necking) of the neighboring singlet particles to form the larger soot "precursors" in the #2 diesel is evident (Figure 15 a1-a4). The particles appear to be composed of tar-like material as is apparent from the stretching of the material (arrow in Figure 15 a4). Figure 15 a4 shows three nearly spherical particles starting to fuse together. The fusing of these particles at this flame position may explain the polydisperse distribution of their sizes.

The spreading of a very large "irregular-shaped" structure from the COME flame after its impact on the surface of the carbon film is shown in Figure 15 d1. The shape indicates the viscous liquid nature of the "liquid-like" structure (Figure 15 d1). It is well established that several parameters can play a key role in the spreading of a droplet upon the impact on a surface, including the droplet size, velocity of impact, density, viscosity and surface tension along with some other physical characteristics present on the surface [215].

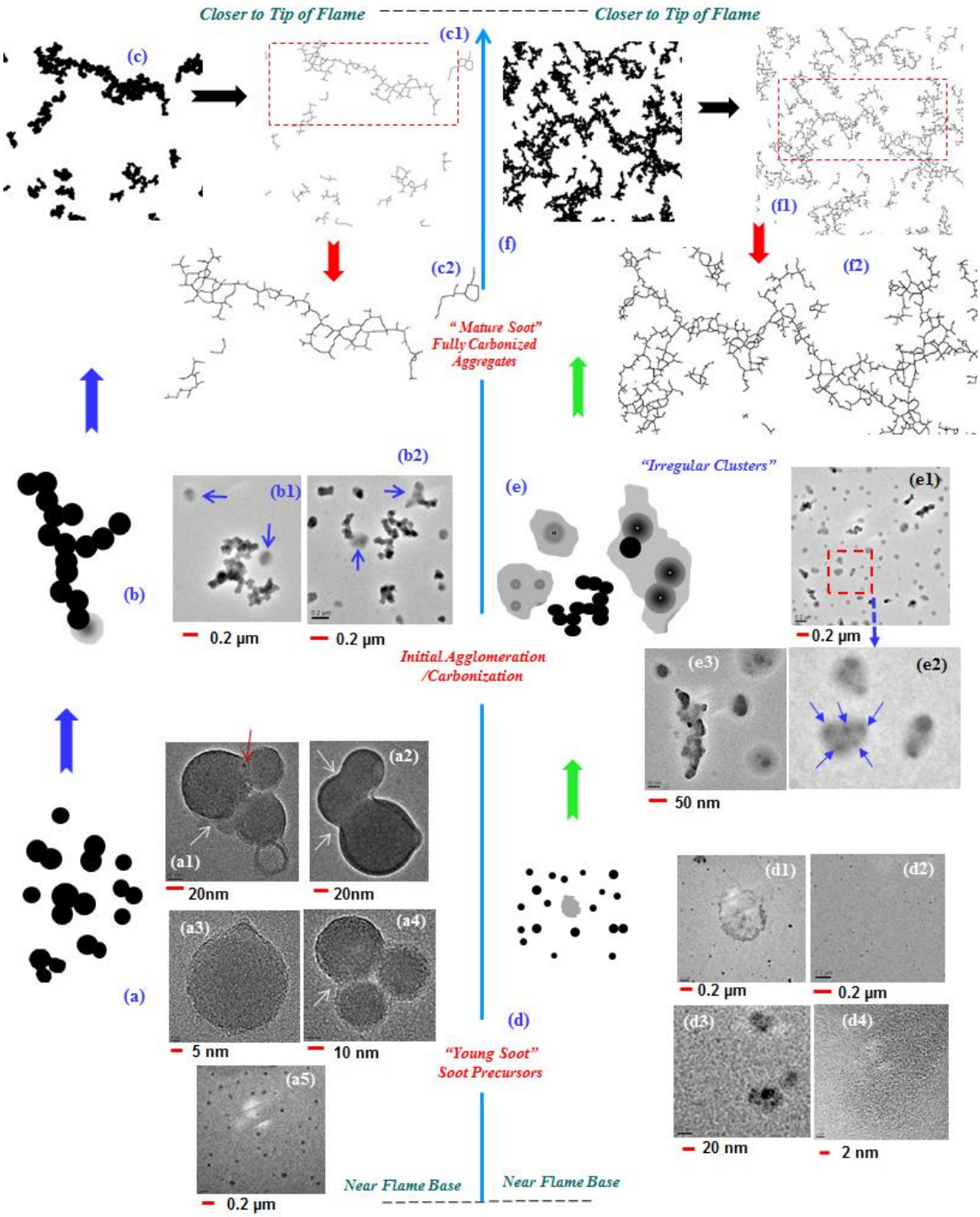

Figure 15. Schematics and TEM images depicting the soot formation and evolution along the central axis of a vaporized # 2 Diesel/air (a-c) and of a biodiesel (COME/air) (d-f) flame.

At approximately the middle height of the flame the soot produced by the biodiesel and diesel appear to be very different. For the #2 diesel flame the particle evolution is composed of soot of typical physical characteristics (Figure 15 b1-b2). That is, the aggregates are composed of fused primary particles that have well-defined boundaries and are nearly spherical in shape. Although, a closer look at the TEM images reveals that the aggregates are also accompanied by a few small size "globules" as pointed out by the arrows in Figure 15 b1-b2. However, for the biodiesel flame the soot evolution is composed of a higher number of "irregular-shaped" structures or "globules" (Figure 15 e1). The "irregular-shaped" structures contain embedded carbonized inclusions that can be easily identified as they have a darker contrast to the electron beam (Fig. 8 e2-e3). A single "globule" can have multiple embedded carbonized inclusions and of different sizes. For instance, one of the three clusters of Figure 15 e2 (close-up view of Figure 15 e1) have five nuclei inside as pointed out by the solid arrows. The transformation from "irregular-shaped" structures to fully carbonized (agglomerated) soot in the upper part of the biodiesel flames is evident in the TEM images for all studied flames in this work. From the soot evolutions it can be suggested that the "irregular-shaped" structures serve as possible growth pathways for the formation of long fully carbonized aggregates composed of nearly spherical primary particles. The carbonized aggregates are very long and of complex fractal morphology (multi-branched) and are no longer accompanied or formed of "irregular" structures (Figure 15 f). In order to visualize the complexity of these fully carbonized soot aggregates, binary images on the TEM micrographs of the COME (Figure 15 f) and #2 diesel (Figure 15 c) soot were obtained using a computer software. Skeletonization was applied to the binary images to obtain basic structural information of

the aggregates. Skeletonization is a repeating erosion process in which pixels from the edges of objects are removed (in a binary image) until a one-pixel-wide shape is reached [216, 217]. Figure 15 f1-f2 is for biodiesel and Figure 15 c1-c2 are for the #2 diesel. The binary images were developed with an optimal intensity threshold to prevent the creation of separations between the aggregates and to distinguish between aggregates boundaries and the background. For instance, the largest aggregate in Figure 15 f1 has a length of ~39 μm, boxed area in Figure 15 f1 with its magnified view in Figure 15 f2. On the other hand, the largest aggregate in the #2 diesel flame (Figure 15 c) has a length of ~8.0 μm. The difference in the degree of agglomeration and branched structures are much more profound near the flame tip than the middle region of the flame. The reason is that clusters in the middle region are relatively small since they just started to form, thus the dominant aggregation mechanism is the monomer-cluster in which the aggregates are formed by attaching single particles to an existing aggregate, leading to more compact structures. As the size of aggregates increase, the cluster-cluster become the dominant mechanism which considers the movement and attachment of aggregates together as the main path for aggregation leading to more branched and elongated structures. Cluster-cluster aggregation is dominant in the upper part of the flame where clusters have a considerable length.

4.4 Soot formation in blending (CME/diesel) air-flames

Similar to the studied neat biodiesel (B100) air flames discussed earlier in this chapter, profiles of soot formation and evolution were also obtained in flames (along the axial direction) formed using blended fuel mixtures with different concentrations. In this

study CME is used as the blendstock for use in blending with various percentages of #2 diesel (volumetric). Prior to running the experiments, a fuel mixture was created and manually stirred for one minute followed by a few minutes of sonication process. A visual inspection of the fuel mixtures showed no separation of the fuels. It has been reported that no separation of the fuels (BD and No. 2 Diesel) is observed over a three-month period [218].

The blends consist of B80, B50, and B20. B20 has been reported to be an optimum, very popular, and an easy-storable blend; it also does not require any engine modification when being used in an IC diesel engine [104, 105]. Therefore, B20 was selected for the low biodiesel content blend. B50, which is a mixture of equal amounts of both fuels (biodiesel and diesel), and B80, which is the B20's counterpart in the high biodiesel content part, were selected in order to obtain the best comparison between different blending options. Figure 16-Figure 18 display the soot evolution in B80, B50, and B20 flames (CME/#2 diesel air flames). For the B80 flame a peak value of d_p of 27.5 nm at the flame height of 15 mm was observed (Figure 12). The average primary particle diameter for the B80 flame at the lowest sampled region of the flame (HAB of 6.5 mm) is 15.5 nm and for the highest sampled flame position (HAB of 27 mm) is 20.5 nm (Figure 12). For the B50 the primary particle diameter at 6.5 mm HAB (lowest sampled position) is measured to be 16 nm. At the highest sampled position in the flame (HAB of 28 mm) the average primary particle diameter of 19.5 nm was measured. The peak d_p value most likely takes place at the HAB of 15 mm.

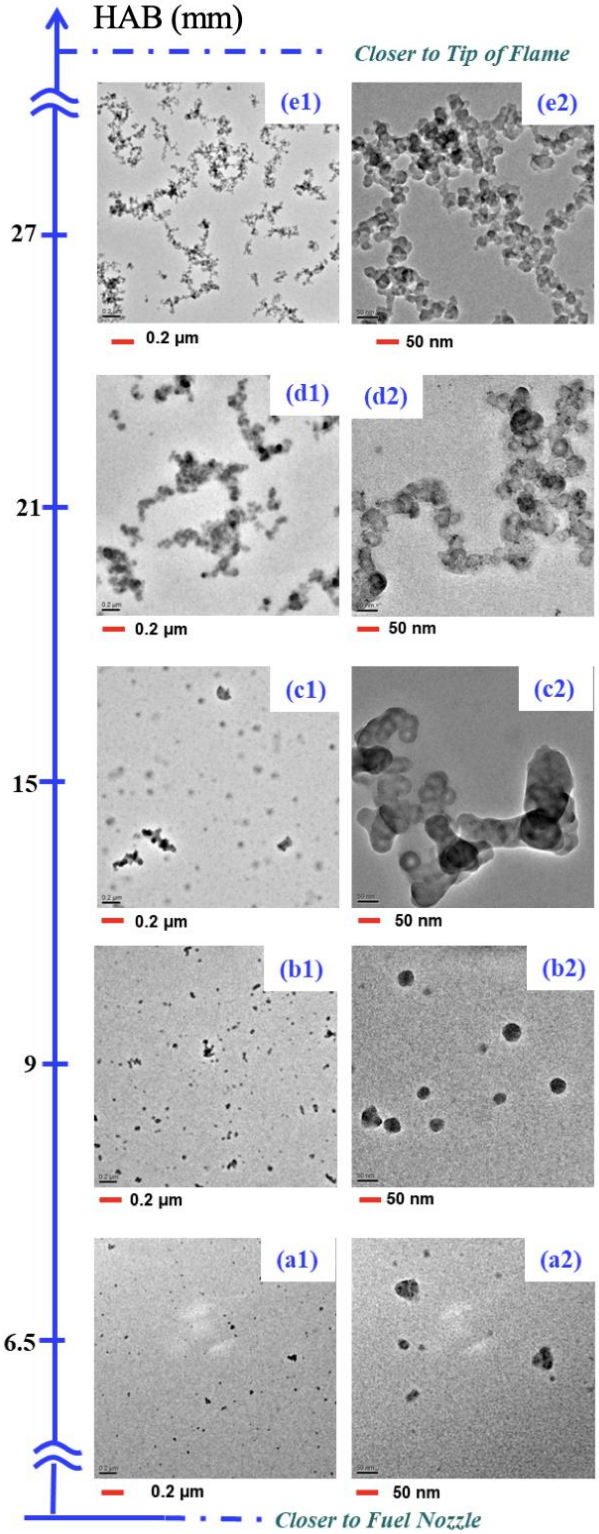

Figure 16. Representative progression of the soot evolution in an evaporated B80 air-flame through a series of low and higher-resolution TEM images taken from samples extracted along the central axis of the flame at various heights above the burner (HAB).

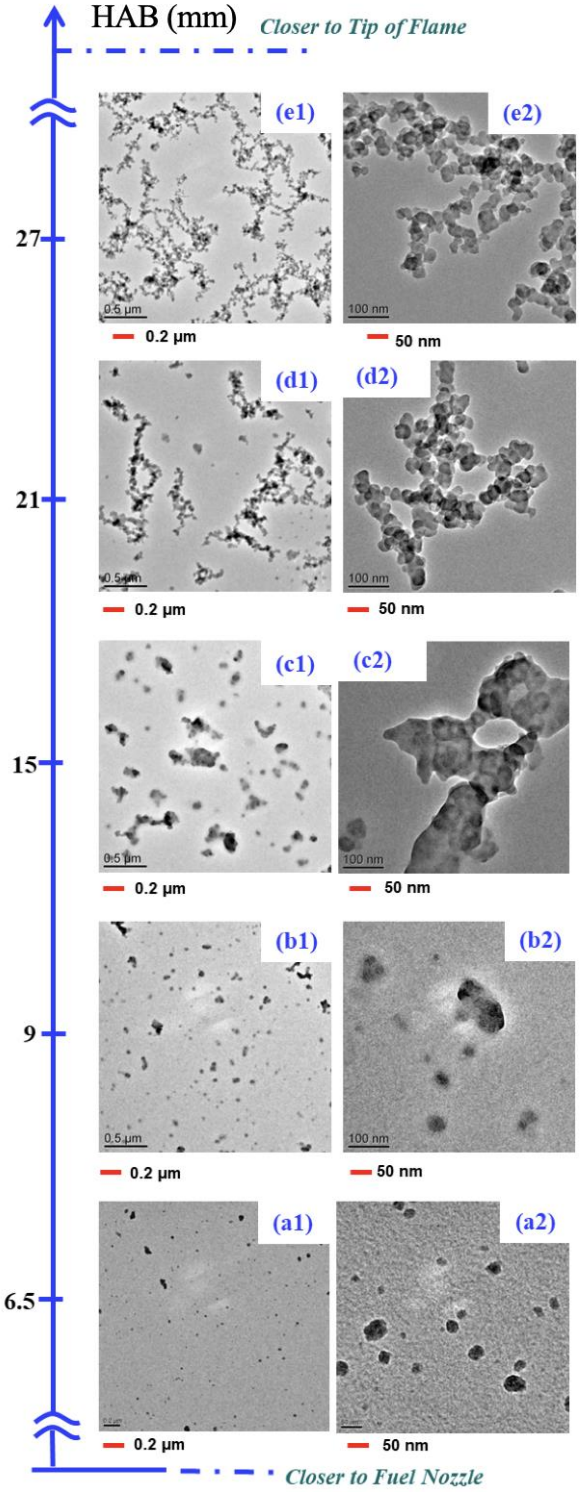

Figure 17. Representative progression of the soot evolution in an evaporated B50 air-flame through a series of low and higher-resolution TEM images taken from samples extracted along the central axis of the flame at various heights above the burner (HAB).

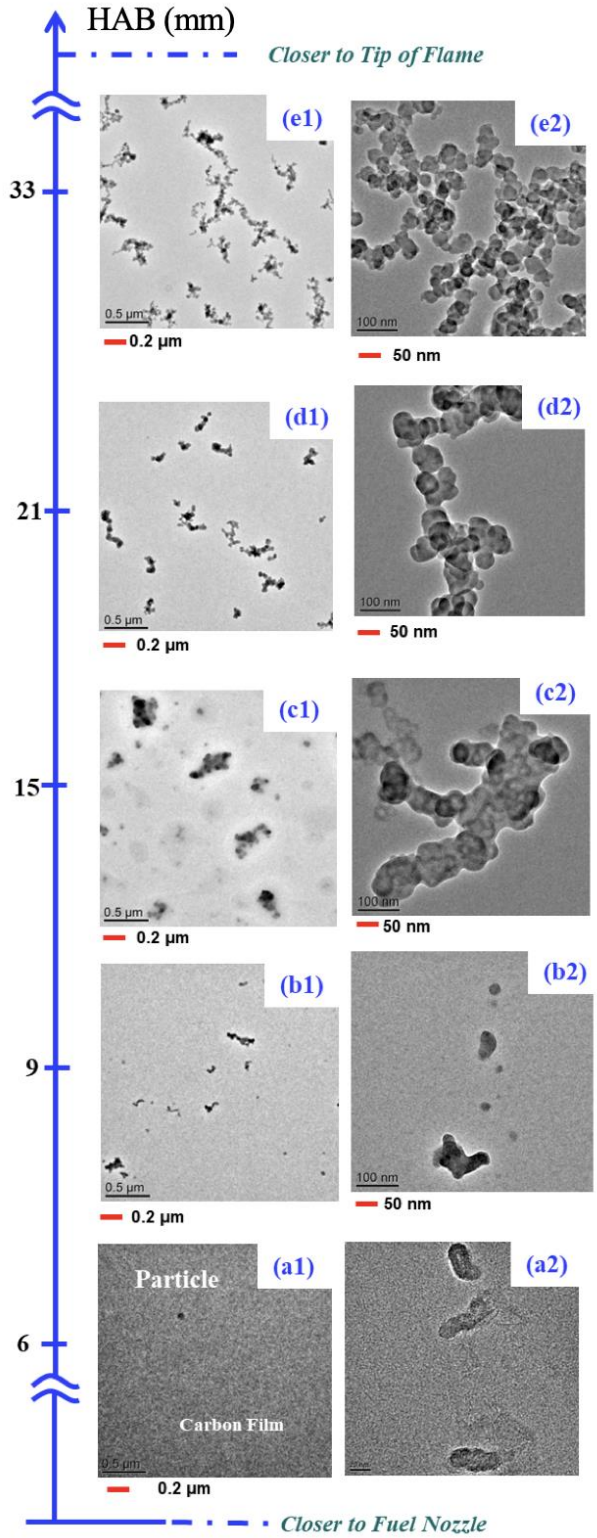

Figure 18. Representative progression of the soot evolution in an evaporated B20 air-flame through a series of low and higher-resolution TEM images taken from samples extracted along the central axis of the flame at various heights above the burner (HAB).

However, at this blending (B50) condition the soot agglomerates/aggregates at 15 mm HAB are composed of primary particles that have an undefined geometry making it difficult to identify their boundaries (Figure 17) and obtain an accurate d_p value. In the B20 flame (Figure 18) (blend with the lowest amount of biodiesel in the mixture) the value of d_p ranged from 21 nm at HAB of 9 mm to 18.5 nm at HAB of 33 mm (highest sampled position in flame). The peak d_p value for this flame was measured as 33.5 nm at HAB of 15 mm (Figure 12). The overall flame length is increased as the percentage of diesel is increased in the blended fuel mixture. The highest sampled position for the diesel is 33 mm HAB, while for the B80 and B50 it is the 27 mm HAB. These results show that the common growth mechanism for soot particle formation (particle inception, surface growth, and soot oxidation) present in the compressed volume of B100 CME is much stronger than in the taller diesel air flame. Therefore, soot precursors tend to form earlier in the short flames compared to the longer flames. Similar to the non-blended flames, the enhancement of nanostructure reorganization of the carbon layers forming the soot (mature) as they travel from a lower to a higher region of the flame can be observed.

A striking observation from soot evolution profiles is the shape and complexity of the aggregates in the upper region of the flames. That is, the morphology of the fully carbonized soot aggregates in the B80 (Figure 16 e1) and B50 (Figure 17 e1) resembles that of the B100 CME air flame (Figure 10 a4) and the fully carbonized soot aggregates in the pure diesel flame (Figure 9 e1) resemble those present in B20 (Figure 18 e1). One of the interesting trends observed in the soot evolutions inside the blended flames is the high density of the singlet particles or soot precursors in the B80 and B50 flame compared to those present in B20 at the lower regions of the flames.

Similar to the neat biodiesel soot profiles, the singlet particles or soot precursors formed in these blended fuel flames appear to be nearly spherical in shape. The soot profiles of the B80 and B50 already show the presence of a high density of soot precursor or young soot at 6.5 mm HAB. However, this is not the case for the B20 flame. This could be due to the fact that the flame "inner-cone" of the B80 and B50 (or "potential-core of the jet" if one considers a nonreacting laminar fuel jet issuing out of the nozzle) are shorter (Figure 16-Figure 18). It is evident that the density or number of the soot precursors in the diesel flame is smaller than those produced in the B80 and B50 flames; however, they are much larger in size. Soot precursors in the diesel flame are nonexistent at HAB of 6.0 and 9 mm. The fractal morphology (multi-branched) of the aggregates becomes more complex as the percentage of biodiesel is increased in the blending mixture. That is, a simple comparison of the soot evolution of the diesel flame (Figure 9) with the B20-B80 shows that the soot aggregates formed in the diesel flame are much more linear and shorter. Similar to the soot characteristics in the carbon particle evolution profiles of the neat biodiesel, the profiles from the blended flames have interesting characteristics. At a region of approximately half the flame (15 mm HAB) the presence of "irregular-shaped" fragments or "globules" formed of short complex agglomerates is evident (Figure 16-Figure 18).

The soot morphology (primary particle size and agglomeration) correlates well with the presented soot formation evolution profiles. The soot evolution profiles identifying a soot inception zone at the lower part of the flame, followed by the growth and agglomeration at the middle region, and oxidation zone at the upper part of the flame appear to correlate well with the trend variation of flame temperature. The flame

temperature profiles along the centerline for some of the evaporated biodiesel flames studied here have been reported in our previous work [175]. The higher the flame temperature, the higher the oxidation rate of the soot particles. It is evident from our soot evolution profiles that the physical characteristics (soot appearance and size) of soot samples collected along the axial direction in the flames formed using biodiesels are quite similar but very distinct from those present along a diesel flame. It has been suggested that flame temperature and/or the fuel type can affect soot formation. Some efforts have been devoted to understand the role of flame temperature and/or fuel type may have on soot formation. Gomez et al. investigated the effects of temperature and type of fuel on soot formation by monitoring the soot formation along the flame centerline of an axisymmetric laminar diffusion flame formed with four different types of fuels (butane, acetylene, butadiene, and benzene). It was suggested that the soot formation process along the flame centerline is highly temperature dependent regardless of fuel type or level of dilution [219]. The work of Love et al. on partially coflow premixed flames at a fixed equivalent ratio using several types of biodiesel and a diesel fuel suggest that the chemical structure of the fuel may be an important parameter in the formation of soot [220]. In that work despite the similarity of the flame temperature profiles along the centerline of the biodiesel and diesel flames the results of the soot volume fraction study suggest that the soot formation in the vaporized oxygenated fuel flames does not significantly vary between the different tested biodiesels. However, the results also show that the tested counterpart fuel (#2 diesel) is significantly sootier.

5 Morphological Characteristics of Soot Aggregates Using Image Processing Technique

Soot emission, as light absorbing carbon aerosols, has a great impact on the Earth's energy balance, climate, atmospheric chemistry, cloud processes, and global warming, which makes it one of the most important environmental concerns [221, 222]. Soot particles emitted from combustion configurations (engines, flames, etc.) are in the form of aggregates with different physical characteristics such as size, shape, complexity, and compactness. These aggregates are formed by primary particles which are typically considered spherical and uniform in size [223, 224]. In order to study the effects of soot or particulate matter (PM) on the environment and human health, different characteristics such as transport and optical properties, surface area, reactivity, and aerodynamic behavior need to be evaluated [221, 225-230]. These properties largely depend on soot morphology (size, shape, etc.) which is a crucial part of soot understanding [221, 225-230]. For instance, since soot reactivity is strongly affected by soot morphology, the design and functionality of soot after-treatment devices such as filters are influenced by soot morphology due to the fact that they rely on oxidation of trapped particles in order to prevent clogging and inefficiency [227, 231]. Another example would be the shape factor of emitted soot particles determining their suspension time in air before settling down, which also relates directly to the morphology [226]. Due to its importance, soot morphology has been the subject of numerous studies. One of the earliest studies on soot morphology was carried out by Medalia in 1967 [232] in which the morphology of carbon black aggregates were characterized by various properties such as bulkiness, shape factor, and anisomery. Several years later, Mandelbrot [233] introduced the fractal concept to

describe and quantify the morphology of complex objects. The Hausdorff or fractal dimension, D_f , describes how the volume of a fractal object (with self-similarity) varies with respect to its size [233]. That is, the increase in volume of a fractal object is directly related to the radius to the power of D_f. For a two-dimensional object, the D_f is between 1 and 2, and for the three-dimensional case, it is between 1 and 3 [234]. Fractal concept has been applied to various natural objects such as coastline and star clusters [235], marine particles [236], and combustion particles [234]. Fe, Zn, and SiO_2 aggregates were the first combustion products described by fractal geometry by Forrest and Witten in 1979 [237] with a D_f between 1.7 and 1.9. Samson et al. [238] first employed the fractal geometry to characterize soot particles emitted from acetylene flame, followed by numerous researchers who have performed fractal analysis on soot particles generated by flames and engines along with corresponding simulations. For instance, Köylü et al. [239] studied the soot morphology from laminar and turbulent flames of various fuels and reported the D_f values to be around 1.73 for soot aggregates in turbulent, and 1.78 in laminar flames. Zhang et al. [240] investigated the D_f of soot emitted from a light-duty diesel engine and reported D_f values of 1.7 to 1.9 which is consistent with several other studies conducted both on engines [229, 230, 241] and also constant-volume combustion chambers [242-244]. This range of D_f is known to be related to the diffusion limited cluster aggregation (DLCA) regime in which the diffusive motion of the clusters is the rate limiting step and also clusters and particles move and interact on random trajectories [234, 245, 246]. Similarly, Sorensen et al. [247] reported the simulated value of D_f for DLCA aggregates to be around 1.82, in consistent with the value of 1.74 for their experimental measurement.

5.1 Fractal dimension calculation

Image analysis on TEM micrographs of soot samples is performed by MATLAB and ImageJ to obtain the morphological properties (radios of gyration, D_f, skeleton length, branching ratio, etc). The first step is to convert each TEM image into a binary format, which possess only black and white pixels, in order to calculate the desired parameters. This process is completed by the ImageJ software and using the Otsu thresholding. The mathematical description of D_f can be shown as:

$$N = k_f \left(\frac{R_g}{d_p}\right)^{D_f} \qquad (1)$$

Where N is the number of primary particles per aggregate, k_f is the fractal prefactor, R_g is the radius of gyration, and d_p is the average diameter of primary particles of an aggregate.

There are various methods for obtaining the D_f of mathematical and physical objects [235, 248, 249]. Unlike mathematical objects (e.g., Sierpinski gasket), physical objects (e.g., particle aggregates) have poor self-similarity properties and also the TEM images have limited resolution [249, 250]. The most common method to avoid such problems is by analyzing a large number of aggregates instead of performing a separate analysis for each of them. That is, calculating N *and* R_g for each aggregate, then D_f and k_f would be the slope and intercept of the linear least-square regression line in the plot of $ln(N)$ over $ln(\frac{R_g}{d_p})$. To do so, the value of N can be obtained by:

$$N = \left(\frac{A_a}{A_p}\right)^a \qquad (2)$$

Where A_a is the projected area of an aggregate and A_p is the mean projected area of primary particles. A value of a=1.09 was applied in the present work which is commonly used in the literature [162, 168, 251] and suggested by Megaridis and Dobbins for soot aggregates formed inside a diffusion ethane flame [252]. The radius of gyration is defined as:

$$R_g^2 = \frac{1}{N}\sum r_i^2 \qquad (3)$$

Where r_i denotes the distance from the center of each primary particle to the centroid of the aggregate. Using two-dimensional projected views (TEM images) to calculate the D_f is not an ideal method since it can underestimate the real values of three-dimensional aggregates, but the error is not significant [253, 254]. The insignificant error is valid for R_g as well, and a two-dimensional approximation of the three-dimensional can be used to obtain the radius of gyration [162, 251] as follows:

$$R_g^2 = \frac{1}{m}\sum r_i^2 \qquad (4)$$

Where m is the number of pixels per aggregate, and r_i is the distance between each pixel and the centroid of the aggregate. However, without digital image processing tools, it is enormously demanding to calculate the R_g, therefore several alternatives and simplified methods within acceptable uncertainty range have been proposed for soot aggregates [238, 239]. Using the term $(LW)^{1/2}$ instead of R_g where L is the maximum projected length of the aggregate, and W is the maximum projected width normal to L, is a very well-known and widely-used alternative with an error range of about 5% compared to R_g [238, 239, 255-257].

Figure 19 illustrates a binarized soot aggregate (Figure 19 a) labeled with the aforementioned parameters, as well as the skeletonized version (Figure 19 b).

Skeletonization is an eroding process applied to a binary image and displays the skeleton of an object and decrease its thickness to one pixel. The one-pixel thick skeleton is presented by white color inside the black binary aggregate (Figure 19 b). Skeletonization of soot aggregates helps to demonstrate their structure without the influence of particle diameter and provide helpful statistical information which will be discussed in the next section.

Soot primary particles diameter is another important property and is measured manually not by means of related softwares to get the best accuracy. R_g is calculated by Eq. 4 from binary TEM images using MATLAB, and L, W, and A_a are calculated using ImageJ.

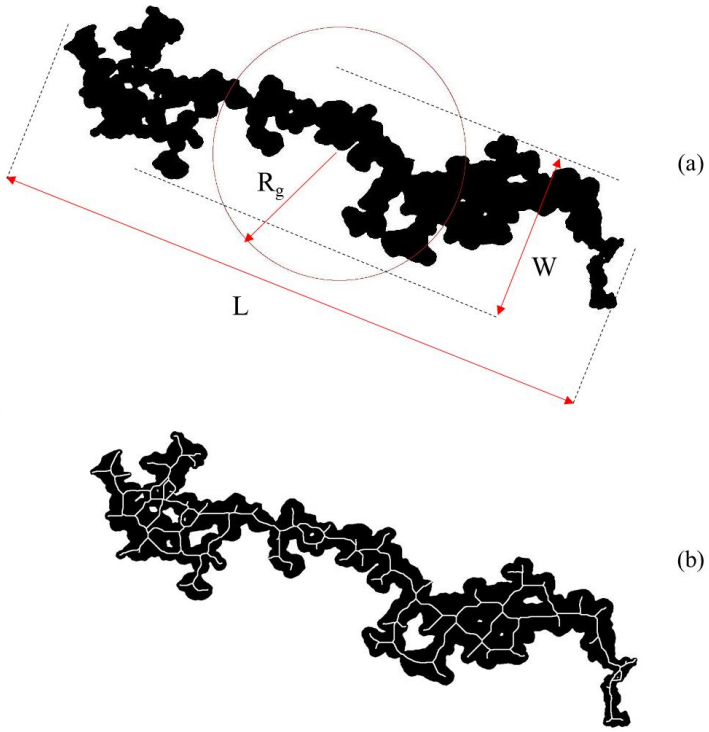

Figure 19. a) A binary soot aggregate labeled with R_g, L, and W along with b) the skeleton obtained by ImageJ.

5.2 Structural parameters for characterizing soot aggregates

Soot aggregates collected from biodiesel flames in this study are observed to have a distinct appearance compared to that of diesel with a higher rate of branching and agglomeration, which is also consistent with recent studies in the literature [258-261]. In order to quantify the branching ratio, we need to introduce a new parameter since it is not related directly to the D_f.

The goal is to count all the branching nodes for each aggregate. That is, counting all particles having more than two neighbor particles. That would be practically impossible through TEM or binary images due to the overlapping of soot primary particles. The solution is the employment of skeletonized images of soot aggregates since their skeleton has a thickness of one pixel and therefore makes it possible to identify the branching nodes. This method may not lead to the exact number of branching nodes due to the erosion process, however it is easily applicable and allows to statistically evaluate the branching. ImageJ has been employed to count the branching nodes. It provides the number of junctions (NJ) when processing a skeletonized object. Technically, ImageJ considers a black pixel (here black pixels are the objects and white pixels are the background) a junction when is has more than two neighbor black pixels.

Besides the branching, the length of aggregates and also the length of branches can provide information on the soot growth process. The parameter "L" (Figure 19 a) cannot provide reliable information on the length of aggregates, especially when aggregates are highly branched and curved. An alternative could be the length of the "largest shortest branch" in ImageJ when analyzing the skeletonized aggregates, which is referred to as the skeleton length (SL) [262]. Figure 20 illustrates a skeletonized aggregate

(Figure 20 a) along with its largest shortest branch being distinguished as bold (Figure 20 b). It is clear from Figure 20 b that the SL provide a more accurate estimation of the length of aggregate than L even in this rather straight aggregate. The length summation of all branches in one aggregate minus the SL (bold path in Figure 20 b) will be reported by the branching length (BL) as a representative of the branching growth.

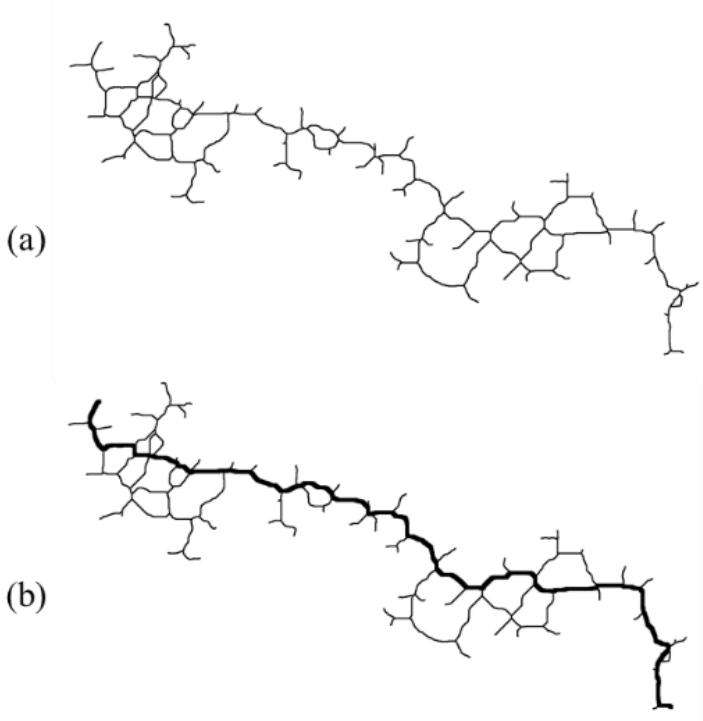

Figure 20. a) TEM skeletonized image of an aggregate, b) TEM skeletonized image of an aggregate with bold skeleton branch.

5.3 Obtained D_f and structural values

As mentioned in section 5.1, two common approaches for calculating D_f are used in the present work. The first approach obtains D_f by calculating N from Eq. 2 and R_g from Eq. 4, then plotting $ln(N)$ over $ln\left(\frac{R_g}{d_p}\right)$ for all aggregate, then finding the slope of the linear least-square regression. The second approach is very similar to the first one, but the term $(LW)^{1/2}$ was replaced the R_g in the calculation [238, 239]. Table 3 and Table 4

provide the values of fractal dimensions (D_f) for soot aggregates sampled from the tip of the studied flames where they are known to be fully carbonized and represent the final stage of soot evolution (mature soot). Additionally, R-square (R^2), which is an indication of how close the data are to the regression line, is reported. Higher values of R^2 indicate that the data are closer to the fitted regression line, with the maximum possible value of one.

Table 3. Flame height, D_f and R^2 for different fuels at the tip of the flames using R_g.

Fuel	Flame height (mm)	D_f	R^2
Diesel	33	1.56 ± 0.224	0.90
B20	33	1.31 ± 0.305	0.67
B50	27	1.69 ± 0.268	0.90
B80	27	1.72 ± 0.188	0.92
CME	21	1.51 ± 0.204	0.89
COME	21	1.5 ± 0.191	0.87
SME	25	1.72 ± 0.190	0.89

Table 4. Flame height, D_f, and R^2 for different fuels at the tip of the flames using $(LW)^{1/2}$.

Fuel	Flame height (mm)	D_f	R^2
Diesel	33	1.9 ± 0.088	0.99
B20	33	1.65 ± 0.317	0.75
B50	27	1.79 ± 0.158	0.97
B80	27	1.83 ± 0.087	0.98
CME	21	1.8 ± 0.077	0.99
COME	21	1.79 ± 0.082	0.98
SME	25	1.86 ± 0.083	0.98

D_f values obtained using R_g (Table 3) range from 1.31 ± 0.305 (B20) to 1.72 ± 0.188 and 1.72 ± 0.190 (B80 and SME). On the other hand, $(LW)^{1/2}$ (Table 4) leads to larger D_f values ranging from 1.65 ± 0.317 (B20) to 1.9 ± 0.088 (diesel). All the D_f values are calculated with 95% confidence. The higher values of D_f by means of $(LW)^{1/2}$ than R_g is well-known and has been reported in the literature [238, 239]. It is also reported that their difference would be approximately 5% [238, 239]. The differences between their values obtained in this study are approximately 5% to 8% in case of three flames (B50, B80, and SME) and 20% in the other four flames (diesel, B20, CME, and COME).

Both approaches ($(LW)^{1/2}$ and R_g) lead to a very similar trend. That is, D_f decreases from diesel to B20 followed by an increase from B20 to B80 (with B50 in the middle), then decreases again toward CME and COME (similar values) and increases to SME. Despite their similarities in the trendline, D_f values from $(LW)^{1/2}$ are considered more precise in this study and are selected as the main data set for the interpretation. The first reason behind our selection was the range of D_f values. Soot aggregates presenting in the upper part of a coflow flame are known to follow the DLCA aggregation regime which results to D_f values in the range of 1.7-1.9. This criterion is met only when using $(LW)^{1/2}$. Another reason was the D_f values for diesel in relation to the biodiesel. B50, B80, and SME have higher D_f than diesel based on R_g while diesel has the highest D_f than all other tested fuels based on $(LW)^{1/2}$ which is more consistent with the literature [260, 263].

One interesting observation is the R^2 parameter which is significantly high based on $(LW)^{1/2}$ (Table 4). Except B20, all other fuels resulted in a R^2 value fairly close to one (the maximum value) implying that the data are highly close to the regression line. Figure 21 shows the plotted data of $ln(N)$ over $ln(\frac{R_g}{d_p})$ and the regression line for COME as an

example to show the difference. It is evident that all the data from $(LW)^{1/2}$ are profoundly close to the regression line as indicated by the R^2 value (Figure 21 b), but more spread when R_g is used (Figure 21 a).

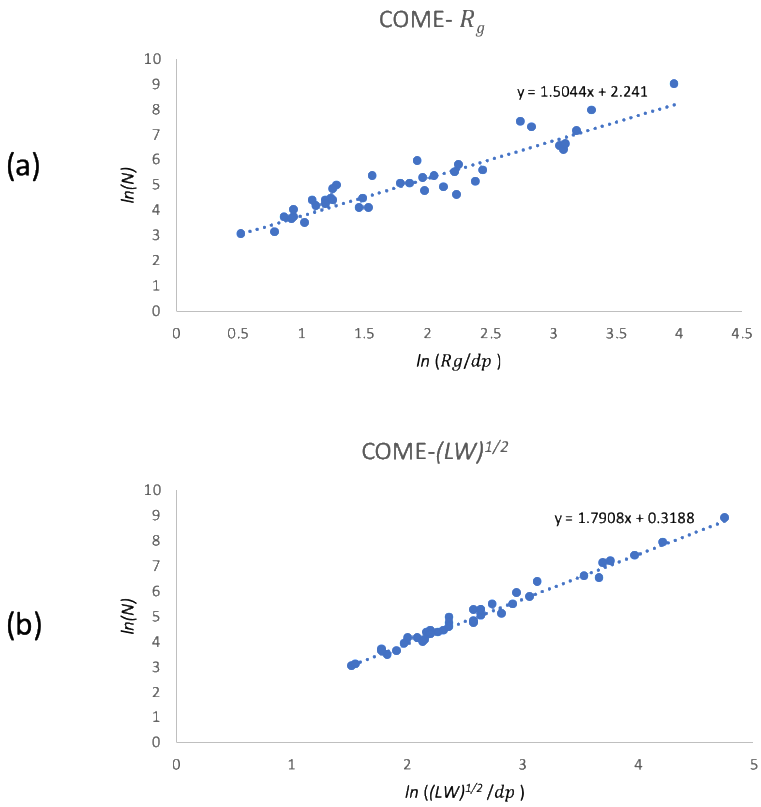

Figure 21. Plotted data for aggregates extracted from COME flame tip by using a) Rg, and b) $(LW)^{1/2}$.

While D_f values indicate the compactness of soot aggregates, NJ, SL, and BL also need to be reported to characterize their branching and growth rate. Due to the highly dispersed distribution of NJ, SL, and BL values, their mean values are not reported since they may not show any reliable trend. However, the most complex aggregates with the highest NJ, SL, and BL from each flame may lead to a better comparison. The NJ, SL, and BL values of these selected and representative aggregates are provided in Table 5. Diesel produced the most linear aggregate with the lowest NJ of 76 and by adding

biodiesel to that, NJ increased from 110 for B20 to 608 for B80. COME led to the most branched aggregate while CME and SME led to moderately branched ones. Three highest branched aggregates (B50, B80 and COME) also have the highest SL and BL. While B20 aggregate has slightly more branching nodes than that of diesel, it has a lower SL and BL.

Table 5. Highest number of junctions for aggregates from tip of the studied flames and summation of all branches of selected aggregate.

Fuel	Flame height (mm)	NJ (selected aggregate)	SL (μm) (selected aggregate)	BL (μm) (selected aggregate)
Diesel	33	76	2.5	5.4
B20	33	110	1.5	4.8
B50	27	554	5.5	30
B80	27	608	4.5	31.7
CME	21	255	4.1	15.2
COME	21	646	5.4	32.7
SME	25	225	2.7	11

(NJ: Number of Junctions, SL: Skeleton Length, BL: Branching Length)

5.4 Detailed soot morphology comparison from diesel and blending

In order to interpret the results it is worth noting that there are two main parameters affecting the D_f of soot fractal aggregates formed inside a flame: i) soot inception rate (equivalent to the precursors density) and ii) the residence time of fractal clusters inside the flame volume [251]. Both parameters have a direct relation to the compactness of aggregates and consequently D_f. That is, a higher number of non-fractal primary particles at the lower part of the flame (stronger soot inception) and/or longer residence time tend to increase the chance of particle collision and agglomeration, hence increasing the compactness and D_f. TEM images collected from the lower part of the

flame can be used to evaluate the density of soot singlet particles operating as the primary particles to form fractals at the upper part of the flame. Since the sampling of these fractals occurs at the flame tip region, the flame height could be a meaningful representative of the residence time due to the identical flow rate used to form all the tested flames. Therefore, singlet particle density and the flame height are the two main parameters to interpret the results of this study. Additionally, agglomeration schemes and carbonization process will be discussed to explain the distinct fractal properties observed in tested flames.

Considering blended fuels, D_f increases with increasing the percentage of biodiesel in the mixture (Table 3) implying that soot aggregates become more compact and less stretched/linear by the addition of biodiesel to the blend. B20 has the longest flame (33mm) among the tested blends while B50 and B80 form shorter flames with the height of 27 mm. Therefore, soot particles at the tip of the B20 flame experience the longest residence time compared to the other two blends which tends to increase the D_f. However, despite having the longest flame, B20 leads to a lower D_f than B50 and B80 suggesting a significantly lower singlet particles density at the lower part of the flame. Soot samples inside the B50 and B80 experience similar residence time (approximately the same flame height), therefore fewer number of singlet particles (weaker soot inception) may be the reason behind the lower D_f values in the case of B50 than B80. Diesel and B20 form flames with similar heights, thus lower D_f values for B20 means weaker soot inception for B20. These conclusions for the variation of soot inception need to be verified by TEM images from lower part of the flames which illustrate the singlet particles.

Figure 22 presents a set of low resolution TEM images (Figure 22 a1-a4) with softened background (Figure 22 b1-b4) and magnified center regions (Figure 22 c1-c4) from the lower part of the diesel, B20, B50, and B80 flames, respectively, to evaluate the inception rate or the density of non-fractal spherical particles. The singlet particles or monomers observed at this region travel on ballistic (linear) trajectories and form compact clusters upon contact. As the size of the growing clusters increases, their movement is then characterized by Brownian (random) walks forming relatively loos and ramified clusters near the flame tip. The higher number of monomers at the beginning of the aggregation process increases the compactness of final clusters by increasing the collision probability [264-266]. Based on the D_f values, we concluded the order of soot inception to be B20<B50<B80 and B20<diesel. Figure 22 can support this conclusion. It is evident from Figure 22 that B20 (Figure 22 a2,b2) leads to a significantly lower density of non-fractal and singlet particles than B50 (Figure 22 a3,b3) and B80 (Figure 22 a4,b4). Additionally, the singlet particle density is lower in the case of B50 (Figure 22 a3,b3) than B80 (Figure 22 a4,b4) which is likewise consistent with the conclusion based on D_f values. A weaker soot inception for B20 than diesel is verified by Figure 22 (a1-a3 vs. b1-b3). Last but not least, Figure 22 clearly shows higher singlet particle density (enhancing D_f) for B50 and B80 compared to diesel, however a higher D_f value for diesel suggests that the higher flame length of diesel outweighed the higher soot inception rate of B50 and B80. Another interesting observation is the size of singlet non-fractal particles. Figure 22 clearly shows the largest particles for diesel and the smallest ones for B20. More addition of biodiesel to the mixture (B50 and B80) increased the particle size but still considerably smaller than diesel.

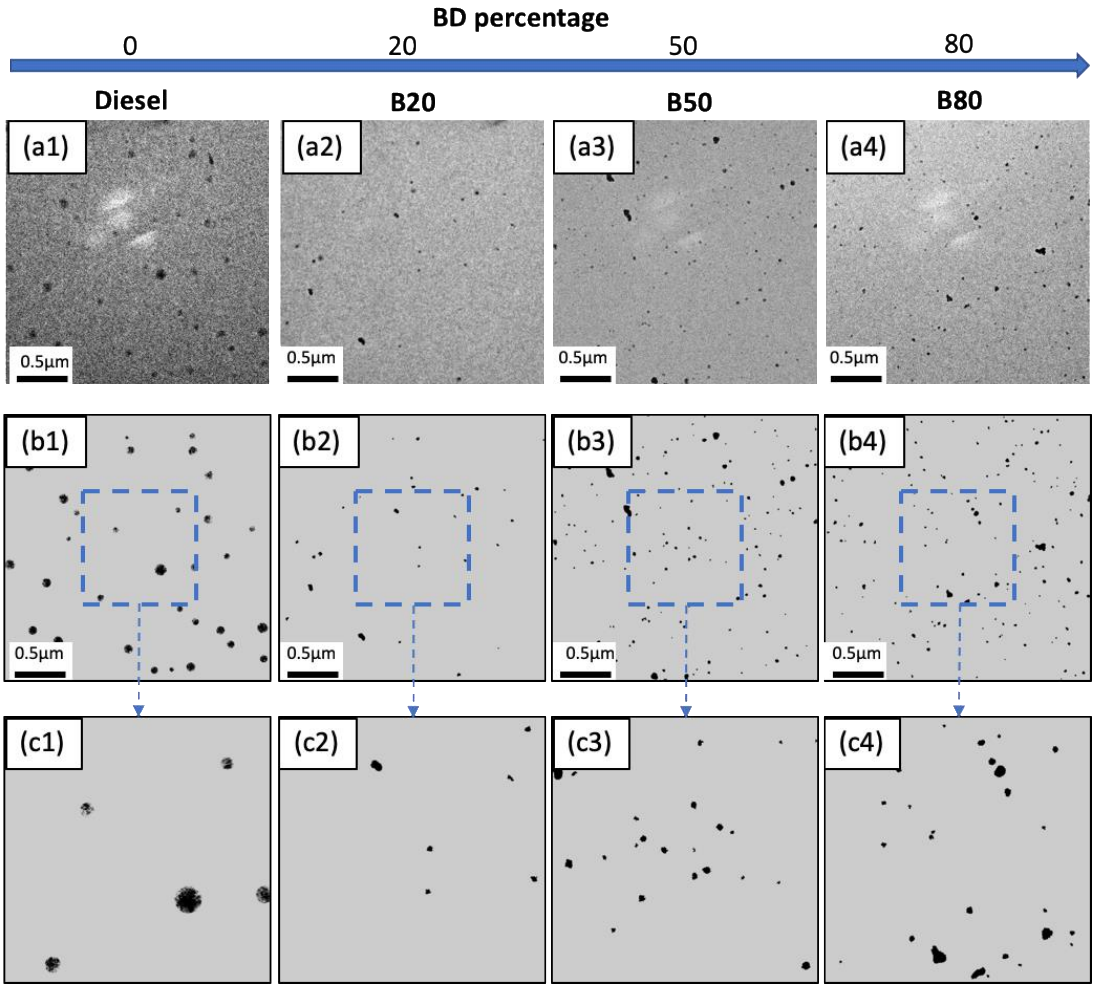

Figure 22. Low resolution TEM images of non-fractal soot precursors captured at the lower part of the diesel, B20, B50, and B80 flames (a1-a4, respectively). TEM images with smoothened background (b1-b4) and their magnified center regions (c1-c4) are presented to remove the noise and improve the visual clarity. The singlet non-fractal particles are the primary particles colliding with each other under different aggregation schemes to form the fractals in the upper region of the flame.

Figure 23 provides TEM images (Figure 23 a1-a4) of soot fractals collected from the flame tip region of diesel, B20, B50, and B80 along with the binary images (b1-b4) of selected aggregates with the highest NJ and SL. Skeletonized images (Figure 23 c1-c4) of the selected aggregates are provided for a better observation of their structure, branching, and complexity. TEM images in Figure 22 and Figure 23 illustrate that a high number of soot precursors at the lower part of the flame (stronger soot inception) leads to

highly branched and agglomerated clusters at the flame upper region. TEM images from B50 (Figure 23 a3,b3) and B80 (Figure 23 a4,b4) present highly elongated and branched fractal aggregates with high values of NJ and SL for the representative aggregates as a result of the high singlet particle density at the lower part of the flame. While B50 and B80 produced fractal aggregates with significantly high length and branching with respect to diesel, B20 led to higher similarity to diesel. However, the decreasing effect of B20 on soot formation compared to diesel is clearly observed from Fig.4 and 5. The effect of biodiesel addition to the diesel is evident from a visual inspection of TEM images (Figure 23 a1-a4) even without considering the statistics obtained from image analysis. B80 resulted in a fully occupied TEM image while one can notice much empty space as the biodiesel percentage in the mixture decreases. This observation does not mean higher soot emission for blended fuels since most of the fractals are fully oxidized before leaving the flame medium due to the higher oxidation rate and smaller primary particles. On the other hand, higher number of fractals leave the diesel flame ought to the lower oxidation rate and larger primary particles making diesel flame the highest soot-emitting tested flame. This is highly expected since biodiesel and blended fuels are already known to reduce the soot and other harmful emissions [28, 267]. The wide size distribution of aggregates is obvious by observing the TEM images (Figure 23 a1-a4) which contain several small aggregates with less than 100 nm in length in contrast to extended aggregates longer than 2 µm.

Physical properties (e.g., density, viscosity), fuel molecular structure (e.g., carbon chain length, number of double bonds, the degree of unsaturation), and oxygen content

can play key roles in soot formation and growth path [268-272] leading to the considerable difference between soot morphological characteristics from diesel, B20, B50 and B80. The obtained morphological characteristics of fractal aggregates generated by blended fuels can increase the efficiency of after-treatment devices such as particulate filters. All tested blends generated more open-structured aggregates than diesel which increases the particulate filtering efficiency [226, 263, 273]. Moreover, larger aggregates from B50 and B80 can be trapped easier by filters which is another desired characteristic [274]. Last but not least, all biodiesels and blended fuels led to smaller primary particles forming the fractal aggregates compared to diesel. This is consistent with previous studies reporting smaller primary particles generated by biodiesel and blending compared to diesel [63, 227, 261, 275-278]. The smaller primary particles enhance the oxidation of trapped particles inside the filters and hence improves the filtering efficiency and reusability [279, 280].

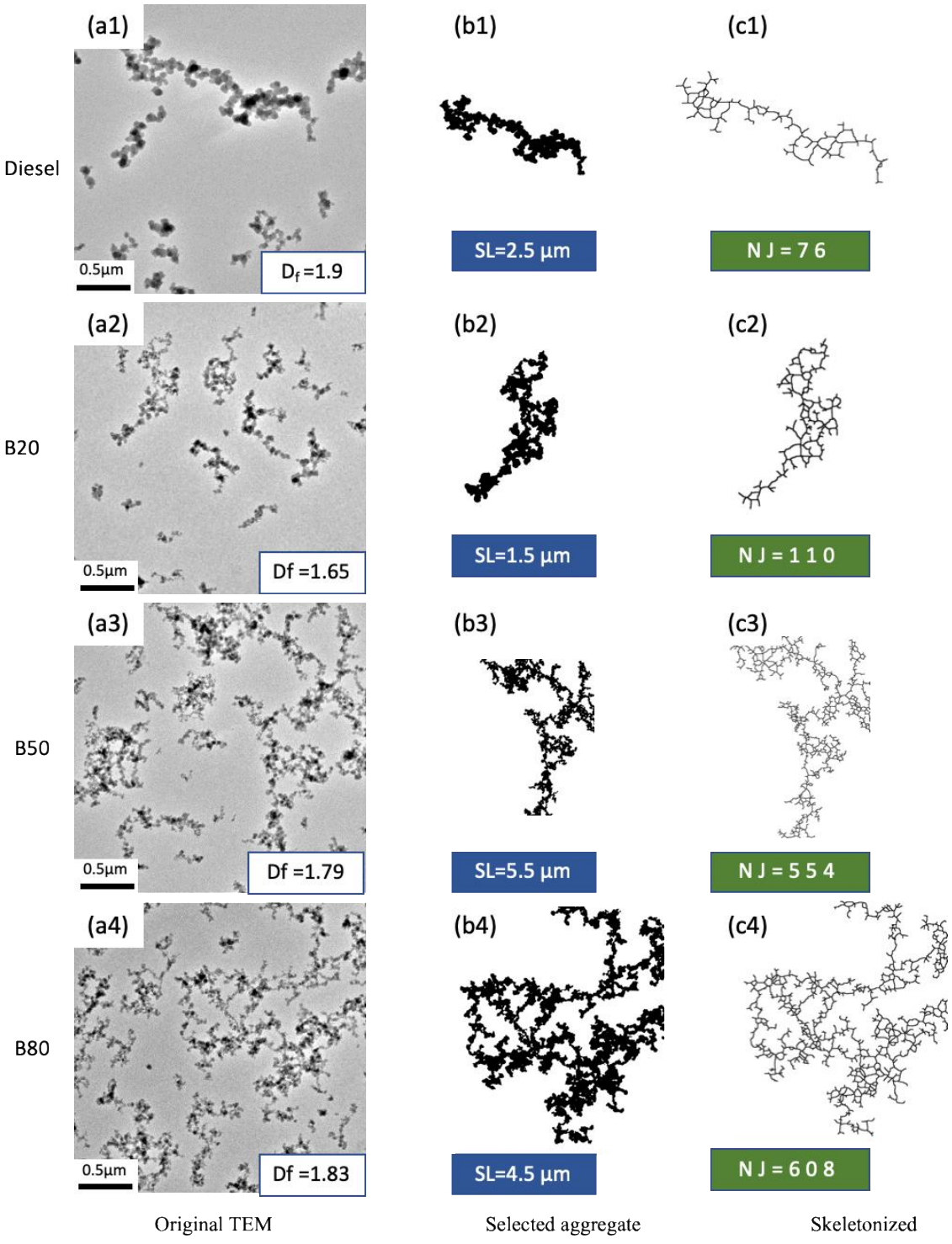

Figure 23. (a1 to a4) represent TEM images showing typical soot fractal aggregates extracted from the tip region of diesel, B20, B50, and B80 air flames, respectively. The corresponding binary images of a single aggregate with the highest SL and NJ for each flame (b1-b4) are presented to compare the effects of blending on soot microstructure. The skeletonized images of these aggregates are also presented (c1-c4) to observe their branching.

5.5 Detailed soot morphology comparison from diesel and biodiesel

All three tested biodiesels formed shorter flames containing soot fractal aggregates with lower D_f values compared to diesel. Figure 24 represents TEM images (Figure 24 a1-a4) with softened background (Figure 24 b1-b4) of soot non-fractal singlet particles from the lower part of the diesel, CME, COME, and SME flames. It clearly displays larger but fewer non-fractal spherical particles (which tends to decrease the D_f) for diesel compared to biodiesel. On the other hand, diesel forms the longest flame among all tested fuels, which increases the D_f. The higher D_f value for diesel suggests that its longer flame outweighs its lower inception rate. It can be concluded that the residence time of soot aggregates inside the flame before the extraction has a significant impact on their aggregation process.

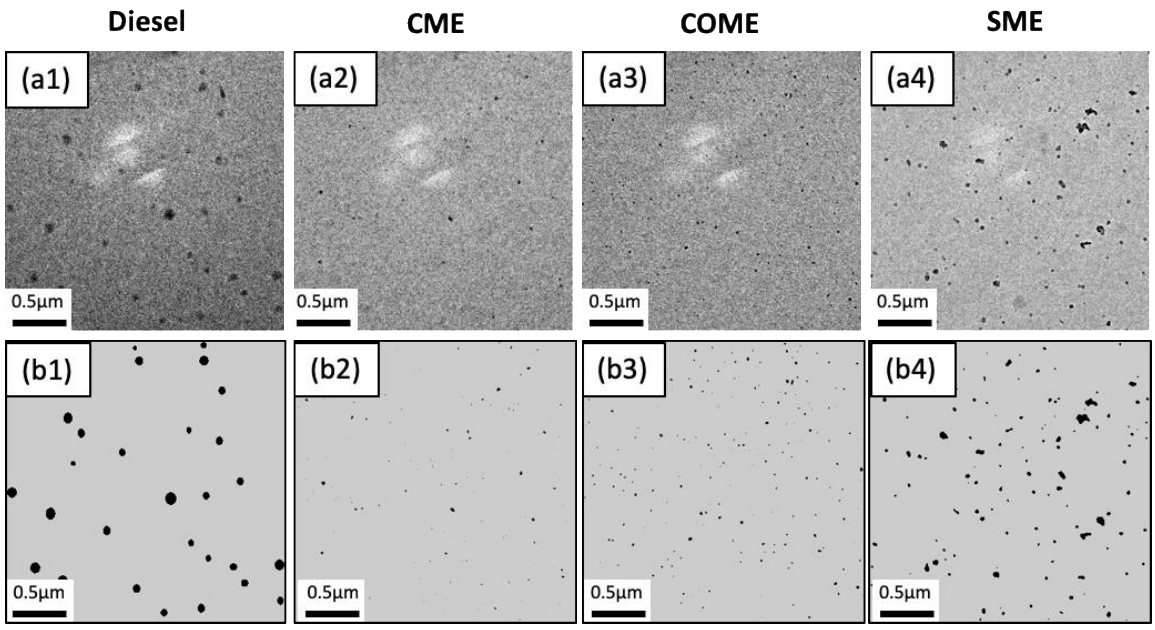

Figure 24. Low resolution TEM images of soot precursors captured at the lower part of the diesel, CME, COME, and SME flames (a1-a4, respectively) in order to observe the effect of different types of biodiesel fuels on soot inception rate. The TEM images with smoothened background (b1-b4) are presented to improve the visual clarity.

Figure 25, which illustrates TEM, binary, and skeletonized images of selected soot aggregates at the tip of the diesel and biodiesel flames, demonstrates the determining role of inception rate on the morphology of fractal aggregates. Highly agglomerated fractal clusters present in CME, COME, and SME flames are the outcome of extremely high inception rates while diesel fractals are the opposite with the lowest degree of agglomeration due to the weakest inception rate.

All tested biodiesels lead to longer aggregates (higher SL) with higher branching (higher NJ) compared to diesel. Only 76 junctions were counted for the selected diesel aggregate compared to 225 for SME, 255 for CME, and 646 for COME. Similar to Figure 23, a wide size distribution of aggregates is evident from Figure 25 a1-a4 illustrating quite small aggregates coexist with very long-stretched ones.

All biodiesels formed more open-structured and larger soot aggregates with smaller primary particles. The open-structured and large aggregates are very desirable in filtering technology and enhance the efficiency of particulate filters [263, 274, 280]. The difference in soot morphology is noticeable even among various biodiesel fuels denoting the strong influence of fuel chemistry on soot formation. Similar to the blending, pure biodiesels led to highly occupied TEM images (Figure 25 a2-a4) with respect to that of diesel (Figure 25 a1). However, the stronger oxidation and smaller primary particles in biodiesel flames result in a lower soot emission in comparison to diesel.

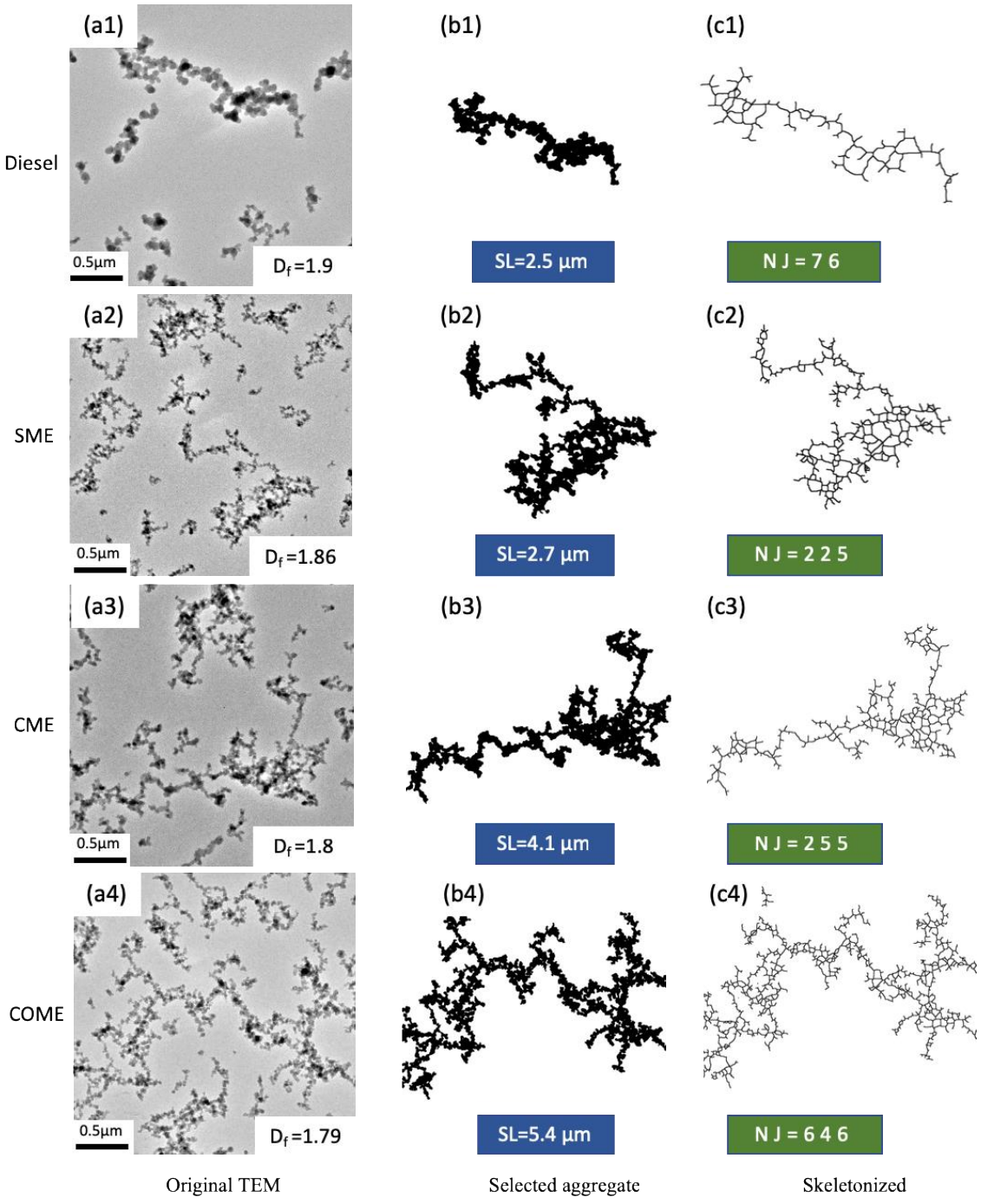

Figure 25. (a1-a4) TEM images showing typical morphology of soot samples extracted near the tip of the diesel, SME, CME, and COME air flames, respectively. The corresponding binary images of a fractal aggregate with the highest SL and NJ for each flame (b1-b4) are presented to compare the effects of biodiesel on soot microstructure. The skeletonized images of these aggregates are also presented (c1-c4) to observe their branching structure.

5.6 Aggregation growth and evolution

In our study, neat biodiesel fuels and the biodiesel/diesel blending with high biodiesel percentage (50% and 80%) generated a number of highly long-stretched soot fractal aggregates (showed as selected aggregates in Figure 24 and Figure 25) compared to commonly reported soot aggregates from various combustion configurations and fuels which are known to be up to a few hundred nm [64, 168, 227, 242, 281-284]. Most of these unusual and highly extended irregular aggregates here are longer than 4μm and are not entirely captured in the TEM images even in the low magnification of 4,000X. Similar-sized aggregates have been also reported by Aizawa et al. [260] and were found only inside the biodiesel spray flame and not inside the diesel flame. The aggregation mechanism was believed to be responsible for such a different morphology. Based on our TEM images and calculated fractal and structural parameters, we hypothesize that the combination of aggregation and carbonization mechanism can provide a credible explanation to the considerable difference between diesel- and biodiesel-derived soot.

Figure 26 illustrates our proposed aggregation evolution including two observed fractal evolution paths inside the coflow flame. TEM images from diesel and COME are presented as two examples in order to support the mechanism. Similar to any coflow diffusion flame, the monomer-cluster aggregation (MCA) is the governing aggregation scheme in the lower part of our tested flames because of the plenty of monomers at this region while their upper region is dominated by cluster-cluster aggregation (CCA) due to the presence of higher number of large clusters and consumption of monomers [252, 264]. In MCA, monomer movement is characterized by ballistic (linear) trajectories in the lower part of the flame due to a large mean free path compared to the size of primary

particles and growing clusters [252, 265]. As clusters grow and enter the upper region of the flame, their size passes the mean free path leading to the Brownian (random) motion [252, 266]. Particles traveling on linear trajectories are more likely to deeply penetrate into the clusters compared to the random motion, therefore MCA results in more compact clusters with higher D_f compared to CCA [264].

The outcome of MCA is apparent in the low region of the COME flame resulting in compact non-fractal tarry-like or droplet-like clusters due to the high amount of hydrogen, soluble organic fraction (SOF), and volatile organic fraction (VOF) in the presence of relatively low temperature [63, 64, 285]. The schematic of these structures is shown by Figure 26 b. These non-fractal objects with nuclei inside can easily be detected in the TEM images as pointed by arrows in Figure 26 b1 and enlarged in Figure 26 b2. The conversion of non-fractal structures to fractals is observed when entering the upper region of the COME flame (Figure 26 b, c). This transition is due to the carbonization in which soot particles become fully defined and solidified. The transition from non-fractals to fractals witnessed in COME flame follows the carbonization process suggested by Reilly et al. [207] in which large PAH-containing droplets including nuclei grow and fuse together followed by their conversion to well-defined fractals due to the carbonization when exposed to the higher temperature at the upper part of the flame. One intermediate fractal aggregate as a result of this carbonization process is depicted by Figure 26 c1 with its skeleton shown by Figure 26 c2. The intermediate aggregates grow and collide with each other under the CCA to form long-stretched and branched fractal aggregates near the tip of the flame (Figure 26 d). The TEM image from the tip region of COME flame (Figure 26 d1) illustrates the presence of highly stretched and open-structured aggregates.

The aggregates are carefully inspected to make sure there is no discontinuity along their length. Several points of interest are pointed by arrows and enlarged to show that the selected aggregate is one complete aggregate without any break or gap.

In contrast to COME, aggregation evolution in diesel flame seems to follow another path (path 2 in Figure 26). The large non-fractal droplet-like structures observed in COME flame are not dominant in diesel flame. TEM images from low region of the diesel flame (Figure 26 e1-2, f1) demonstrate the dominance of singlet particles and small clusters instead of large droplet-like structures. The number of nuclei inside the clusters is limited (Figure 26 e) compared to COME indicating that small number of particles are fusing together. Figure 26 e1-2 show several transparent non-fractal structures containing mostly one or two nuclei which are pointed by arrows and schematically presented by Figure 26 e. These transparent particles become more defined and solidified as shown by Figure 26 f1, as a result of carbonization. The carbonization evolution taking place in the diesel flame follows the mechanism suggested by Lahaye [213] in which particles first carbonize and then go through the agglomeration to form fractal structures. Due to the abundance of singlet particles and small clusters at this point, the aggregation is governed by MCA leading to relatively compact intermediate fractals. Figure 26 g1 shows an intermediate fractal with the skeleton structure (Figure 26 g2) from the diesel flame which is more compact than the one presenting in COME flame (Figure 26 c1). The intermediate aggregates then follow the CCA to form the final fractal aggregates in the tip region of the diesel flame (Figure 26 h). The TEM images from the tip region of diesel flame (Figure 26 h1) clearly depicts more compact, shorter, less ramified and stretched fractals

with respect to COME (Figure 26 d1). The fractal parameters obtained in this study (i.e., lower D_f, higher NJ and SL for COME) also support the observation of TEM images.

The main difference between path 1 and 2 is the order in which MCA and carbonization take place. Late carbonization (path 1) allows the formation of large non-fractal droplet-like structures as a result of MCA leading to more open fractals after carbonization. Nevertheless, an early carbonization (path 2) solidifies the liquid-like non-fractals first and forms singlet particles and small clusters leading to more compact fractals as a result of following MCA.

TEM images of soot aggregates sampled from the tested flames along with their calculated D_f values suggest that path 1 is dominant inside the COME, CME, SME, B50, and B80 flames while path 2 is governing inside the diesel and B20 flames. It was expected that the characteristics of B20 derived soot follow that of diesel due to the high percentage of diesel in the mixture and similarly B80 was expected to follow that of biodiesel. The B50 which contains equal percentage of diesel and biodiesel resembled biodiesel more than diesel suggesting the strong effect of biodiesel on soot properties.

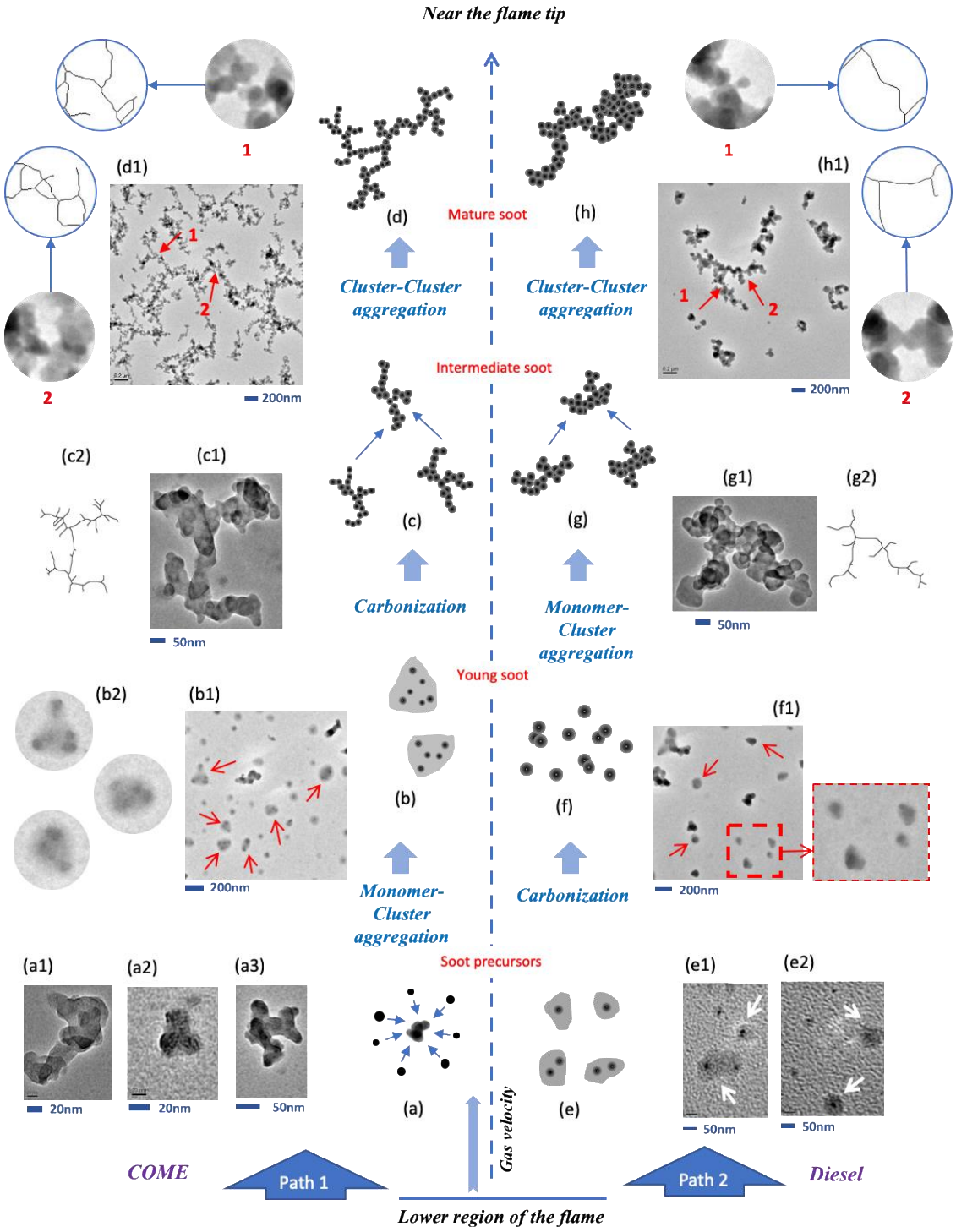

Figure 26. Soot aggregation evolution and growth along the flame axis of vaporized biodiesel (path 1, COME) and vaporized US#2 diesel (path 2). In the case of path 1, carbonization happens after the MCA leading to large droplet-like structures resulting in open-structured and stretched fractal aggregates in the tip region of COME flame. Unlike path 1, carbonization takes place early and before the dominance of the MCA in path 2 favoring the creation of singlet particles instead of the large droplet-like structures which results in more compact and less stretched and extended fractals in the tip region of the diesel flame.

6 Nanostructure Analysis of Soot Particles Derived from Studied Flames

Soot nanostructure can have implications in the design of combustion systems and their emission requirements. For instance, the type of nanostructure (crystalline vs amorphous), quality of the graphene layers in the crystalline soot (length and curvature), can alter its properties such as its thermal radiation (emissivity of soot) and oxidative reactivity [286, 287]. The nanostructure can also provide information on the type of fuel used for the combustion processes that lead to its generation [222, 287-290]. Nanostructure studies on soot can also help reveal its maturity. Soot nanostructure can also affect biological reactivity and hence affecting human health and the environment [221, 258, 291].

6.1 Visual inspection of soot nanostructure

Figure 27 (a1-a4), (b1-b4) and (c1-c4) are representative HR-TEM images of the soot nanostructure at the different stages of the soot evolution for CME, COME, and SME, respectively, all using air as the oxidizer. Brightness and contrast were adjusted to improve the visibility of the fringes in the HR-TEM images. HR-TEM imaging analysis on the precursor particles or "young soot" show that their internal structure is not well ordered (Figure 27 (a1, b1, c1)). These soot precursors captured from the lower region of the flame are composed of an amorphous tar-like polymeric material with no clear boundaries between the particle surface and the carbon film of the TEM grid. It is evident from an inspection of the HR-TEM images (Figure 27) that as the particles are transported

in the direction of the flame's tip (direction of temperature increase) their inner structure is significantly modified. Singlet particles or "soot precursors" at the lower region of the flames appear to be mostly amorphous (Figure 27 (a1, b1, c1)) and by the small variation of the axial flame position are transformed into aggregates of a few primary particles with an internal structure that is composed of segments of short graphene layers (Figure 27 (a2, b2, c2)). HR-TEM applied to a section or corner from the "irregular cluster" present in the upper part of the flame exhibits a more graphitized inner structure (Figure 27 (a3, b3, c3)).

HR-TEM imaging on selected areas of the assembled fused primary particles forming the aggregates show that they have well-defined crystallites or so-called graphitic inner structure that is curved, planar and in some regions composed of concentrically stacked curved graphene layers. The necking of the primary particles fused to form the fractal-like aggregates is evident in these HR-TEM images (arrows in Figure 27 (a3, b3, c3)).

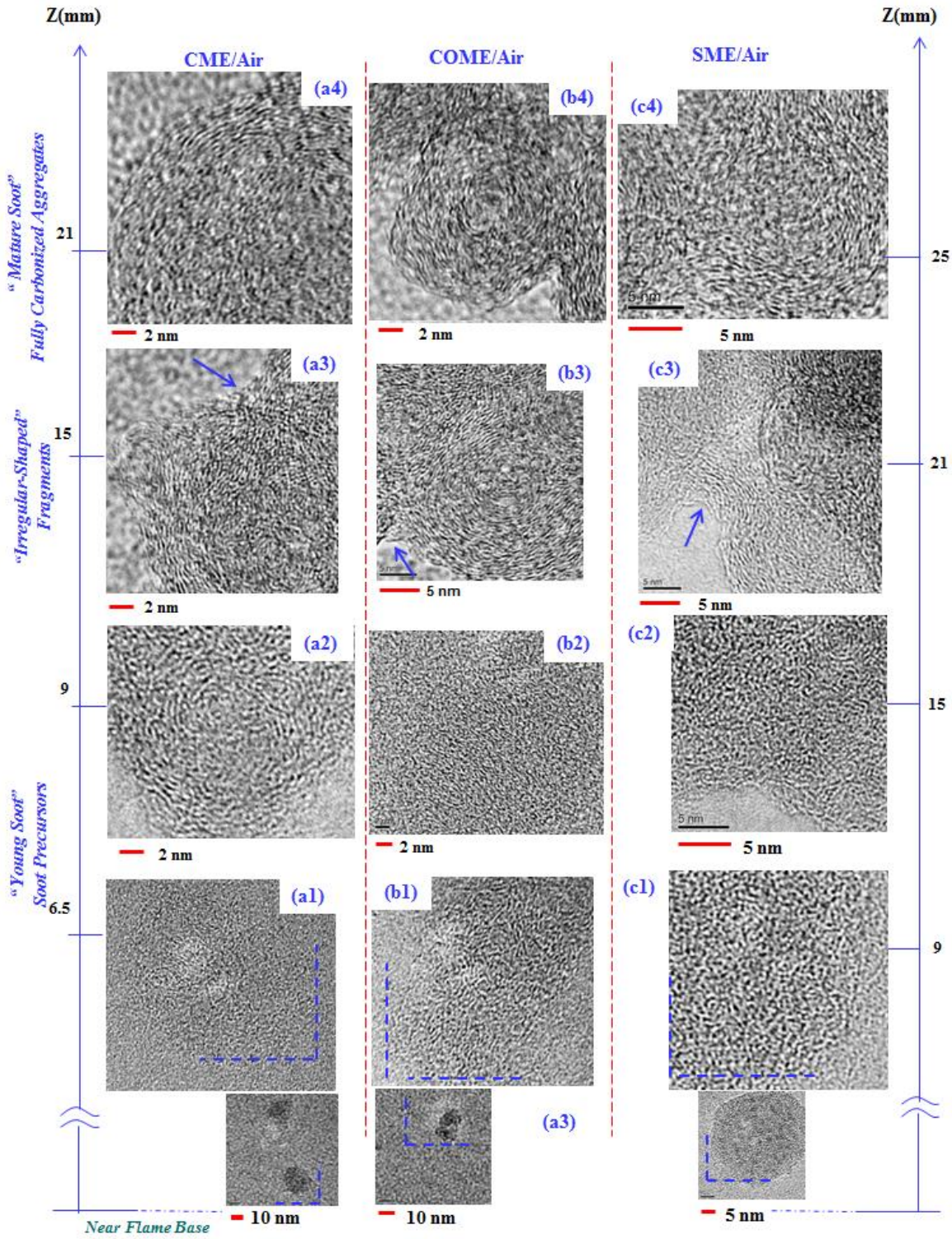

Figure 27. Representative soot nanostructure of "young" and "mature" soot present along the central axis of the three (B100) evaporated biodiesel formed flames at the various HAB. (a1-a4), (b1-b4) and (c1-c4) represent the HR-TEM images of soot collected from the CME, COME and SME air flames, respectively.

Overall, it is interesting to note that the degree of graphitization of the soot in the CME/air and COME/air is enhanced as the flame's tip is approached. The same effect is present in the SME/air flame; however, the process is delayed, and the carbonization process is evident at the flame HAB of 25 mm. Another interesting aspect of the nanostructure study is that the soot formed in the biodiesel flames is comprised of ultra-small carbonized inclusions. The carbonized inclusions are clearly observed as they appear as a material of a darker contrast to the electron beam within the soot (insets in Figure 27 (a1, b1, c1)).

HR-TEM images of soot nanostructure at various HAB of flames formed by diesel, B20, B50, and B80 are presented in Figure 28. Similar to biodiesel flames, HR-TEM images at the lower part of the flames (Figure 28 (a1-a4)) illustrate amorphous tar-like structures without defined boundaries. However, as soot particles travel toward the flame tip, their internal structure are significantly modified with higher degree of graphitization, more ordered graphene layers, and clear boundaries Figure 28 (b1-b4) and (c1-c4). Moving toward the flame tip, the internal structure of soot particles becomes well-ordered with clear carbon layers and sharp boundaries as shown in Figure 28 (d1-d4) and (e1-e4). This characteristic is related to "mature soot" with high degree of carbonization near the flame tip. It is also evident from Figure 28 that the inner region of the mature soot particles or the "core" of the particles are rather amorphous including short and randomly oriented fringes while the outer region of particles or the "shell" is composed of long and radially ordered carbon layers. This core-shell characteristic has been widely reported in the literature for soot nanostructure [292-295]. One interesting observation from Figure 28 is the comparison between diesel and blended fuels. The

degree of curvature seems to be higher and the layers seem to be shorter in the case of blending (Figure 28 (d2-d4), (e2-e4)) compared to rather long, linear and straight graphene layers in the diesel flame (Figure 28 (d1, e1)).

The HR-TEM studies of the trapped carbon particles or "young soot" from the biodiesel flames (region just below the middle of the flames) show that the inner structure is composed of shorter graphene layers that are arranged in an irregular manner compared to the soot nanostructure formed in the #2 diesel flame where the "young soot" inner particle structure appears to be more organized. From the presented soot evolution profiles, it is evident that for both types of fuels (biodiesels and #2 diesel), the state of graphitization increases in the upper regions of the flame. It is also evident from the soot profiles that the carbon layers forming the inner structure of the "mature soot" in the #2 diesel flame (Figure 28) appear to be of a lower degree of curvature compared to those of the biodiesel flame (Figure 27) at similar flame position. It has been suggested by Vander Wal et al. [289] that curvature of a graphene layer in soot results from the presence of five-member rings of aromatics. Curved carbon layers have weaker C-C bonds (so they can be broken easily) and also oxidizing agents (O_2 and mostly OH) can attack them at more points due to their structure compared to a straight chain [289] (Figure 29). That could be another reason behind the higher rate of oxidation in the biodiesel flame than the diesel flame.

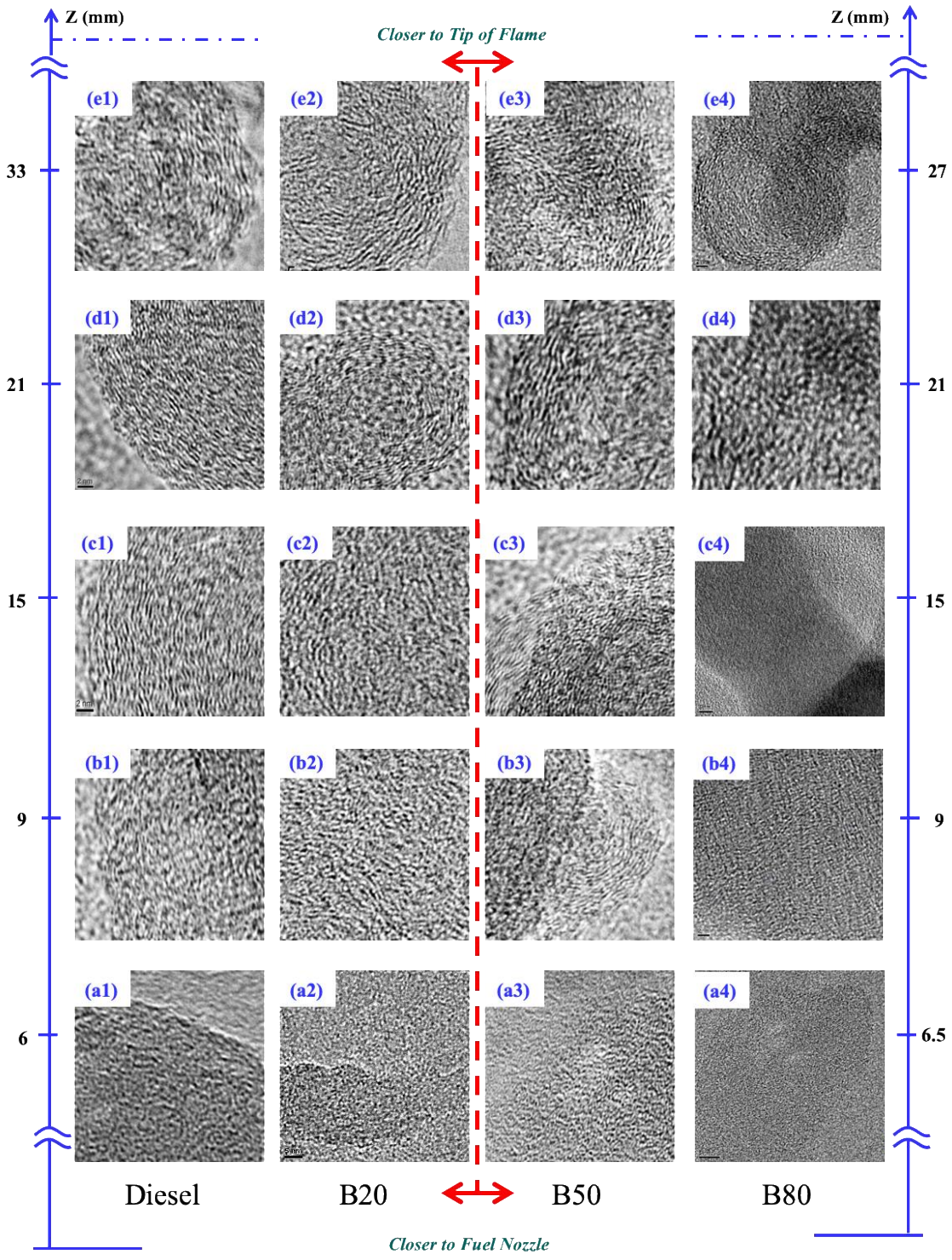

Figure 28. Representative soot nanostructure of "young" and "mature" soot present along the central axis of evaporated blends and diesel formed flames at the various HAB. (a1-e1), (a2-e2), (a3-e3), and (a4-e4) represent the HR-TEM images of soot collected from the diesel, B20, B50, and B80 air flames, respectively.

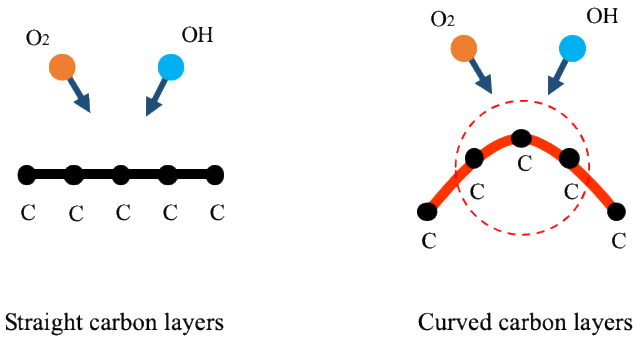

Figure 29. Curved carbon layers (results from five-member rings of aromatics) have weaker C-C bonds and also are more prone to oxidizing agents (O_2 and mostly OH) leading to a stronger soot oxidation.

6.2 Imaging analysis and statistical data

Imaging analysis has been used extensively to analyze soot nanostructure in order to obtain statistical information on soot characteristics and its reactivity. High-resolution transmission electron microscopy (HR-TEM) is capable of revealing the graphitic structure (nanostructure) of soot and allows to directly measure the length, orientation, curvature, and spacing of graphitic fringes [296]. Many studies have been conducted to analyze and characterize the soot nanostructure and relate it to fuel type, combustion conditions, and oxidative reactivity [287, 289, 297-300]. The most common fringe parameters studied in the literature are length, tortuosity, and fringe separation [300-304]. The fringe length measures the physical extent of the atomic carbon layer planes [305]. Larger fringe lengths means the material has fewer crystallites or grain boundaries and is considered to be more similar to graphite [305, 306]. The length of a fringe in a skeletonized (one-pixel thickness) image is obtained by summing the distant between the first pixel of the fringe and the next pixel cumulatively. Figure 30 illustrates a fringe (dark

pixels) with the distant between adjacent pixels. The distant between two adjacent pixels are either 1 if aligned vertically or horizontally or $\sqrt{2}$ if aligned diagonally (Figure 30). Tortuosity measures the curvature of a fringe implying the extent of 5- and 7-membered carbon rings [301, 307, 308]. Tortuosity is an indication of disorder within the material and is defined by the ratio of the fringe length to the distant between the fringe endpoints (Figure 30). Therefore, the lowest possible value of tortuosity is 1 (for a straight fringe) and the value increases with increasing the curvature. fringe separation is the mean distance between neighboring carbon layer planes. In order to obtain the most reliable result, the spacing is measured manually by finding parallel adjacent fringes and measuring the normal distant between them.

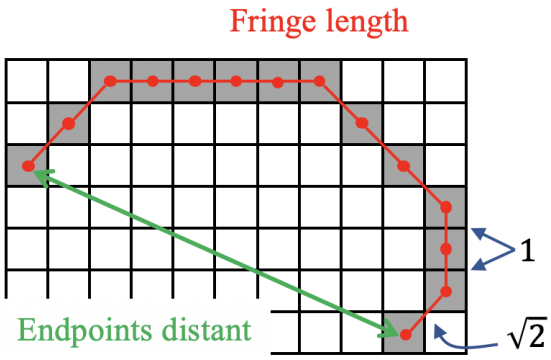

Figure 30. A magnified fringe with various length parameters. The distant between vertically or horizontally aligned pixels is 1 and between diagonally aligned pixels is $\sqrt{2}$.

There are also various image analysis algorithms developed by researchers to extract the statistical data out of the HR-TEM images [303, 305, 309]. The algorithm used in this study is very similar to the one developed by Yehliu et al. [305]. ImageJ was the main software to implement the various steps of the algorithm. The first step is the region of interest (ROI) selection (Figure 31.2). ROI was selected manually to only consider the

sufficient and clear fringes. For instance, the background (carbon film on the TEM grid), irrelevant objects, highly noisy areas, and particles overlapping regions should be avoided when selecting the ROI. All the pixels outside the ROI are deleted before processing the image. The next step is the contrast enhancement (Figure 31.3). A high contrast image has a large difference between the highest and lowest intensity levels. The image contrast was increased by ImageJ with histogram equalization option turned on which transforms the image intensity histogram into a uniform probability density function as suggested by Ref. [305]. While applying histogram equalization improves the contrast of the image, it also increases the contrast of the background noise which affects the robustness of the algorithm, especially the processes after the image binarization [305]. Therefore, a Gaussian lowpass filter is applied as the following step in order to lessen the high-frequency noise [310] (Figure 31.4). If the binarization is applied at this point (after lowpass filter), the result would be inaccurate due to the uneven illumination which is common in HR-TEM images. The binarization applies a threshold across the whole image leading to areas with undistinguishable fringes due to uneven illumination. This issue can be addressed by applying various thresholds for different regions of the image [310]. A top-hat transformation can correct the uneven illumination by subdividing the image into multiple regions and thresholding each region separately [304, 305, 310]. In this study, a top-hat transformation with a disk element of 5 pixels size (as suggested by Ref. [305]) has been applied to images by “MorphoLibJ” plugin in ImageJ (Figure 31.5). The next step is binarization which converts all the gray pixels into black and white pixels based on the given threshold which is necessary in order to extract lattice the fringes from the background [300, 303, 304] (Figure 31.6). Here the threshold was applied using Otsu’s

method which is one of the most common method in the literature as suggested by many authors [305, 311-315]. After performing the morphological corrections (opening and closing) (Figure 31.7,8), the skeletonization was applied by a built-in plugin in ImageJ which has been suggested in the literature [227]. Skeletonization is a necessary process to extract the fringes statistical information [227, 305] (Figure 31.9). ImageJ "AnalyzeSkeletons" plugin was then employed to calculate the fringe length and tortuosity [227]. Removing the fringes which are smaller than a minimum value is a necessary step in order to separate the recognizable fringes from smaller objects with insufficient features to be distinguish from noisy or noncrystalline structures [227, 305, 313] (Figure 31.10). However, various minimum values have been suggested in the literature. Values such as 0.264 nm [316], 1.5 nm [303], 0.4 nm [301], and 0.483 nm [313] have been used. In this study, we followed Botero et al. [313] who suggested the 0.483 nm which is the length of two aromatic rings. Figure 31 provides a complete set of processed images corresponding to each mentioned step in the imaging analysis algorithm.

A set of histograms for the fringes length of soot particles extracted near the flame tip is provided by Figure 32. Soot particles near the flame tip have been selected for the image analysis due to their fully carbonized characteristics, clear fringes, and sharp boundaries. Additionally, considering soot samples near the flame tip leads to a better comparison between flames with various heights providing a normalized height.

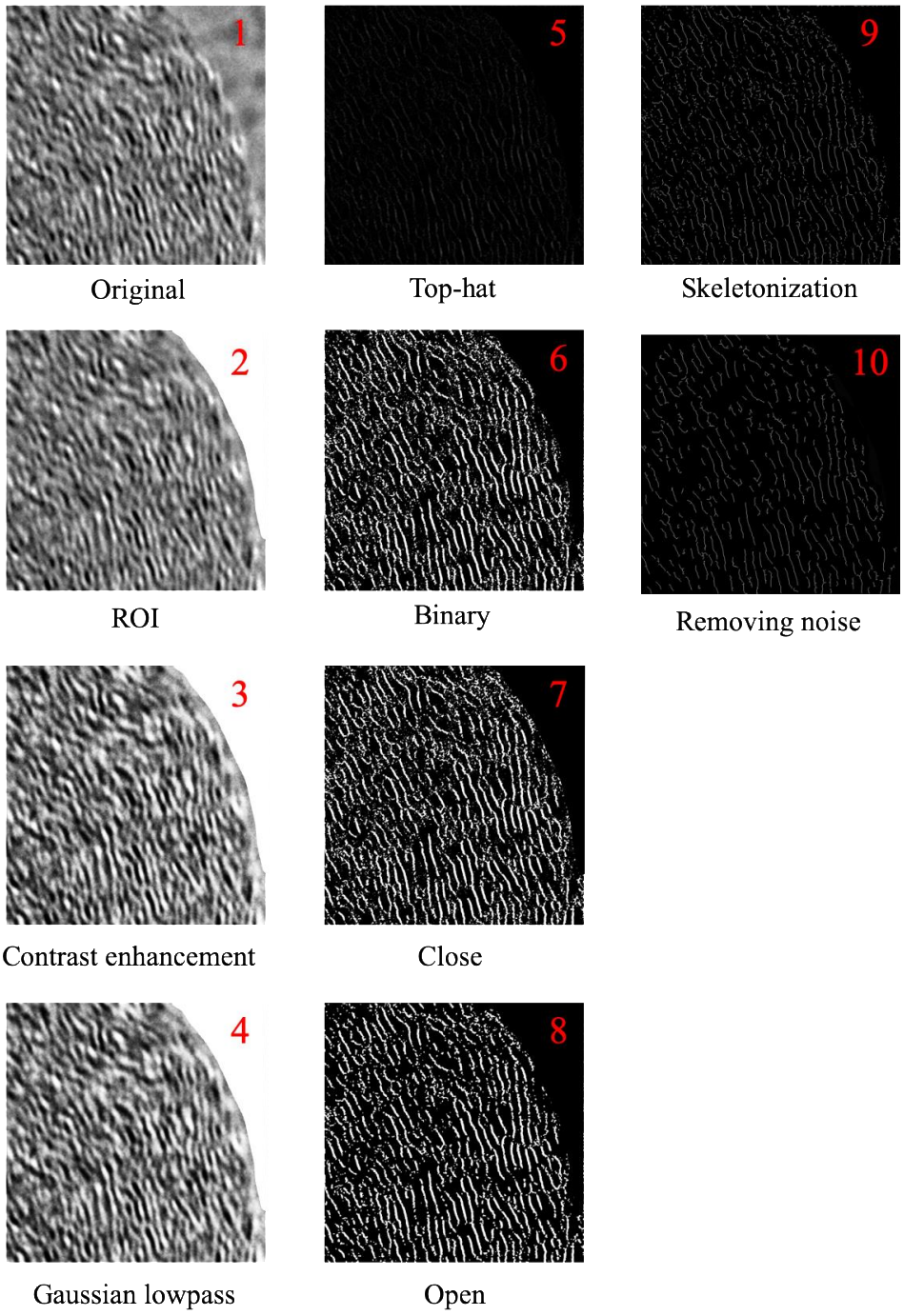

Figure 31. Consecutive implementation of the image processing algorithm employed in this study. The numbering shows the sequence of processes.

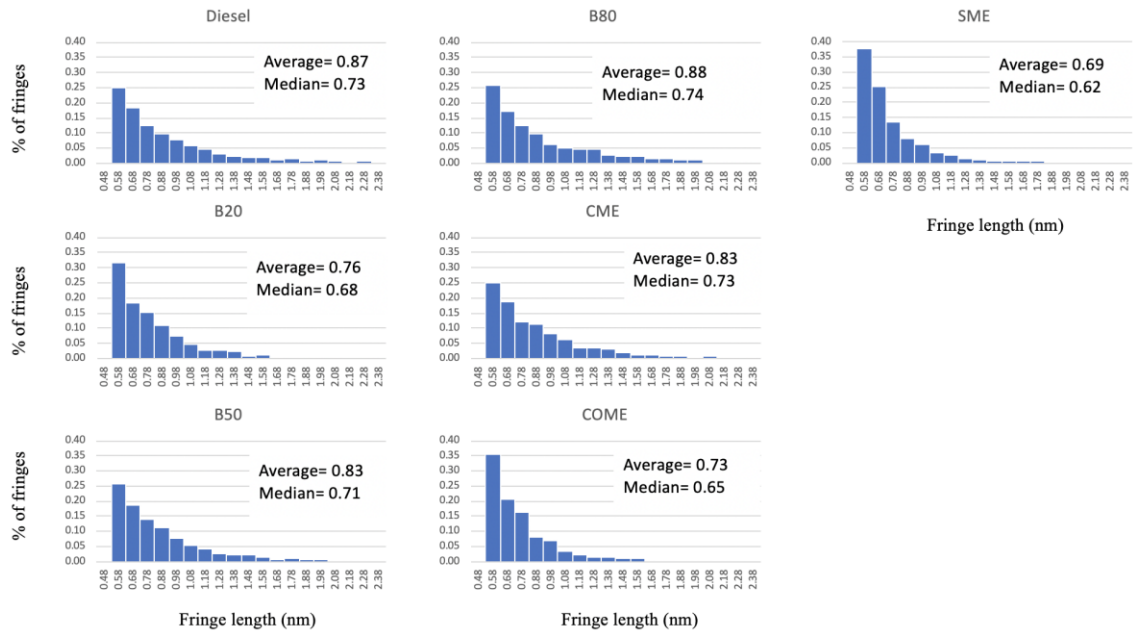

Figure 32. Histograms of fringes length of soot from near the tip of the studied flames.

A simple inspection of Figure 32 shows the shortest fringes for SME and COME with more than 35% of fringes shorter than 0.58 nm. Other fuels show very similar fringe length histograms while diesel seems to have the longest fringe length overall with highest average (Figure 32). It is widely accepted that biodiesel and oxygenated fuels tend to form more amorphous soot particles with shorter length in comparison with diesel [227, 289, 298]. Therefore, our obtained fringe lengths are consistent with the trend reported in the literature with the highest value for diesel and the lowest for biodiesel.

The tortuosity histograms which indicate the degree of curvature of carbon fringes are provided in Figure 33. It is clear from Figure 33 that diesel led to the lowest tortuosity values with around 30% of fringes with a maximum tortuosity of 1.1. This indicates the diesel soot particles compose of straight and linear fringes. On the other hand, SME and COME led to the highest degree of curvature with only less than 15% of fringes with a

tortuosity of 1.2 or lower suggesting highly curved fringes (Figure 33). This observed trend (more curved fringes in case of biodiesel and blending compared to diesel) has also been widely reported in the literature [227, 289, 298].

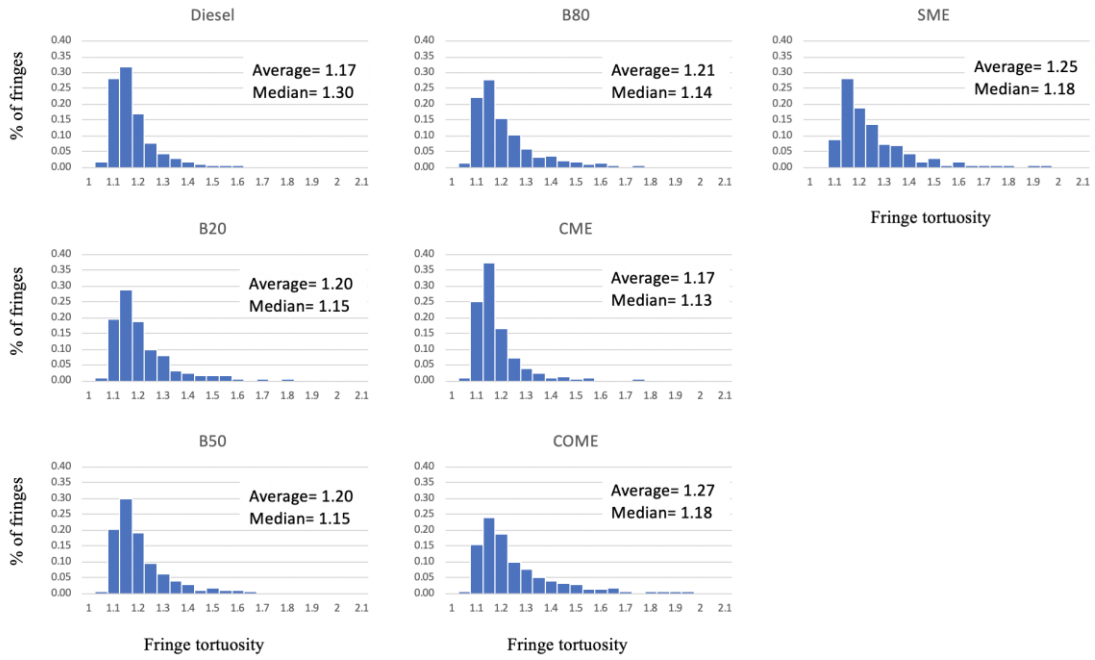

Figure 33. Histograms of fringes tortuosity of soot from near the tip of the studied flames.

The spacing between graphene fringes is another important parameter to characterize the nanostructure of soot particles. As reported in Figure 34, all biodiesels and blended fuels produced soot particles whit higher interlayer lattice spacing compared to diesel. Higher interlayer spacing can be an indication of higher degree of graphitization [227, 315]. As shown in Figure 32-Figure 34, diesel soot particles showed the highest degree of graphitization with the shortest fringes, highest tortuosity, and highest interlayer separation compared to biodiesel and blended fuels. The same trend has been reported in the literature [227, 298, 305, 315, 317] which can validate our obtained result.

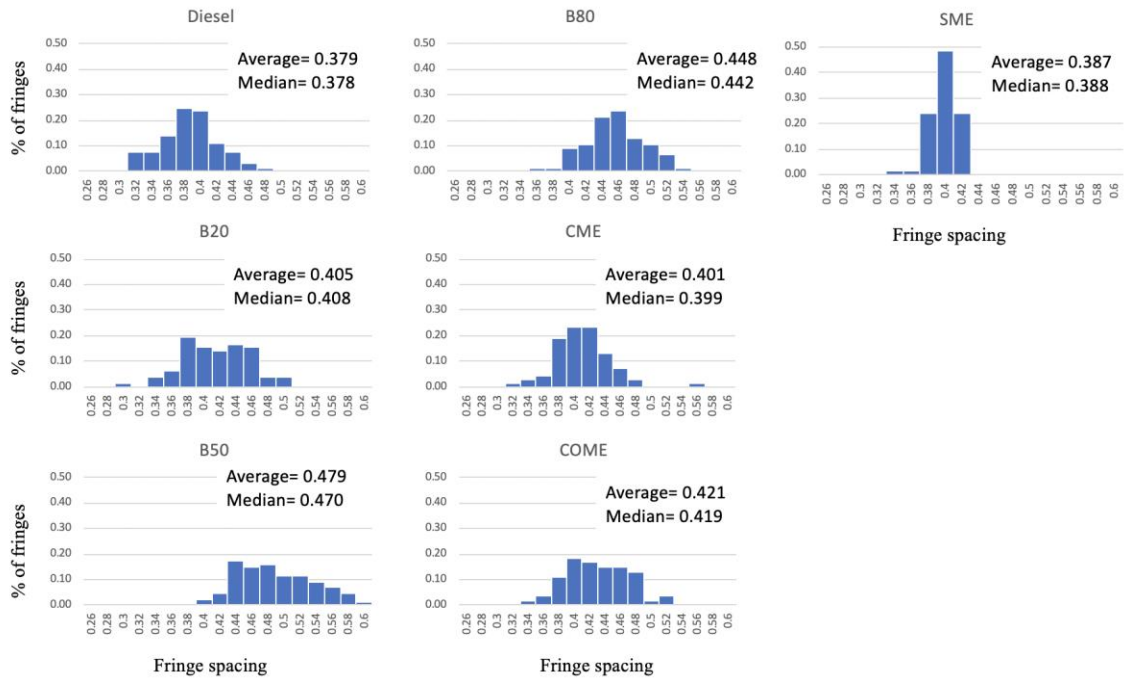

Figure 34. Histograms of fringes distance (spacing) of soot from near the tip of the studied flames.

7 Conclusions

In this study the soot evolution profiles on the formation of carbon particulates (physical characteristics) in co-flow diffusion flames formed by three different vaporized biodiesels, #2 diesel, and various blends of biodiesel/diesel were obtained. For all studied flames, air is used as the oxidizer. Canola methyl ester (CME), soy methyl ester (SME), and cotton methyl ester (COME) have been studied due to their popularity. The blended fuels are obtained by volumetric mixtures of CME and #2 diesel with various concentrations: B20, B50, and B80. Soot samples were thermophoretically collected from the centerline of formed diffusion flames at various heights above the burner followed by transmission electron microscopy (TEM) imaging. The attained soot evolution profiles in all tested flames show the typical soot formation process. That is, particle inception (singlet particles) or "young soot" is present at the lower part of the flame followed by the presence of particle growth "mature soot" and oxidation in the upper regions of the flame. However, it was found that there are some unique differences in the characteristics of the soot evolutions in the flames formed by biodiesel and blended fuels compared to those present in the diesel flame. The singlet particles or "soot precursors" present in the lower region of the biodiesel flames are much smaller in size compared to those in the diesel flame. In the biodiesel and blended fuel flames the presence of large "irregular-shaped" fragments or "globule" structures is typical of their soot evolution. At approximately the middle region of the flame, "irregular-shaped" structures are evident. The "irregular-shaped" structures have the following morphological characteristics: (i) resemble large eutectic (solid/liquid) manifesting the viscous liquid nature; (ii) some of these "irregular-shaped" clusters containing embedded carbonized inclusions that can be

easily identified as they have a darker contrast; (iii) from the TEM results it can be suggested that the "irregular-shaped" structures serve as possible growth pathways for the formation of aggregates composed of nearly spherical shaped and fully carbonized particles in the upper part of the flame.

The soot evolution obtained in the blended flames resemble those present in the parent fuel. For instance, the peak d_p value for B20 flame approaches that of the parent fuel (in this case the #2 diesel). That is, the diameter of the primary particles increases as the percentage of diesel in the blending mixture increases. The increase of biodiesel percentage in the blended mixture enhances the formation of long chain-like aggregates composed of a high number of soot primary particles with higher degree of networks. On the other hand, the aggregates formed in the diesel flame are shorter and not as heavily linked as in the biodiesel flame. It was found that when the fuel blend was obtained using equal proportions (B50), the morphology of the soot is rather complex and it is difficult to identify the boundaries of the primary particles forming the aggregates, thus making it difficult to obtain a peak dp value for this blended flame.

In order to statistically investigate the morphology of soot particulates, several morphological and structural parameters are obtained by computer-aided imaging analysis. Fractal dimension (D_f), aggregate skeleton length (SL), and number of junctions (NJ) of soot aggregates are obtained to characterize the soot morphology. All tested biodiesels and blended fuels led to soot aggregates with higher NJ (higher branching) but lower D_f (more open structure) compared to diesel. Compared to diesel, all tested fuels, except B20, enhanced the number of soot precursors structures leading to highly branched and long-stretched fractal objects with very long skeleton length near the flame tip. Fuel

chemistry, especially the carbon chain length and the degree of unsaturation, is hypothesized to be the main reason behind the different soot morphology even among biodiesels and blends. Soot agglomeration and carbonization evolution could be another justification for the very large and extended aggregates observed in biodiesel, B50, and B80 flames. When the carbonization happens early and prior to the dominance of monomer-cluster aggregation, final soot fractals become more compact which is the case inside the diesel flame. On the other hand, the late carbonization after the dominance of monomer-cluster scheme results in more open-structured and stretched aggregates due to the presence of large droplet-like structures which is observed inside the biodiesel, B50, and B80 flames. The lowest D_f value for B20 implies the late carbonization inside the B20 flame. However, large droplet-like structures are not evident inside the B20 flame which might be a result of the low number of singlet particles with small diameter. Having the lower D_f, biodiesel soot fractals can have a longer suspension time in air due to their higher dynamic shape factor, but they can be more easily trapped in particulate filters before being released to the atmosphere due to their open and chain-like structure and larger size. Besides having soot particles with lower D_f, another advantage of using biodiesel is their smaller soot primary particles which can be easily oxidized to reuse the particulate filters.

Soot nanostructure is also studied due to its importance in characterizing the degree of graphitization and their oxidative reactivity. Graphene layers are captured by high-resolution TEM (HR-TEM) images and analyzed by computer-aided imaging analysis. The length, tortuosity (degree of curvature), and interlayer spacing of carbon fringes are obtained for tested fuels. The impact of biodiesel and blended fuels on soot

internal structure is evident as they resulted in shorter and less organized fringes with a higher degree of curvature and also with smaller interlayer spacing compared to diesel. All of these observations imply the more amorphous and less graphitized characteristics for biodiesel and blending with respect to diesel. The amorphous structure with highly curved layers facilitates the oxidation and enhance the oxidative reactivity of biodiesel soot particles which again enhance the effectiveness of particulate filters.

Biodiesel is observed to influence the size, morphology, evolution mechanism, and internal structure of soot particles significantly. Even a 20% addition of biodiesel into diesel fuels can lessen the soot emission and enhance the efficiency of after-treatment devices. Using biodiesel/diesel blends is very helpful to take advantage of biodiesel positive impacts on environment with no or minor engine modification, and at the same time keeping the fuel price reasonable compared to pure biodiesel.

8 References

1. Dhinesh, B., et al., *An assessment on performance, emission and combustion characteristics of single cylinder diesel engine powered by Cymbopogon flexuosus biofuel.* Energy Conversion and Management, 2016. **117**: p. 466-474.

2. Abdul Karim, S.A., et al., *Diesel Engine Performance Operating with Tire Derived Fuel.* MATEC Web of Conferences, 2018. **225**.

3. Agency, I.E., *World Energy Balances, https://doi.org/10.1787/world_energy_bal-2017-en.* 2017.

4. Maurya, R.K., et al., *Effect of compression ratio, nozzle opening pressure, engine load, and butanol addition on nanoparticle emissions from a non-road diesel engine.* Environ Sci Pollut Res Int, 2018. **25**(15): p. 14674-14689.

5. Yamaki, Y., et al., *Application of Common Rail Fuel Injection System to a Heavy Duty Diesel Engine.* SAE Transactions, 1994. **103**: p. 1977-1988.

6. Li, Y., C. Wan, and C. Liu, *Study on emission characteristics of biodiesel fuel for heavy diesel vehicles.* IOP Conference Series: Materials Science and Engineering, 2018. **394**.

7. (IARC), I.A.f.R.o.C., *Diesel engine exhaust carcinogenic.* 2012.

8. Peters, A., et al., *Translocation and potential neurological effects of fine and ultrafine particles a critical update.* Particle and fibre toxicology, 2006. **3**(1): p. 13.

9. Harrod, K.S., et al., *Inhaled diesel engine emissions reduce bacterial clearance and exacerbate lung disease to Pseudomonas aeruginosa infection in vivo.* Toxicological Sciences, 2004. **83**(1): p. 155-165.

10. Geng, P., H. Zhang, and S. Yang, *Experimental investigation on the combustion and particulate matter (PM) emissions from a port-fuel injection (PFI) gasoline engine fueled with methanol–ultralow sulfur gasoline blends.* Fuel, 2015. **145**: p. 221-227.

11. Organization., W.H., *Ambient (outdoor) air quality and health. http://www.who.int/en/news-room/fact-sheets/detail/ambient-(outdoor)-air-quality-and-health.* 2018.

12. Veltman, M.K., P.K. Karra, and S.-C. Kong, *Effects of biodiesel blends on emissions in low temperature diesel combustion*. 2009, SAE Technical Paper.

13. Taghavifar, H., S. Khalilarya, and S. Jafarmadar, *Engine structure modifications effect on the flow behavior, combustion, and performance characteristics of DI diesel engine.* Energy conversion and management, 2014. **85**: p. 20-32.

14. Alkemade, U.G. and B. Schumann, *Engines and exhaust after treatment systems for future automotive applications.* Solid State Ionics, 2006. **177**(26-32): p. 2291-2296.

15. Johnson, T., *Review of diesel emissions and control*. International Journal of Engine Research, 2009. **10**(5): p. 275-285.

16. Stamatelos, A., *A review of the effect of particulate traps on the efficiency of vehicle diesel engines.* Energy conversion and management, 1997. **38**(1): p. 83-99.

17. Maurya, R.K., et al., *Effect of compression ratio, nozzle opening pressure, engine load, and butanol addition on nanoparticle emissions from a non-road diesel engine.* Environmental Science and Pollution Research, 2018. **25**(15): p. 14674-14689.

18. Geng, P., et al., *Effects of alternative fuels on the combustion characteristics and emission products from diesel engines: A review*. Renewable and Sustainable Energy Reviews, 2017. **71**: p. 523-534.

19. Demirbas, A., *Biodiesel*. 2008: Springer.

20. Li, Y., C. Wan, and C. Liu. *Study on emission characteristics of biodiesel fuel for heavy diesel vehicles*. in *IOP Conference Series: Materials Science and Engineering*. 2018. IOP Publishing.

21. Helwani, Z., et al., *Solid heterogeneous catalysts for transesterification of triglycerides with methanol: a review.* Applied Catalysis A: General, 2009. **363**(1-2): p. 1-10.

22. Nguyen, T., L. Do, and D.A. Sabatini, *Biodiesel production via peanut oil extraction using diesel-based reverse-micellar microemulsions.* Fuel, 2010. **89**(9): p. 2285-2291.

23. Patil, P.D. and S. Deng, *Optimization of biodiesel production from edible and non-edible vegetable oils.* Fuel, 2009. **88**(7): p. 1302-1306.

24. Okitsu, K., et al., *Ultrasound-assisted production of biodiesel fuel from vegetable oils in a small scale circulation process.* Bioresource Technology, 2010. **101**(2): p. 639-645.

25. Bartholomew, D., *Vegetable oil fuel.* Journal of the American Oil Chemists' Society, 1981. **58**(4): p. 286A-288A.

26. Nitske, W.R. and C.M. Wilson, *Rudolph Diesel: Pioneer of the Age of Power*. 1965: University of Oklahoma Press.

27. Ma, F. and M.A. Hanna, *Biodiesel production: a review.* Bioresource technology, 1999. **70**(1): p. 1-15.

28. Ayhan, D., *Biodiesel a Realistic Fuel Alternative for Diesel Engines.* ISBN-13: 9781846289941, 2008.

29. Ma, F. and A. Milford, *Hanna. biodiesel production: a review.* Bioresource Technology, 1999. **70**(1): p. 1-15.

30. Ramsey, W., *Proceedings of the International Conference on Plant and Vegetable Oils as Fuels.* 1982.

31. Balat, M. and H. Balat, *A critical review of bio-diesel as a vehicular fuel.* Energy Conversion and Management, 2008. **49**(10): p. 2727-2741.

32. Tamilselvan, P., N. Nallusamy, and S. Rajkumar, *A comprehensive review on performance, combustion and emission characteristics of biodiesel fuelled diesel engines.* Renewable and Sustainable Energy Reviews, 2017. **79**: p. 1134-1159.

33. Hoekman, S.K. and C. Robbins, *Review of the effects of biodiesel on NOx emissions.* Fuel Processing Technology, 2012. **96**: p. 237-249.

34. Bondioli, P., et al., *Evaluation of biodiesel storage stability using reference methods.* European journal of lipid science and technology, 2002. **104**(12): p. 777-784.

35. Demirbas, A., *Importance of biodiesel as transportation fuel.* Energy policy, 2007. **35**(9): p. 4661-4670.

36. Tenenbaum, D.J., *Food vs. Fuel: Diversion of Crops Could Cause More Hunger.* Environmental Health Perspectives, 2008. **116**(6).

37. Royon, D., et al., *Enzymatic production of biodiesel from cotton seed oil using t-butanol as a solvent.* Bioresource technology, 2007. **98**(3): p. 648-653.

38. Kumar, N. and P. Sharma, *Jatropha curcus-A sustainable source for production of biodiesel.* 2005.

39. Campbell, M.N., *Biodiesel: algae as a renewable source for liquid fuel.* Guelph Engineering Journal, 2008. **1**(1): p. 2-7.

40. Ali, M.H., et al., *Biodiesel from Neem oil as an alternative fuel for Diesel engine.* Procedia Engineering, 2013. **56**: p. 625-630.

41. Hannon, M., et al., *Biofuels from algae: challenges and potential.* Biofuels, 2010. **1**(5): p. 763-784.

42. Mueller, C.J., A.L. Boehman, and G.C. Martin, *An Experimental Investigation of the Origin of Increased NO_x Emissions When Fueling a Heavy-Duty Compression-Ignition Engine with Soy Biodiesel.* SAE International Journal of Fuels and Lubricants, 2009. **2**(1): p. 789-816.

43. Huesemann, M.H., et al., *Biomass Productivities in Wild Type and Pigment Mutant of Cyclotella sp. (Diatom).* Applied Biochemistry and Biotechnology, 2009. **157**(3): p. 507-526.

44. Demirbas, A., *Progress and recent trends in biodiesel fuels.* Energy conversion and management, 2009. **50**(1): p. 14-34.

45. Roy, M.M., W. Wang, and J. Bujold, *Biodiesel production and comparison of emissions of a DI diesel engine fueled by biodiesel–diesel and canola oil–diesel blends at high idling operations.* Applied Energy, 2013. **106**: p. 198-208.

46. Canakci, M., *Combustion characteristics of a turbocharged DI compression ignition engine fueled with petroleum diesel fuels and biodiesel.* Bioresource technology, 2007. **98**(6): p. 1167-1175.

47. Demirbaş, A., *Biodiesel fuels from vegetable oils via catalytic and non-catalytic supercritical alcohol transesterifications and other methods: a survey.* Energy conversion and Management, 2003. **44**(13): p. 2093-2109.

48. Lang, X., et al., *Preparation and characterization of bio-diesels from various bio-oils.* Bioresource technology, 2001. **80**(1): p. 53-62.

49. Gülüm, M. and A. Bilgin, *Density, flash point and heating value variations of corn oil biodiesel–diesel fuel blends.* Fuel Processing Technology, 2015. **134**: p. 456-464.

50. Rashid, U., F. Anwar, and G. Knothe, *Evaluation of biodiesel obtained from cottonseed oil.* Fuel Processing Technology, 2009. **90**(9): p. 1157-1163.

51. Alptekin, E. and M. Canakci, *Determination of the density and the viscosities of biodiesel–diesel fuel blends.* Renewable Energy, 2008. **33**(12): p. 2623-2630.

52. Chiu, C.-W., L.G. Schumacher, and G.J. Suppes, *Impact of cold flow improvers on soybean biodiesel blend.* Biomass and Bioenergy, 2004. **27**(5): p. 485-491.

53. Kulkarni, M.G., A. Dalai, and N. Bakhshi, *Transesterification of canola oil in mixed methanol/ethanol system and use of esters as lubricity additive.* Bioresource technology, 2007. **98**(10): p. 2027-2033.

54. Saydut, A., et al., *Process optimization for production of biodiesel from hazelnut oil, sunflower oil and their hybrid feedstock.* Fuel, 2016. **183**: p. 512-517.

55. Imahara, H., et al., *Thermal stability of biodiesel in supercritical methanol.* Fuel, 2008. **87**(1): p. 1-6.

56. Demirbas, A., *Production of biodiesel fuels from linseed oil using methanol and ethanol in non-catalytic SCF conditions.* Biomass and bioenergy, 2009. **33**(1): p. 113-118.

57. Jham, G.N., et al., *Wild Brazilian mustard (Brassica juncea L.) seed oil methyl esters as biodiesel fuel.* Journal of the American Oil Chemists' Society, 2009. **86**(9): p. 917-926.

58. Benjumea, P., J. Agudelo, and A. Agudelo, *Basic properties of palm oil biodiesel–diesel blends.* Fuel, 2008. **87**(10-11): p. 2069-2075.

59. Ilkılıç, C., et al., *Biodiesel from safflower oil and its application in a diesel engine.* Fuel processing technology, 2011. **92**(3): p. 356-362.

60. Bala, B., *Studies on biodiesels from transformation of vegetable oils for diesel engines.* Energy Education Science and Technology, 2005. **15**(1/2): p. 1.

61. Kinast, J.A., *Production of Biodiesels From Multiple Feedstocks and Properties of Biodiesels and Biodiesel/Diesel Blends: Final Report; Report 1 in a Series of 6*. 2003, National Renewable Energy Lab., Golden, CO.(US).

62. Prakash, C., *A Critical Review of Biodiesel as a Transportation Fuel in Canada", Report to Transportation System Branch, Air Pollution Prevention Directorate, R gasification Biomass to produce Hydrogen Rich Gas.* Int. J. Hydrogen Energy, 1998. **23**: p. 551-557.

63. Salamanca, M., et al., *Variations in the chemical composition and morphology of soot induced by the unsaturation degree of biodiesel and a biodiesel blend.* Combustion and Flame, 2012. **159**(3): p. 1100-1108.

64. Boehman, A.L., J. Song, and M. Alam, *Impact of biodiesel blending on diesel soot and the regeneration of particulate filters.* Energy & Fuels, 2005. **19**(5): p. 1857-1864.

65. Lapuerta, M., O. Armas, and J. Rodriguez-Fernandez, *Effect of biodiesel fuels on diesel engine emissions.* Progress in energy and combustion science, 2008. **34**(2): p. 198-223.

66. Szybist, J.P., et al., *Biodiesel combustion, emissions and emission control.* Fuel processing technology, 2007. **88**(7): p. 679-691.

67. Ozil, F., et al., *Efficiency of catalytic processes for the reduction of CO and VOC emissions from wood combustion in domestic fireplaces.* Fuel Processing Technology, 2009. **90**(9): p. 1053-1061.

68. Pisupati, S.V. and S. Bhalla, *Numerical modeling of NOx reduction using pyrolysis products from biomass-based materials.* Biomass and Bioenergy, 2008. **32**(2): p. 146-154.

69. Schumacher, L., et al., *Fueling diesel engines with blends of methyl ester soybean oil and diesel fuel. Available on line*. 1994.

70. Marshall, W., L.G. Schumacher, and S. Howell, *Engine exhaust emissions evaluation of a Cummins L10E when fueled with a biodiesel blend*. 1995, SAE Technical Paper.

71. Yuan, W., et al., *Spray, ignition, and combustion modeling of biodiesel fuels for investigating NOx emissions.* Transactions of the ASAE, 2005. **48**(3): p. 933-939.

72. Serdari, A., et al., *Effect of biodiesel addition to diesel fuel on engine performance and emissions.* Journal of propulsion and power, 1999. **15**(2): p. 224-231.

73. Staat, F. and P. Gateau, *The effects of rapeseed oil methyl ester on diesel engine performance, exhaust emissions and long-term behavior-a summary of three years of experimentation.* SAE transactions, 1995: p. 1-7.

74. Hamasaki, K., et al. *(3-09) Combustion Characteristics of Diesel Engines with Waste Vegetable Oil Methyl Ester ((AF-3) Alternative Fuels 3-Biomass Fuels and Fuel Design)*. in *The Proceedings of the International symposium on diagnostics and modeling of combustion in internal combustion engines 01.204*. 2001. The Japan Society of Mechanical Engineers.

75. Dorado, M., et al., *Exhaust emissions from a Diesel engine fueled with transesterified waste olive oil ⁎.* Fuel, 2003. **82**(11): p. 1311-1315.

76. Peterson, C.L. and D.L. Reece, *Emissions testing with blends of esters of rapeseed oil fuel with and without a catalytic converter*. 1996, SAE Technical Paper.

77. Lapuerta, M., et al., *Diesel emissions from biofuels derived from Spanish potential vegetable oils.* Fuel, 2005. **84**(6): p. 773-780.

78. Mohan, B., et al., *Experimental study of spray characteristics of biodiesel derived from waste cooking oil.* Energy conversion and management, 2014. **88**: p. 622-632.

79. Zhang, X. and G. Gao. *Liguang Li, Zhijun Wu, Zongglie Hu and Jun Deng," Characteristics of Combustion and Emissions in a DI Engine Fueled with Biodiesel Blends from Soybean Oil," SAE paper 2008-01-1832, 2008 SAE International Powertrains*. in *Fuels and Lubricants Congress, Shanghai, China Jun*. 2008.

80. Crua, C., et al., *Dropsizing of near-nozzle diesel and RME sprays by microscopic imaging.* 2012.

81. Wang, X., et al., *Experimental and analytical study on biodiesel and diesel spray characteristics under ultra-high injection pressure.* International journal of heat and fluid flow, 2010. **31**(4): p. 659-666.

82. Moon, S., et al., *Biodiesel effects on transient needle motion and near-exit flow characteristics of a high-pressure diesel injector.* International Journal of Engine Research, 2014. **15**(4): p. 504-518.

83. Hwang, J., Y. Jung, and C. Bae, *Spray and combustion of waste cooking oil biodiesel in a compression-ignition engine.* International Journal of Engine Research, 2015. **16**(5): p. 664-679.

84. Kaplan, C., R. Arslan, and A. Sürmen, *Performance characteristics of sunflower methyl esters as biodiesel.* Energy Sources, 2006. **28**(8): p. 751-755.

85. Altıparmak, D., et al., *Alternative fuel properties of tall oil fatty acid methyl ester–diesel fuel blends.* Bioresource Technology, 2007. **98**(2): p. 241-246.

86. Usta, N., *An experimental study on performance and exhaust emissions of a diesel engine fuelled with tobacco seed oil methyl ester.* Energy Conversion and Management, 2005. **46**(15-16): p. 2373-2386.

87. Graboski, M., J. Ross, and R. McCormick, *Transient emissions from No. 2 diesel and biodiesel blends in a DDC series 60 engine*. 1996, SAE Technical Paper.

88. Rakopoulos, C.D., et al., *Operational and environmental evaluation of diesel engines burning oxygen-enriched intake air or oxygen-enriched fuels: a review.* SAE transactions, 2004: p. 1723-1743.

89. Tsolakis, A., *Effects on particle size distribution from the diesel engine operating on RME-biodiesel with EGR.* Energy & Fuels, 2006. **20**(4): p. 1418-1424.

90. Senatore, A., et al., *A comparative analysis of combustion process in DI diesel engine fueled with biodiesel and diesel fuel*. 2000, SAE Technical Paper.

91. Lapuerta, M., J. Rodríguez-Fernández, and J.R. Agudelo, *Diesel particulate emissions from used cooking oil biodiesel.* Bioresource Technology, 2008. **99**(4): p. 731-740.

92. Strzelec, A., et al., *Nanostructure and burning mode of light-duty diesel particulate with conventional diesel, biodiesel, and intermediate blends.* International Journal of Engine Research, 2017: p. 1468087416674414.

93. Demirbaş, A., *Biodiesel from vegetable oils via transesterification in supercritical methanol.* Energy conversion and management, 2002. **43**(17): p. 2349-2356.

94. Carraretto, C., et al., *Biodiesel as alternative fuel: experimental analysis and energetic evaluations.* Energy, 2004. **29**(12): p. 2195-2211.

95. Dinkov, R., et al., *Effect of commercially available antioxidants over biodiesel/diesel blends stability.* Fuel, 2009. **88**(4): p. 732-737.

96. Westbrook, S., *An evaluation and comparison of test methods to measure the oxidation stability of neat biodiesel. Report to National Renewable Energy Laboratory*. Contract No DEAC3699GO10337, Sub Contract No ACE3307501, 2005.

97. Ramalho, E., et al., *Low temperature behavior of poultry fat biodiesel: diesel blends.* Fuel, 2012. **93**: p. 601-605.

98. *U.S. Energy Information Administration, Monthly Energy Review,April 2019.*

99. Benjumea, P., J. Agudelo, and A. Agudelo, *Basic properties of palm oil biodiesel–diesel blends.* Fuel, 2008. **87**(10): p. 2069-2075.

100. Kinast, J., *Production of biodiesels from multiple feedstocks and properties of biodiesels and biodiesel/diesel blends.* NREL Final Report, SR-510-31460, 2003.

101. Qi, D., et al., *Experimental studies on the combustion characteristics and performance of a direct injection engine fueled with biodiesel/diesel blends.* Energy Conversion and Management, 2010. **51**(12): p. 2985-2992.

102. Lin, Y.-f., Y.-p.G. Wu, and C.-T. Chang, *Combustion characteristics of waste-oil produced biodiesel/diesel fuel blends.* Fuel, 2007. **86**(12): p. 1772-1780.

103. Wang, W.-G., et al., *Emissions from nine heavy trucks fueled by diesel and biodiesel blend without engine modification.* Environmental Science & Technology, 2000. **34**(6): p. 933-939.

104. Schumacher, L., et al., *Heavy-duty engine exhaust emission tests using methyl ester soybean oil/diesel fuel blends.* Bioresource Technology, 1996. **57**(1): p. 31-36.

105. Pandey, A., *Handbook of plant-based biofuels*. 2008: CRC Press.

106. Buyukkaya, E., *Effects of biodiesel on a DI diesel engine performance, emission and combustion characteristics.* Fuel, 2010. **89**(10): p. 3099-3105.

107. Zheng, M., et al., *Biodiesel engine performance and emissions in low temperature combustion.* Fuel, 2008. **87**(6): p. 714-722.

108. Ramadhas, A., S. Jayaraj, and C. Muraleedharan, *Use of vegetable oils as IC engine fuels—a review.* Renewable energy, 2004. **29**(5): p. 727-742.

109. Bockhorn, H., *Soot formation in combustion: mechanisms and models*. Vol. 59. 2013: Springer Science & Business Media.

110. Tree, D.R. and K.I. Svensson, *Soot processes in compression ignition engines.* Progress in Energy and Combustion Science, 2007. **33**(3): p. 272-309.

111. Christopher Shaddix, T.W., *Soot: Giver and Taker of Light.* American Scientist, 2007. **95**.

112. Leung, K.M., R.P. Lindstedt, and W. Jones, *A simplified reaction mechanism for soot formation in nonpremixed flames.* Combustion and flame, 1991. **87**(3-4): p. 289-305.

113. Frenklach, M., *Reaction mechanism of soot formation in flames.* Physical Chemistry Chemical Physics, 2002. **4**(11): p. 2028-2037.

114. Haynes, B.S. and H.G. Wagner, *Soot formation.* Progress in Energy and Combustion Science, 1981. **7**(4): p. 229-273.

115. Brookes, S. and J. Moss, *Measurements of soot production and thermal radiation from confined turbulent jet diffusion flames of methane.* Combustion and Flame, 1999. **116**(1-2): p. 49-61.

116. Struwe, F. and D.E. Foster, *In-cylinder measurement of particulate radiant heat transfer in a direct injection diesel engine.* SAE transactions, 2003: p. 293-313.

117. Benajes, J., et al., *In-cylinder soot radiation heat transfer in direct-injection diesel engines.* Energy conversion and management, 2015. **106**: p. 414-427.

118. Furmanski, P., J. Banaszek, and T.S. Wisniewski, *Radiation heat transfer in a combustion chamber of diesel engine with partially transparent burnt gas zone*. 1998, SAE Technical Paper.

119. Vögelin, P., P. Obrecht, and K. Boulouchos, *Experimental investigation of multi-in-cylinder pyrometer measurements and exhaust soot emissions under steady and transient operation of a heavy-duty Diesel engine.* SAE International Journal of Engines, 2013. **6**(3): p. 1855-1865.

120. Skeen, S., et al., *Quantitative spatially resolved measurements of total radiation in high-pressure spray flames*. 2014, SAE Technical Paper.

121. Flynn, P., et al., *An experimental determination of the instantaneous potential radiant heat transfer within an operating Diesel engine*. 1972, SAE Technical Paper.

122. Faeth, G. and Ü.Ö. Köylü, *Soot morphology and optical properties in nonpremixed turbulent flame environments.* Combustion science and technology, 1995. **108**(4-6): p. 207-229.

123. Dobbins, R., G.W. Mulholland, and N.P. Bryner, *Comparison of a fractal smoke optics model with light extinction measurements.* Atmospheric Environment, 1994. **28**(5): p. 889-897.

124. Lahaye, J. and G. Prado, *Morphology and internal structure of soot and carbon blacks*, in *Particulate carbon*. 1981, Springer. p. 33-55.

125. Donnet, J.-B., *Carbon black: science and technology*. 1993: CRC Press.

126. Arduini, F., et al., *Electroanalytical characterization of carbon black nanomaterial paste electrode: development of highly sensitive tyrosinase biosensor for catechol detection.* Analytical Letters, 2010. **43**(10-11): p. 1688-1702.

127. Llobet, E., *Gas sensors using carbon nanomaterials: A review.* Sensors and Actuators B: Chemical, 2013. **179**: p. 32-45.

128. Yuan, Y., S. Zhou, and L. Zhuang, *Polypyrrole/carbon black composite as a novel oxygen reduction catalyst for microbial fuel cells.* Journal of Power Sources, 2010. **195**(11): p. 3490-3493.

129. Vaalma, C., et al., *Non-aqueous K-ion battery based on layered K0. 3MnO2 and hard carbon/carbon black.* Journal of The Electrochemical Society, 2016. **163**(7): p. A1295-A1299.

130. Dec, J.E., *A conceptual model of DI diesel combustion based on laser-sheet imaging*. 1997, SAE Technical Paper.

131. Higgins, B. and D.L. Siebers, *Measurement of the flame lift-off location on DI diesel sprays using OH chemiluminescence*. 2001, SAE Technical Paper.

132. Pinson, J.A., et al., *Quantitative, planar soot measurements in a DI diesel engine using laser-induced incandescence and light scattering*. 1993, SAE Technical Paper.

133. Wiltafsky, G., et al., *The quantification of laser-induced incandescence (LII) for planar time resolved measurements of the soot volume fraction in a combusting diesel jet*. 1996, SAE Technical Paper.

134. Matsui, Y., T. Kamimoto, and S. Matsuoka, *A study on the time and space resolved measurement of flame temperature and soot concentration in a DI diesel engine by the two-color method*. 1979, SAE Technical Paper.

135. Ullman, T.L., *Investigation of the effects of fuel composition on heavy-duty diesel engine emissions*. 1989, SAE Technical Paper.

136. Ullman, T.L., K.B. Spreen, and R.L. Mason, *Effects of cetane number, cetane improver, aromatics, and oxygenates on 1994 heavy-duty diesel engine emissions*. 1994, SAE Technical Paper.

137. Lee, R., J. Pedley, and C. Hobbs, *Fuel quality impact on heavy duty diesel emissions:-a literature review*. 1998, SAE Technical Paper.

138. Nakakita, K., et al., *Effect of Hydrocarbon Molecular Structure on Diesel Exhaust Emissions: Part 1: Comparison of Combustion and Exhaust Emission Characteristics among Representative Diesel Fuels.* SAE transactions, 1998: p. 1173-1180.

139. Takatori, Y., et al., *Effect of hydrocarbon molecular structure on diesel exhaust emissions part 2: effect of branched and ring structures of paraffins on benzene and soot formation*. 1998, SAE Technical Paper.

140. Liotta, F.J. and D.M. Montalvo, *The effect of oxygenated fuels on emissions from a modern heavy-duty diesel engine*. 1993, SAE Technical Paper.

141. Beatrice, C., C. Bertoli, and N. Giacomo, *New findings on combustion behavior of oxygenated synthetic diesel fuels.* Combustion science and technology, 1998. **137**(1-6): p. 31-50.

142. Feng, X., et al., *The effects of EGR and injection timing on the engine combustion and emission performances fueled by butanol-diesel blends.* SAE International Journal of Engines, 2012. **5**(3): p. 794-811.

143. Pickett, L.M. and D.L. Siebers, *Soot in diesel fuel jets: effects of ambient temperature, ambient density, and injection pressure.* Combustion and Flame, 2004. **138**(1-2): p. 114-135.

144. Bae, C. and J. Kim, *Alternative fuels for internal combustion engines.* Proceedings of the Combustion Institute, 2017. **36**(3): p. 3389-3413.

145. Cetinkaya, M., et al., *Engine and winter road test performances of used cooking oil originated biodiesel.* Energy Conversion and Management, 2005. **46**(7-8): p. 1279-1291.

146. Lin, Y.-C., et al., *Comparison of PAH and regulated harmful matter emissions from biodiesel blends and paraffinic fuel blends on engine accumulated mileage test.* Fuel, 2006. **85**(17-18): p. 2516-2523.

147. Monyem, A. and J.H. Van Gerpen, *The effect of biodiesel oxidation on engine performance and emissions.* Biomass and bioenergy, 2001. **20**(4): p. 317-325.

148. Schmidt, K. and J. Van Gerpen, *The effect of biodiesel fuel composition on diesel combustion and emissions*. 1996, SAE Technical Paper.

149. Scholl, K.W. and S.C. Sorenson, *Combustion of soybean oil methyl ester in a direct injection diesel engine.* SAE Transactions, 1993: p. 1450-1462.

150. Turrio-Baldassarri, L., et al., *Emission comparison of urban bus engine fueled with diesel oil and 'biodiesel'blend.* Science of the Total Environment, 2004. **327**(1-3): p. 147-162.

151. Labeckas, G. and S. Slavinskas, *The effect of rapeseed oil methyl ester on direct injection diesel engine performance and exhaust emissions.* Energy conversion and Management, 2006. **47**(13-14): p. 1954-1967.

152. Last, R.J., M. Krüger, and M. Dürnholz, *Emissions and performance characteristics of a 4-stroke, direct injected diesel engine fueled with blends of biodiesel and low sulfur diesel fuel*. 1995, SAE Technical Paper.

153. Charlet, A., P. Higelin, and J. Andrzejewski, *Etude comparative des émissions d'un moteur diesel fonctionnant au gazole et différentes huiles végétales.* Entropie, 1993. **29**(174-75): p. 109-113.

154. VON WEDEL, R., *Handbook of biodiesel: emissions reductions with biodiesel. 1999*. 2011.

155. Hansen, K.F. and M.G. Jensen, *Chemical and biological characteristics of exhaust emissions from a DI diesel engine fuelled with rapeseed oil methyl ester (RME)*. 1997, SAE Technical Paper.

156. Murillo, S., et al., *Performance and exhaust emissions in the use of biodiesel in outboard diesel engines.* Fuel, 2007. **86**(12-13): p. 1765-1771.

157. Shi, X., et al., *Emission characteristics using methyl soyate–ethanol–diesel fuel blends on a diesel engine.* Fuel, 2005. **84**(12-13): p. 1543-1549.

158. Haas, M.J., et al., *Engine performance of biodiesel fuel prepared from soybean soapstock: a high quality renewable fuel produced from a waste feedstock.* Energy & Fuels, 2001. **15**(5): p. 1207-1212.

159. Durbin, T.D. and J.M. Norbeck, *Effects of biodiesel blends and Arco EC-diesel on emissions from light heavy-duty diesel vehicles.* Environmental science & technology, 2002. **36**(8): p. 1686-1691.

160. Leung, D.Y., Y. Luo, and T.-L. Chan, *Optimization of exhaust emissions of a diesel engine fuelled with biodiesel.* Energy & fuels, 2006. **20**(3): p. 1015-1023.

161. Kholghy, M., et al., *The evolution of soot morphology in a laminar coflow diffusion flame of a surrogate for Jet A-1.* Combustion and Flame, 2013. **160**(10): p. 2119-2130.

162. Kondo, K., et al., *Uncertainty in sampling and TEM analysis of soot particles in Diesel spray flame*. 2013, SAE Technical Paper.

163. http://gasengineyatoshido.blogspot.com/2017/05/gas-engine-combustion.html.

164. Smyth, K.C., et al., *Soot inception in a methane/air diffusion flame as characterized by detailed species profiles.* Combustion and flame, 1985. **62**(2): p. 157-181.

165. Smooke, M., et al., *Computational and experimental study of soot formation in a coflow, laminar diffusion flame.* Combustion and Flame, 1999. **117**(1): p. 117-139.

166. Snelling, D.R., et al., *Determination of the soot absorption function and thermal accommodation coefficient using low-fluence LII in a laminar coflow ethylene diffusion flame.* Combustion and Flame, 2004. **136**(1): p. 180-190.

167. Dobbins, R. and C. Megaridis, *Morphology of flame-generated soot as determined by thermophoretic sampling.* Langmuir, 1987. **3**(2): p. 254-259.

168. Lee, K.O., et al., *Morphological investigation of the microstructure, dimensions, and fractal geometry of diesel particulates.* Proceedings of the Combustion Institute, 2002. **29**(1): p. 647-653.

169. Lee, K.-O., et al., *Soot formation effects of oxygen concentration in the oxidizer stream of laminar coannular nonpremixed methane/air flames.* Combustion and Flame, 2000. **121**(1-2): p. 323-333.

170. Yazicioglu, A.G., et al., *Measurement of fractal properties of soot agglomerates in laminar coflow diffusion flames using thermophoretic sampling in conjunction with transmission electron microscopy and image processing.* Combustion science and technology, 2001. **171**(1): p. 71-87.

171. Ying, Y. and D. Liu, *Effects of flame configuration and soot aging on soot nanostructure and reactivity in n-butanol-doped ethylene diffusion flames.* Energy & fuels, 2017. **32**(1): p. 607-624.

172. Lapuerta, M., et al., *Morphological analysis of soot agglomerates from biodiesel surrogates in a coflow burner.* Journal of Aerosol Science, 2017. **111**: p. 65-74.

173. Santoro, R., et al., *The transport and growth of soot particles in laminar diffusion flames.* Combustion Science and Technology, 1987. **53**(2-3): p. 89-115.

174. Fassinou, W.F., *Higher heating value (HHV) of vegetable oils, fats and biodiesels evaluation based on their pure fatty acids' HHV.* Energy, 2012. **45**(1): p. 798-805.

175. Merchan-Merchan, W., S. McCollam, and J.F.C. Pugliese, *Soot formation in diffusion oxygen-enhanced biodiesel flames.* Fuel, 2015. **156**: p. 129-141.

176. Allen, C.A., et al., *Predicting the viscosity of biodiesel fuels from their fatty acid ester composition.* Fuel, 1999. **78**(11): p. 1319-1326.

177. Kincs, F.R., *Meat fat formulation.* Journal of the American Oil Chemists' Society, 1985. **62**(4): p. 815-818.

178. Zullaikah, S., et al., *A two-step acid-catalyzed process for the production of biodiesel from rice bran oil.* Bioresource technology, 2005. **96**(17): p. 1889-1896.

179. Giakoumis, E.G., *A statistical investigation of biodiesel physical and chemical properties, and their correlation with the degree of unsaturation.* Renewable Energy, 2013. **50**: p. 858-878.

180. Knothe, G., *"Designer" biodiesel: optimizing fatty ester composition to improve fuel properties.* Energy & Fuels, 2008. **22**(2): p. 1358-1364.

181. Knothe, G., A.C. Matheaus, and T.W. Ryan III, *Cetane numbers of branched and straight-chain fatty esters determined in an ignition quality tester☆.* Fuel, 2003. **82**(8): p. 971-975.

182. Megaridis, C.M. and R. Dobbins. *Soot aerosol dynamics in a laminar ethylene diffusion flame*. in *Symposium (International) on Combustion*. 1989. Elsevier.

183. Abid, A.D., et al., *On evolution of particle size distribution functions of incipient soot in premixed ethylene–oxygen–argon flames.* Combustion and Flame, 2008. **154**(4): p. 775-788.

184. Cain, J., et al., *Molecular characterization of organic content of soot along the centerline of a coflow diffusion flame.* Physical Chemistry Chemical Physics, 2014. **16**(47): p. 25862-25875.

185. Zhao, B., K. Uchikawa, and H. Wang, *A comparative study of nanoparticles in premixed flames by scanning mobility particle sizer, small angle neutron scattering, and transmission electron microscopy.* Proceedings of the Combustion Institute, 2007. **31**(1): p. 851-860.

186. Cain, J.P., et al., *Evidence of aliphatics in nascent soot particles in premixed ethylene flames.* Proceedings of the Combustion Institute, 2011. **33**(1): p. 533-540.

187. Blevins, L.G., et al., *The existence of young soot in the exhaust of inverse diffusion flames.* Proceedings of the Combustion Institute, 2002. **29**(2): p. 2325-2333.

188. Barrientos, E.J., et al., *Impact of ester structures on the soot characteristics and soot oxidative reactivity of biodiesel*. 2015, SAE Technical Paper.

189. Li, X., et al., *Impact of exhaust gas recirculation (EGR) on soot reactivity from a diesel engine operating at high load.* Applied Thermal Engineering, 2014. **68**(1-2): p. 100-106.

190. Zhang, J., et al., *Soot temperature and KL factor for biodiesel and diesel spray combustion in a constant volume combustion chamber.* Applied energy, 2013. **107**: p. 52-65.

191. Omidvarborna, H., A. Kumar, and D.-S. Kim, *Variation of diesel soot characteristics by different types and blends of biodiesel in a laboratory combustion chamber.* Science of The Total Environment, 2016. **544**: p. 450-459.

192. Jung, H., D.B. Kittelson, and M.R. Zachariah, *Characteristics of SME biodiesel-fueled diesel particle emissions and the kinetics of oxidation.* Environmental science & technology, 2006. **40**(16): p. 4949-4955.

193. Xue, J., T.E. Grift, and A.C. Hansen, *Effect of biodiesel on engine performances and emissions.* Renewable and Sustainable energy reviews, 2011. **15**(2): p. 1098-1116.

194. Wang, H., *Formation of nascent soot and other condensed-phase materials in flames.* Proceedings of the Combustion Institute, 2011. **33**(1): p. 41-67.

195. HARRIS, S.J., *Surface growth and soot particle reactivity.* Combustion Science and Technology, 1990. **72**(1-3): p. 67-77.

196. Barry, E., et al., *Heavy-duty diesel engine/fuels combustion performance and emissions-A cooperative research program*. 1985, SAE Technical Paper.

197. Calcote, H.F., *Mechanisms of soot nucleation in flames—a critical review.* Combustion and Flame, 1981. **42**: p. 215-242.

198. Haynes, B., *Wag ner, HG, Soot For ma tion.* Prog ress in En ergy and Com bus tion Sci ence, 1981. **7**(4).

199. Smith, O.I., *Fundamentals of soot formation in flames with application to diesel engine particulate emissions.* Progress in Energy and Combustion Science, 1981. **7**(4): p. 275-291.

200. Dobbins, R., R.A. Fletcher, and H.-C. Chang, *The evolution of soot precursor particles in a diffusion flame.* Combustion and flame, 1998. **115**(3): p. 285-298.

201. Maricq, M.M., *An examination of soot composition in premixed hydrocarbon flames via laser ablation particle mass spectrometry.* Journal of Aerosol Science, 2009. **40**(10): p. 844-857.

202. Bouvier, Y., et al., *Molecular species adsorbed on soot particles issued from low sooting methane and acetylene laminar flames: A laser-based experiment.* Proceedings of the Combustion Institute, 2007. **31**(1): p. 841-849.

203. Cain, J.P., et al., *Micro-FTIR study of soot chemical composition—evidence of aliphatic hydrocarbons on nascent soot surfaces.* Physical Chemistry Chemical Physics, 2010. **12**(20): p. 5206-5218.

204. Öktem, B., et al., *Chemical species associated with the early stage of soot growth in a laminar premixed ethylene–oxygen–argon flame.* Combustion and Flame, 2005. **142**(4): p. 364-373.

205. Knothe, G., C.A. Sharp, and T.W. Ryan, *Exhaust emissions of biodiesel, petrodiesel, neat methyl esters, and alkanes in a new technology engine.* Energy & Fuels, 2006. **20**(1): p. 403-408.

206. Chang, D.Y. and J.H. Van Gerpen, *Determination of particulate and unburned hydrocarbon emissions from diesel engines fueled with biodiesel*. 1998, SAE Technical Paper.

207. Reilly, P., et al., *Direct observation of the evolution of the soot carbonization process in an acetylene diffusion flame via real-time aerosol mass spectrometry.* Combustion and flame, 2000. **122**(1): p. 90-104.

208. CONSTANTINE, M.M. and A.D. Richard, *Comparison of soot growth and oxidation in smoking and non–smoking ethylene diffusion flames.* Combustion Science and Technology, 1989. **66**(1-3): p. 1-16.

209. Santamaria, A., et al., *Chemical and morphological characterization of soot and soot precursors generated in an inverse diffusion flame with aromatic and aliphatic fuels.* Combustion and flame, 2010. **157**(1): p. 33-42.

210. Oh, K.C. and H.D. Shin, *The effect of oxygen and carbon dioxide concentration on soot formation in non-premixed flames.* Fuel, 2006. **85**(5): p. 615-624.

211. Pandey, P. and B. Pundir, *Role of fluid-dynamics in soot formation and microstructure in acetylene-air laminar diffusion flames.* International Journal of Spray and Combustion Dynamics, 2015. **7**(1): p. 25-38.

212. De Iuliis, S., et al., *Effect of hydrogen addition on soot formation in an ethylene/air premixed flame.* Applied Physics B, 2012. **106**(3): p. 707-715.

213. Lahaye, J., *Particulate carbon from the gas phase.* Carbon, 1992. **30**(3): p. 309-314.

214. Kholghy, M.R., *The evolution of soot morphology in laminar co-flow diffusion flames of the surrogates for jet A-1 and a synthetic kerosene*. 2012, University of Toronto.

215. Lee, J.B., et al., *Modeling the maximum spreading of liquid droplets impacting wetting and nonwetting surfaces.* Langmuir, 2016. **32**(5): p. 1299-1308.

216. Zhang, T. and C.Y. Suen, *A fast parallel algorithm for thinning digital patterns.* Communications of the ACM, 1984. **27**(3): p. 236-239.

217. Strelnikova, N., M. Göllner, and T. Pfohl, *Direct Observation of Alternating Stretch-Coil and Coil-Stretch Transitions of Semiflexible Polymers in Microstructured Flow*. Macromolecular Chemistry and Physics, 2017. **218**(2): p. 1600474.

218. Marin, A.J.S., *Effect on Fuel Injection Timing on the Combustion of Various Biofuels in a Diesel Engine*. 2008, University of Oklahoma.

219. Gomez, A., M. Littman, and I. Glassman, *Comparative study of soot formation on the centerline of axisymmetric laminar diffusion flames: fuel and temperature effects.* Combustion and Flame, 1987. **70**(2): p. 225-241.

220. Love, N., et al. *Comparison of Soot Volume Fraction, Temperature, and Radiation in Petroleum Diesel and Biodiesel Flames*. in *46th AIAA Aerospace Sciences Meeting and Exhibit*. 2008.

221. Cheng, T., Y. Wu, and H. Chen, *Effects of morphology on the radiative properties of internally mixed light absorbing carbon aerosols with different aging status.* Optics express, 2014. **22**(13): p. 15904-15917.

222. Chakrabarty, R.K., et al., *Low fractal dimension cluster-dilute soot aggregates from a premixed flame.* Physical review letters, 2009. **102**(23): p. 235504.

223. Smallwood, G.J., et al., *Concurrent quantitative laser-induced incandescence and SMPS measurements of EGR effects on particulate emissions from a TDI diesel engine*. 2002, SAE Technical Paper.

224. Wentzel, M., et al., *Transmission electron microscopical and aerosol dynamical characterization of soot aerosols.* Journal of aerosol science, 2003. **34**(10): p. 1347-1370.

225. Wozniak, M., et al., *Comparison of methods to derive morphological parameters of multi-fractal samples of particle aggregates from TEM images.* Journal of Aerosol Science, 2012. **47**: p. 12-26.

226. Lapuerta, M., R. Ballesteros, and F.J. Martos, *A method to determine the fractal dimension of diesel soot agglomerates.* Journal of colloid and interface science, 2006. **303**(1): p. 149-158.

227. Savic, N., et al., *Influence of biodiesel fuel composition on the morphology and microstructure of particles emitted from diesel engines.* Carbon, 2016. **104**: p. 179-189.

228. Wu, Y., et al., *The single scattering properties of soot aggregates with concentric core–shell spherical monomers.* Journal of Quantitative Spectroscopy and Radiative Transfer, 2014. **135**: p. 9-19.

229. Neer, A. and U.O. Koylu, *Effect of operating conditions on the size, morphology, and concentration of submicrometer particulates emitted from a diesel engine.* Combustion and Flame, 2006. **146**(1): p. 142-154.

230. Zhu, J., et al., *Effects of engine operating conditions on morphology, microstructure, and fractal geometry of light-duty diesel engine particulates.* Proceedings of the Combustion Institute, 2005. **30**(2): p. 2781-2789.

231. Yehliu, K., et al., *Impact of engine operating modes and combustion phasing on the reactivity of diesel soot.* Combustion and Flame, 2013. **160**(3): p. 682-691.

232. Medalia, A.I., *Morphology of aggregates: I. Calculation of shape and bulkiness factors; application to computer-simulated random flocs.* Journal of Colloid and Interface Science, 1967. **24**(3): p. 393-404.

233. Mandelbrot, B., *Les Objets Fractals (The Fractal Objects).* Flammarion, Paris, France, 1975: p. 246.

234. Katrinak, K.A., et al., *Fractal geometry of carbonaceous aggregates from an urban aerosol.* Environmental science & technology, 1993. **27**(3): p. 539-547.

235. Mandelbrot, B.B., *The fractal geometry of nature. 1982.* San Francisco, CA, 1982.

236. Jiang, Q. and B.E. Logan, *Fractal dimensions of aggregates determined from steady-state size distributions.* Environmental Science & Technology, 1991. **25**(12): p. 2031-2038.

237. Forrest, S. and T. Witten Jr, *Long-range correlations in smoke-particle aggregates.* Journal of Physics A: Mathematical and General, 1979. **12**(5): p. L109.

238. Samson, R., G.W. Mulholland, and J. Gentry, *Structural analysis of soot agglomerates.* Langmuir, 1987. **3**(2): p. 272-281.

239. Köylü, Ü.Ö., et al., *Fractal and projected structure properties of soot aggregates.* Combustion and Flame, 1995. **100**(4): p. 621-633.

240. Zhang, R. and S. Kook, *Structural evolution of soot particles during diesel combustion in a single-cylinder light-duty engine.* Combustion and Flame, 2015. **162**(6): p. 2720-2728.

241. Shi, J.P., D. Mark, and R.M. Harrison, *Characterization of particles from a current technology heavy-duty diesel engine.* Environmental Science & Technology, 2000. **34**(5): p. 748-755.

242. Aizawa, T., et al., *Transmission electron microscopy of soot particles directly sampled in diesel spray flame-A comparison between US# 2 and biodiesel soot.* SAE International Journal of Fuels and Lubricants, 2012. **5**(2012-01-0695): p. 665-673.

243. Kondo, K., et al., *High-resolution transmission electron microscopy of soot directly sampled at different axial locations in diesel spray flame*. 2011, SAE Technical Paper.

244. Yamaguchi, T., et al., *Direct sampling, TEM analysis and optical measurement of soot particles at different axial locations in a transient spray flame.* SAE International Journal of Fuels and Lubricants, 2011. **5**(2011-01-2051): p. 316-328.

245. Manin, J., L.M. Pickett, and S.A. Skeen, *Two-color diffused back-illumination imaging as a diagnostic for time-resolved soot measurements in reacting sprays.* SAE International Journal of Engines, 2013. **6**(2013-01-2548): p. 1908-1921.

246. Sorensen, C., *Light scattering by fractal aggregates: a review.* Aerosol Science & Technology, 2001. **35**(2): p. 648-687.

247. Sorensen, C.M. and G.C. Roberts, *The prefactor of fractal aggregates.* Journal of colloid and interface science, 1997. **186**(2): p. 447-452.

248. Theiler, J., *Estimating fractal dimension.* JOSA A, 1990. **7**(6): p. 1055-1073.

249. Schroeder, M., *Fractals, chaos, power laws: Minutes from an infinite paradise*. 2009: Courier Corporation.

250. Foroutan-pour, K., P. Dutilleul, and D.L. Smith, *Advances in the implementation of the box-counting method of fractal dimension estimation.* Applied mathematics and computation, 1999. **105**(2): p. 195-210.

251. Zhang, R. and S. Kook, *Influence of fuel injection timing and pressure on in-flame soot particles in an automotive-size diesel engine.* Environmental science & technology, 2014. **48**(14): p. 8243-8250.

252. MEGARIDIS, C.M. and R.A. DOBBINS, *Morphological description of flame-generated materials.* Combustion Science and Technology, 1990. **71**(1-3): p. 95-109.

253. Rogak, S.N. and R.C. Flagan, *Characterization of the structure of agglomerate particles.* Particle & particle systems characterization, 1992. **9**(1-4): p. 19-27.

254. Nelson, J., R. Crookes, and S. Simons, *On obtaining the fractal dimension of a 3D cluster from its projection on a plane-application to smoke agglomerates.* Journal of Physics D: Applied Physics, 1990. **23**(4): p. 465.

255. Jullien, R. and R. Botet, *Aggregation and fractal aggregates.* Ann. Telecomm., 1987. **41**: p. 343 (short version).

256. Tence, M., J. Chevalier, and R. Jullien, *On the measurement of the fractal dimension of aggregated particles by electron microscopy: experimental method,*

corrections and comparison with numerical models. Journal de Physique, 1986. **47**(11): p. 1989-1998.

257. Köylü, U.O. and G. Faeth, *Optical properties of overfire soot in buoyant turbulent diffusion flames at long residence times.* Journal of Heat Transfer, 1994. **116**(1): p. 152-159.

258. Merchan-Merchan, W., A. Abdihamzehkolaei, and D.A. Merchan-Breuer, *Formation and evolution of carbon particles in coflow diffusion air flames of vaporized biodiesel, diesel and biodiesel-diesel blends.* Fuel, 2018. **226**: p. 263-277.

259. Merchan-Merchan, W., S.G. Sanmiguel, and S. McCollam, *Analysis of soot particles derived from biodiesels and diesel fuel air-flames.* Fuel, 2012. **102**: p. 525-535.

260. Aizawa, T., et al., *Transmission electron microscopy of soot particles directly sampled in diesel spray flame-A comparison between US# 2 and biodiesel soot.* SAE International Journal of Fuels and Lubricants, 2012. **5**(2): p. 665-673.

261. Chung, A., A. Lall, and S. Paulson, *Particulate emissions by a small non-road diesel engine: Biodiesel and diesel characterization and mass measurements using the extended idealized aggregates theory.* Atmospheric Environment, 2008. **42**(9): p. 2129-2140.

262. Gogos, A., et al., *Capabilities of asymmetric flow field-flow fractionation coupled to multi-angle light scattering to detect carbon nanotubes in soot and soil.* Environmental Science: Nano, 2014. **1**(6): p. 584-594.

263. Fayad, M.A., et al., *Role of alternative fuels on particulate matter (PM) characteristics and influence of the diesel oxidation catalyst.* Environmental science & technology, 2015. **49**(19): p. 11967-11973.

264. Lahaye, J. and F. Ehrburger-Dolle, *Mechanisms of carbon black formation. Correlation with the morphology of aggregates.* Carbon, 1994. **32**(7): p. 1319-1324.

265. Meakin, P., *Computer simulation of growth and aggregation processes*, in *On Growth and Form*. 1986, Springer. p. 111-135.

266. Friedlander, S.K. and D. Smoke, *Haze: Fundamentals of aerosol dynamics.* Oxford University Press, New York, 2000.

267. Yusuf, N., S.K. Kamarudin, and Z. Yaakub, *Overview on the current trends in biodiesel production.* Energy conversion and management, 2011. **52**(7): p. 2741-2751.

268. Pham, P., et al., *Engine performance characteristics for biodiesels of different degrees of saturation and carbon chain lengths.* SAE International Journal of Fuels and Lubricants, 2013. **6**(1): p. 188-198.

269. Rahman, M., et al., *Particle emissions from biodiesels with different physical properties and chemical composition.* Fuel, 2014. **134**: p. 201-208.

270. Zhu, L., C. Cheung, and Z. Huang, *Impact of chemical structure of individual fatty acid esters on combustion and emission characteristics of diesel engine.* Energy, 2016. **107**: p. 305-320.

271. Zhu, L., C. Cheung, and Z. Huang, *A comparison of particulate emission for rapeseed oil methyl ester, palm oil methyl ester and soybean oil methyl ester in perspective of their fatty ester composition.* Applied thermal engineering, 2016. **94**: p. 249-255.

272. Tzamkiozis, T., et al., *Aerodynamic and mobility size distribution measurements to reveal biodiesel effects on diesel exhaust aerosol.* Aerosol Science and Technology, 2011. **45**(5): p. 587-595.

273. Kittelson, D.B., *Engines and nanoparticles: a review.* Journal of aerosol science, 1998. **29**(5): p. 575-588.

274. Sukjit, E., et al., *The effect of the addition of individual methyl esters on the combustion and emissions of ethanol and butanol-diesel blends.* Energy, 2012. **42**(1): p. 364-374.

275. Lapuerta, M., et al., *Effect of the alcohol type used in the production of waste cooking oil biodiesel on diesel performance and emissions.* Fuel, 2008. **87**(15-16): p. 3161-3169.

276. Gill, S., et al., *Diesel emissions improvements through the use of biodiesel or oxygenated blending components.* Fuel, 2012. **95**: p. 578-586.

277. Man, X., et al., *Effect of waste cooking oil biodiesel on the properties of particulate from a DI diesel engine.* Aerosol Science and Technology, 2015. **49**(4): p. 199-209.

278. Seong, H., et al., *Characterization of particulate morphology, nanostructures, and sizes in low-temperature combustion with biofuels*. 2012, SAE Technical Paper.

279. Lapuerta, M., et al., *Effect of fuel on the soot nanostructure and consequences on loading and regeneration of diesel particulate filters.* Combustion and Flame, 2012. **159**(2): p. 844-853.

280. Walker, A., *Controlling particulate emissions from diesel vehicles.* Topics in catalysis, 2004. **28**(1-4): p. 165-170.

281. Pawlyta, M. and H. Hercman. *Transmission electron microscopy (TEM) as a tool for identification of combustion products: application to black layers in speleothems*. in *Annales Societatis Geologorum Poloniae*. 2016.

282. Bambha, R.P., et al., *Effects of volatile coatings and coating removal mechanisms on the morphology of graphitic soot.* Carbon, 2013. **61**: p. 80-96.

283. Liu, Y., et al., *Structural and hygroscopic changes of soot during heterogeneous reaction with O 3.* Physical Chemistry Chemical Physics, 2010. **12**(36): p. 10896-10903.

284. Kim, K., K. Masiello, and D. Hahn, *Reduction of soot emissions by iron pentacarbonyl in isooctane diffusion flames.* Combustion and Flame, 2008. **154**(1-2): p. 164-180.

285. Lapuerta, M., R. Ballesteros, and J. Rodríguez-Fernández, *Thermogravimetric analysis of diesel particulate matter.* Measurement Science and Technology, 2007. **18**(3): p. 650.

286. Shaddix, C.R. and T.C. Williams, *Soot: giver and taker of light; The complex structure of soot greatly influences the optical effects seen in fires.* American scientist, 2007. **95**(3): p. 232-240.

287. Vander Wal, R.L. and A.J. Tomasek, *Soot oxidation: dependence upon initial nanostructure.* Combustion and flame, 2003. **134**(1-2): p. 1-9.

288. Mathis, U., et al., *Influence of diesel engine combustion parameters on primary soot particle diameter.* Environmental science & technology, 2005. **39**(6): p. 1887-1892.

289. Vander Wal, R.L. and C.J. Mueller, *Initial investigation of effects of fuel oxygenation on nanostructure of soot from a direct-injection diesel engine.* Energy & Fuels, 2006. **20**(6): p. 2364-2369.

290. Li, Z., et al., *Evolution of the nanostructure, fractal dimension and size of in-cylinder soot during diesel combustion process.* Combustion and Flame, 2011. **158**(8): p. 1624-1630.

291. Alfè, M., et al., *Structure–property relationship in nanostructures of young and mature soot in premixed flames.* Proceedings of the Combustion Institute, 2009. **32**(1): p. 697-704.

292. Kholghy, M.R., A. Veshkini, and M.J. Thomson, *The core–shell internal nanostructure of soot–A criterion to model soot maturity.* Carbon, 2016. **100**: p. 508-536.

293. Müller, J.-O., et al., *Diesel engine exhaust emission: oxidative behavior and microstructure of black smoke soot particulate.* Environmental science & technology, 2006. **40**(4): p. 1231-1236.

294. Wei, Y., et al., *Multifunctional catalysts of three-dimensionally ordered macroporous oxide-supported Au@ Pt core–shell nanoparticles with high catalytic activity and stability for soot oxidation.* Journal of catalysis, 2014. **317**: p. 62-74.

295. Adachi, K., S.H. Chung, and P.R. Buseck, *Shapes of soot aerosol particles and implications for their effects on climate.* Journal of Geophysical Research: Atmospheres, 2010. **115**(D15).

296. Vander Wal, R.L., *A TEM methodology for the study of soot particle structure.* Combustion science and technology, 1997. **126**(1-6): p. 333-351.

297. Song, J., et al., *Examination of the oxidation behavior of biodiesel soot.* Combustion and flame, 2006. **146**(4): p. 589-604.

298. Yehliu, K., et al., *Impact of fuel formulation on the nanostructure and reactivity of diesel soot.* Combustion and Flame, 2012. **159**(12): p. 3597-3606.

299. Wal, R.L.V., *Soot nanostructure: definition, quantification and implications.* SAE transactions, 2005: p. 429-436.

300. Palotás, Á.B., et al., *Soot morphology: An application of image analysis in high-resolution transmission electron microscopy.* Microscopy research and technique, 1996. **33**(3): p. 266-278.

301. Vander Wal, R.L., et al., *Analysis of HRTEM images for carbon nanostructure quantification.* Journal of Nanoparticle Research, 2004. **6**(6): p. 555-568.

302. Sharma, A., T. Kyotani, and A. Tomita, *A new quantitative approach for microstructural analysis of coal char using HRTEM images.* Fuel, 1999. **78**(10): p. 1203-1212.

303. Shim, H.-S., R.H. Hurt, and N.Y. Yang, *A methodology for analysis of 002 lattice fringe images and its application to combustion-derived carbons.* Carbon, 2000. **38**(1): p. 29-45.

304. Galvez, A., et al., *Carbon nanoparticles from laser pyrolysis.* Carbon, 2002. **40**(15): p. 2775-2789.

305. Yehliu, K., R.L. Vander Wal, and A.L. Boehman, *Development of an HRTEM image analysis method to quantify carbon nanostructure.* Combustion and Flame, 2011. **158**(9): p. 1837-1851.

306. Belenkov, E., *Formation of graphite structure in carbon crystallites.* Inorganic Materials, 2001. **37**(9): p. 928-934.

307. Grieco, W.J., et al., *Fullerenic carbon in combustion-generated soot.* Carbon, 2000. **38**(4): p. 597-614.

308. Pope, C.J., J.A. Marr, and J.B. Howard, *Chemistry of fullerenes C60 and C70 formation in flames.* The Journal of Physical Chemistry, 1993. **97**(42): p. 11001-11013.

309. Yehliu, K., R.L. Vander Wal, and A.L. Boehman, *A comparison of soot nanostructure obtained using two high resolution transmission electron microscopy image analysis algorithms.* Carbon, 2011. **49**(13): p. 4256-4268.

310. Gonzalez, R. and R. Woods, *Digital image processing: Pearson prentice hall.* Upper Saddle River, NJ, 2008. **1**.

311. Sakai, M., et al., *Nanostructure analysis of primary soot particles directly sampled in diesel spray flame via HRTEM*. 2012, SAE Technical Paper.

312. Gaddam, C.K., C.-H. Huang, and R.L. Vander Wal, *Quantification of nano-scale carbon structure by HRTEM and lattice fringe analysis.* Pattern Recognition Letters, 2016. **76**: p. 90-97.

313. Botero, M.L., et al., *HRTEM evaluation of soot particles produced by the non-premixed combustion of liquid fuels.* Carbon, 2016. **96**: p. 459-473.

314. Zhang, Y., R. Zhang, and S. Kook, *Nanostructure analysis of in-flame soot particles under the influence of jet-jet interactions in a light-duty diesel engine.* SAE International Journal of Engines, 2015. **8**(5): p. 2213-2226.

315. Li, Z., et al., *The evolution of soot morphology and nanostructure in laminar diffusion flame of surrogate fuels for diesel.* Fuel, 2018. **211**: p. 517-528.

316. Rouzaud, J.-N. and C. Clinard, *Quantitative high-resolution transmission electron microscopy: a promising tool for carbon materials characterization.* Fuel Processing Technology, 2002. **77**: p. 229-235.

317. Jaramillo, I.C., et al., *Soot oxidation kinetics under pressurized conditions.* Combustion and Flame, 2014. **161**(11): p. 2951-2965.